

AN ABSTRACT OF THE THESIS OF

Gunnar Luderer for the degree of Master of Science in Atmospheric Sciences
presented on October 2, 2003.

Title:

Modeling and Application of Multispectral Oceanic Sun Glint Observations

Redacted for privacy

Abstract approved:

James A. Coakley, Jr.

The atmospheric radiative transfer model MOCARAT was developed and is presented in this thesis. MOCARAT employs a Monte Carlo Technique for the accurate modeling of band radiances and reflectances in an atmospheric system with a ruffled ocean surface as a lower boundary. The atmospheric radiative transfer is modeled with consideration of molecular Rayleigh scattering, Mie Scattering and absorption on particulate matter, as well as band absorption by molecules in the wavelength channels of interest. The bidirectional reflection of downwelling light at the ocean surface is computed using the empirical relationship between surface wind field and the slope distribution of wave facets derived by Cox and Munk (1954a).

A method is proposed to use the oceanic sun glint for remote sensing applications. The sensitivity of channel correlations to aerosol burden and type as well as other atmospheric and observational parameters is assessed. Comparisons of observed correlations with model results are used to check the consistency of the calibration of the airborne Multichannel Cloud Radiometer (MCR) that

was employed during the Indian Ocean Experiment (INDOEX). The MCR calibration exhibited large variability from flight to flight. The method was applied to MODIS observations. Unlike the MCR, MODIS was stable where expected, although numerical values for some of the wavelengths appear to depart from theory.

©Copyright by Gunnar Luderer

October 2, 2003

All Rights Reserved

Modeling and Application of Multispectral Oceanic Sun Glint Observations

by

Gunnar Luderer

A THESIS

submitted to

Oregon State University

in partial fulfillment of
the requirements for the
degree of

Master of Science

Completed October 2, 2003
Commencement June 2004

Master of Science thesis of Gunnar Luderer presented on October 2, 2003

APPROVED:

Redacted for privacy

Major Professor, representing Atmospheric Sciences

Redacted for privacy

Dean of the College of Oceanic and Atmospheric Sciences

Redacted for privacy

Dean of the Graduate School

I understand that my thesis will become part of the permanent collection of Oregon State University libraries. My **Redacted for privacy**

Redacted for privacy

, Author

ACKNOWLEDGMENTS

I would like to express my sincere gratitude to Prof. James A. Coakley, Jr. for the opportunity to work in his group, the excellent mentoring, and the numerous, very productive discussions we had. Jim's enthusiasm for science in general and climate research in particular has been a great inspiration for me. I would also like to thank Profs. Richard J. Vong, Murray D. Levine, and Bruce P. McCune for serving on my committee and examining my thesis.

Thanks also to my co-workers Mark Matheson and Bill Tahnk. I have enjoyed the good atmosphere in our group and I am grateful for their assistance with technical issues and all sorts of other problems.

I had a great time spending a school year and two summers in Oregon. I would like to thank my friends and hiking buddies, especially Nora and Michael, as well as my house mates from the Veggie House and my fellow graduate students for helping to make my stay in Oregon such a great time and exploring the Pacific Northwest with me.

I am very grateful for the support and inspiration from my parents and my siblings. Finally, I would like to thank Maren for her continuing love, encouragement and support. Maren herself knows best how much she means to me!

This research project was funded by the NOAA Climate and Global Change Program, Grant NA16GP2911. The scholarship by the Friedrich-Ebert-Foundation and the Fulbright travel grant that supported my first academic year of study at Oregon State University as well as the funding by NOAA are greatly appreciated.

TABLE OF CONTENTS

	<u>Page</u>
Chapter 1: Introduction	1
1.1 Motivation	1
1.2 Background	3
1.3 Outline	4
Chapter 2: Theory of Atmospheric Radiative Transfer	6
2.1 Basic Quantities	6
2.2 Scattering	8
2.2.1 Rayleigh Scattering	9
2.2.2 Mie Scattering	11
2.3 Absorption	15
2.4 The Equation of Radiative Transfer	17
2.5 Radiation from the Ocean	19
2.5.1 Bidirectional Reflectance at the Ocean's Surface	19
2.5.2 Upwelling Radiation from the Ocean Interior	27
Chapter 3: The Indian Ocean Experiment (INDOEX)	30
3.1 Aerosol Climate Interactions	31
3.2 Aerosol Sources	33
3.3 Aerosol Types for INDOEX	34
3.4 The Multichannel Cloud Radiometer (MCR)	41
Chapter 4: MOCARAT: A Monte Carlo Radiative Transfer Model	45

TABLE OF CONTENTS (Continued)

		<u>Page</u>
4.1	Algorithmic Realization	47
	4.1.1 Sampling of Photon Paths	48
	4.1.2 Generation of Random Variables	49
4.2	Simulation of Scattering	51
4.3	Simulation of Absorption	56
	4.3.1 The Lookup-Table Scheme	56
	4.3.2 The Method of Correlated k -Distributions	58
4.4	Reflecting Ocean Surface	61
	4.4.1 Quasi-Lambertian Subsurface Reflection	61
	4.4.2 Simulation of Photon Reflection from the Ocean	62
4.5	Wavelength Dependence	65
4.6	Results	66
4.7	Error Estimation and Limitations of the Model	68
Chapter 5: Verification		71
5.1	Verification of Atmospheric Radiative Transfer: Comparison with RADK/DISORT	72
	5.1.1 Test Case 1: MODIS Channel 1 Radiances, Low Surface Albedo	72
	5.1.2 Test Case 2: Molecular Absorption and High Surface Albedo	74
5.2	Verification of Ocean Surface Reflection: Comparison with li- bRadtran and SBDART	77
	5.2.1 Test Case 3: Reflecting Ocean Surface with Isotropic Slope Distribution	77
	5.2.2 Test Case 4: Reflecting Ocean Surface with Anisotropic Slope Distribution	79

TABLE OF CONTENTS (Continued)

	<u>Page</u>
Chapter 6: Remote Sensing Applications of Sun Glint	82
6.1 Method	82
6.2 Sensitivity Studies	85
6.2.1 Average Continental Aerosol	87
6.2.2 Tropical Marine Aerosol	88
6.2.3 Wind Speed and Direction	91
6.2.4 Solar Geometry	93
6.2.5 Water Vapor Abundance	98
6.3 Consistency of calibration of the MCR	98
6.4 Consistency Tests for MODIS	102
Chapter 7: Conclusions	107
Bibliography	110

LIST OF FIGURES

<u>Figure</u>		<u>Page</u>
2.1	Geometry of the reflection at the ruffled ocean surface.	23
3.1	Spectral dependence of the extinction coefficient per unit aerosol number concentration for the average continental (a) and tropical marine (b) aerosol model. The contributions of the various components are plotted in color.	38
3.2	Atmospheric absorption for a vertical path in the wavelength ranges for MCR channels 1, 4, 5 and 6.	42
4.1	Simplified flowchart of a photon's random trial through the model atmosphere.	50
4.2	A new coordinate frame S^* aligned with the photon incident under \vec{v} with angles ϑ, φ is introduced in order to derive the new direction of propagation \vec{v}' with angles ϑ', φ'	54
4.3	Example of results computed with MOCARAT. The radiance field is visualized as a polar plot (a). Principal plane reflectances are given in (b).	67
5.1	Reflectances computed for test case 1. A polar plot of the results obtained by MOCARAT (a) and RADK/DISORT (b). Comparison of the principal plane reflectances computed by MOCARAT and RADK/DISORT (c). Polar plot of the relative deviation between the model results (d).	73
5.2	Reflectances computed for test case 2. A polar plot of the results obtained by MOCARAT (a) and RADK/DISORT (b). Comparison of the principal plane reflectances computed by MOCARAT and RADK/DISORT (c). Polar plot of the relative deviation between the model results (d).	76
5.3	Reflectances computed for test case 3. Polar plots of the results obtained by MOCARAT (a), libRadtran (b), and SBDART (c). Comparison of the principal plane reflectances (d). Polar plots of the relative deviation between the reference models and MOCARAT (e), (f). Note change in scale.	78

LIST OF FIGURES (Continued)

<u>Figure</u>		<u>Page</u>
5.4	Reflectances computed for test case 4. Polar plots of the results computed by MOCARAT (a) and libRadtran (b). The principal plane reflectances are given in (c). (d) is a plot of the relative deviation between MOCARAT and libRadtran	80
6.1	Analysis of the correlation of sun glint reflectances observed during INDOEX Flight 8 by the MCR. The highlighted box in (a) shows the pixels used for the analysis. The correlation diagram for channels 1 and 4 (b). Modeled reflectances (c) and correlation (d) of the grid points corresponding to the observational pixels used. Tropical marine aerosol was considered and results in (d) are given for reference optical depths of 0.05, 0.10, 0.20.	83
6.2	Ratios of the Fresnel reflectances for MCR wavelength channels 1 (0.64 μm), 4 (1.06 μm), 5 (1.64 μm), and 6 (2.16 μm) as a function of reflection angle.	86
6.3	Correlation diagrams for the sun glint reflectances of the MCR's wavelength channels. Figures (a), (c), (e) show the sensitivity to average continental aerosol burden. Figures (b), (d), (f) show the sensitivity to tropical marine aerosol burden.	89
6.4	Sensitivity to aerosol burden for the NOAA Phase 2 aerosol model.	90
6.5	Sensitivity to wind speed. Figures (a), (c), (e) show the sensitivity for average continental aerosol. Figures (b), (d), (f) show the sensitivity for tropical marine aerosol.	92
6.6	Analysis of the sensitivity of the correlation method to wind direction. Calculations were performed for an isotropic distribution (iso), and anisotropic distributions with relative azimuth angles $\varphi_w = 0^\circ, 90^\circ$. An average continental aerosol was assumed.	94
6.7	Correlation diagrams for the sun glint reflectances of the MCR's wavelength channels. Figures (a), (c) show the sensitivity to solar zenith angle for average continental aerosol. Figures (b), (d) show the sensitivity to solar zenith angle for tropical marine aerosol.	96

LIST OF FIGURES (Continued)

<u>Figure</u>	<u>Page</u>
6.8 Modeled correlation between channel 1 and channel 4 radiances for different relative azimuth angles φ_{rel} between scanning line and solar incidence.	97
6.9 Sensitivity to water vapor abundance. Simulations were performed for H ₂ O profiles from a tropical (trop), and a mid-latitude summer (mls) model, as well as the U.S. 1976 Standard Atmosphere (U.S.).	99
6.10 Modeled correlations of 0.64 μm reflectance with 1.64 μm reflectance (a) and 2.13 μm reflectance (b) for MODIS. Calculations for $\tau_{ref} = 0.05, 0.10, 0.20$ are presented.	105

LIST OF TABLES

<u>Table</u>	<u>Page</u>
3.1 Microphysical parameters for the different aerosol components taken from Hess et al. (1998). The refractive index is given at a reference wavelength of 0.55 μm	37
3.2 Optical properties of the composite aerosol models (Hess et al., 1998; Coakley et al., 2002). The values are given for a reference wavelength of 0.65 μm . The relative humidity was considered to be 80 % for the hygroscopic species. Ångström coefficients were calculated for the 0.64 μm to 1.64 μm range.	39
3.3 The channel configuration of the MCR as operated during the INDOEX campaign	44
4.1 Parameter values relevant for the calculation of the quasi-Lambertian subsurface albedo α_L for different wavelengths. Coefficients of scattering and absorption in the ocean by molecules and hydrosols as well as the hydrosol asymmetry parameter. Parameter values adapted from Walker (1994).	63
6.1 Comparison of observed and modeled channel correlations. The model results are given for $\tau_{ref} = 0.10$	101
6.2 Observed channel correlations for MODIS.	104

*Meiner
herzallerliebsten
Maren*

MODELING AND APPLICATION OF MULTISPECTRAL OCEANIC SUN GLINT OBSERVATIONS

CHAPTER 1

INTRODUCTION

1.1 Motivation

Remote sensing is the science of acquiring information about the earth system from the analysis of electromagnetic radiation recorded from space-borne, airborne or ground-based platforms. In the disciplines of Atmospheric Sciences in particular, it has become an enormously important and successful tool of observational research. It is relevant for short term meteorology and long term analysis of the atmospheric system alike. Accurate weather forecasting relies heavily on the analysis of satellite images. Remote sensing observations have also resulted in significant improvements in the understanding of the most pressing issues of man's impact on the earth-atmosphere system - for example, the depletion of stratospheric ozone and radiative forcing due to aerosols. Undoubtedly, remote sensing will continue to play this crucial role.

Remote sensing is differentiated from in-situ observations, where specific measurements are performed within the medium of interest. For remote sensing, the targeted physical parameters are derived indirectly from the detected signal, which is functionally related to them (Liou, 2002, sec. 7.1). Typically, the measuring function is complicated and non-linear. Whereas for some applications it is possible to invert the measuring function in order to obtain the desired features of the target from the observed signal, for many applications such an

explicit inversion is mathematically not possible. It is therefore necessary to simulate the radiance field observed by the detector for a series of different parameter values and retrieve the target parameters through comparisons of the actual observations with the simulated signals. Consequently, accurate atmospheric radiative transfer modeling is the key for proper analysis of remotely sensed data.

With high performance computers readily available, sophisticated modeling of multi-scattering atmospheric radiative transfer has become possible. An example is given by the very commonly used, well established Discrete Ordinate Radiative Transfer (DISORT) model. In its raw form, this model simulates monochromatic radiative transfer in a plane-parallel atmosphere with an isotropically reflecting lower boundary. Efforts have been made to incorporate increasingly more complex processes in the simulations such as polarization (Evans and Stephens, 1991), non-grey molecular band transmission (Kratz, 1995), horizontally non-uniform cloud fields (Cahalan and Davies, 2000), and anisotropic surface reflection.

The phenomenon of ocean sun glint, the specular reflection of direct sun light at the ocean surface, was explored in a pioneering study by Cox and Munk (1954a). They established an empirical relation between the surface wind field and the slope distribution of the wave facets. In conjunction with the Fresnel reflection coefficients, the surface slope distribution can be used to derive the bidirectional reflection distribution function of the ocean surface. Owing to its small albedo and spatial uniformity, the cloud-free ocean is ideal for atmospheric remote sensing. However, the accurate treatment of the non-lambertian reflection from the ocean surface is rather complicated and requires knowledge of the surface wind field. Therefore, sun glint is often considered an obstacle, and

many remote sensing studies exclude pixels within a certain angular distance from the specular reflection point in order to avoid sun glint contamination. On the other hand, photons recorded in the sun glint region by a detector located at the top of the atmosphere bear the distinct signature of a double transmission path through the atmosphere. O'Brien and Mitchell (1988) used a simplified single-scattering model to infer wind speed and aerosol optical depth from AVHRR (Advanced Very High Resolution Radiometer) data. As pointed out in a recent study by Kaufmann et al. (2002), the sun glint radiances are particularly sensitive to aerosol extinction, whereas the radiances away from the sun glint are more sensitive to aerosol scattering. Together these informations can be used to retrieve the aerosol absorptivity. A similar approach was proposed for the retrieval of atmospheric water vapor abundance by Kleidmann et al. (2000).

1.2 Background

The atmospheric radiation budget is significantly influenced by the abundance of aerosols. Radiative forcing from aerosols occurs both directly, due to their scattering and absorption properties, and indirectly due to aerosol cloud interactions (Houghton et al., 2001). They are thought to have an overall cooling effect. Since human activities have led to a significant increase in the abundance of aerosols, the increase in the negative radiative forcing due to aerosols could offset the heating due to anthropogenic greenhouse gases.

The Indian Ocean Experiment (INDOEX) was designed as an integrated campaign to study the effects of aerosols on the earth radiation budget. As part of INDOEX, remote sensing from satellites, aircraft and ground-based,

in-situ measurements, as well as modeling studies were integrated to improve scientific understanding of aerosol climate interactions.

The extensive satellite data available for the INDOEX time and region were evaluated in several studies (Ramanathan et al., 2001b; Tahnk, 2001). The most striking result was the finding of a large aerosol loading over South Asia and the North Indian Ocean in the months from December to April, subsequently termed the Indio-Asian haze. In addition to the satellite data, aircraft-based radiometric observations were taken during INDOEX. The measurements by the Multichannel Cloud Radiometer (MCR) from the NCAR C-130 aircraft during INDOEX were performed with an ultra-high spatial resolution of approximately 30 m, and could therefore effectively complement the satellite data that were taken with a spatial resolution of 1-4 km. Since small scale clouds can be readily resolved with the MCR, the MCR data could be used to study the aerosol-cloud interaction in detail and validate methods used to derive the indirect effect of aerosols from satellite data.

Since the current calibration of the MCR instrument is not reliable, due to several gain changes during the campaign and environmental effects at flight altitude, it is necessary to analyze the calibrations and perform corrections. Sun glint was encountered in many of the scenes observed by the MCR. The goal of this thesis is to analyze the feasibility of using sun glint for relative calibrations of the wavelength channels.

1.3 Outline

This thesis describes the Monte Carlo Radiative Transfer Model MOCARAT and discusses possible applications in remote sensing. It is organized as follows:

Chapter 2 reviews the theory and basic processes of atmospheric radiative transfer that are relevant for this study as well as the Cox-Munk theory of reflection at the ocean surface. An overview of the INDOEX project, relevant aerosol theory and the MCR instrument employed for aircraft-based remote sensing is provided in Chapter 3. In Chapter 4, the Monte Carlo technique used for MOCARAT as well as the implementations of scattering, non-grey band absorption, and radiative coupling with the ocean are discussed in detail. The verification of the MOCARAT model by comparison with other, well established atmospheric radiative transfer models is presented in Chapter 5. In Chapter 6 a method for using sun glint for in-flight calibration is discussed and sensitivity studies of the proposed technique are presented. Chapter 7 concludes and summarizes the thesis and its results.

CHAPTER 2

THEORY OF ATMOSPHERIC RADIATIVE TRANSFER

The transfer of solar radiation in the earth's atmosphere is controlled by scattering and absorption, and by reflection at the lower boundary. Scattering is caused by molecules, aerosol, and cloud droplets, absorption is caused by both molecules and different kinds of aerosol. Planck emission by the atmosphere's constituents and the earth's surface is an additional source of radiation. In this study, however, only wavelengths of $2.16 \mu m$ or shorter are dealt with, which corresponds to wavenumbers $\nu = 1/\lambda$ greater than 4500 cm^{-1} . In this spectral range, for temperatures typical of the atmosphere and the earth's surface, the exponent $hc\nu/kT$ is much greater than 1, hence the Planck function

$$B_\nu d\nu = \frac{2hc^2\nu^3 d\nu}{e^{\frac{hc\nu}{kT}} - 1} \quad (2.1)$$

becomes very small compared with radiances typical of the incident sunlight. Therefore, thermal emission is insignificant and is not taken into account.

2.1 Basic Quantities

The fundamental quantity for the description of radiation in the atmosphere is the spectral radiance, or spectral intensity, defined as

$$I_\nu(\vartheta, \varphi, \nu) = \frac{dE_\nu}{\cos \vartheta dA d\nu d\Omega dt}, \quad (2.2)$$

where dE_ν is the differential amount of radiative energy, $d\nu$ the differential spectral interval, $d\Omega$ the differential solid angle, and ϑ the angle between the beam

and the normal of the detecting area, hence $\cos \vartheta dA$ consisting the differential detector area perpendicular to the beam.

The spectral amount of radiative energy per unit area and time is referred to as spectral flux density or irradiance

$$F_\nu = \frac{dE_\nu}{dA d\nu dt} = \int_0^{2\pi} \int_0^{\frac{\pi}{2}} I_\nu \cos \vartheta \sin \vartheta d\vartheta d\varphi. \quad (2.3)$$

In general, the radiative quantities I_ν, F_ν depend, in addition to the direction (ϑ, φ) and the spectral wavenumber, on the spatial coordinates. Hence, they can be considered as scalar fields in a six dimensional vector space.

The broadband quantities are defined by integration over the spectrum:

$$\begin{aligned} I(\vartheta, \varphi) &= \int I_\nu d\nu, \\ F &= \int F_\nu d\nu. \end{aligned} \quad (2.4)$$

In this study, the terms radiance and irradiance shall denote the spectral radiance or spectral irradiance integrated over the range of sensitivity of a narrow band channel.

For remote sensing studies, it is very useful to define the reflectance by means of the ratio between up-welling radiance and down-welling irradiance:

$$R(\vartheta, \varphi) = \frac{\pi I^+(\vartheta, \varphi)}{\mu_0 F_0}, \quad (2.5)$$

where the superscripts $+$, $-$ denote quantities of up-welling and down-welling radiation, respectively, μ_0 the cosine of the solar zenith angle and F_0 the solar constant.

For both scattering and absorption, according to *Beer's Law*, the differential extinction dI is proportional to the number density n of interacting particles

and the beam radiance I , and the differential geometrical length dl :

$$dI_\nu = \sigma_\nu n I_\nu dl. \quad (2.6)$$

The proportionality constant σ is the extinction cross section and has units of cm^2 . It is also common to express Beer's law in terms of the extinction coefficient c which is given by the product of the cross section and the number density

$$c_\nu = \sigma_\nu n \quad (2.7)$$

Beer's law gives rise to the definition of the optical depth τ such that

$$d\tau = -\sigma n dz. \quad (2.8)$$

In atmospheric radiation, the optical depth is often used as an alternate vertical coordinate. The minus sign in the above equation accounts for the common convention of setting the optical depth to zero at the top of the atmosphere.

In order to characterize non vertical photon paths, we shall introduce the path optical thickness τ^* as

$$\tau^* = - \int \frac{d\tau}{\mu}, \quad (2.9)$$

where the integral is performed over the photon's path.

2.2 Scattering

The angular distribution of scattered photons is described by the phase function $P(\vartheta, \varphi)$, which is normalized such that

$$\frac{1}{4\pi} \int_{4\pi} d\Omega P(\vartheta, \varphi) = 1, \quad (2.10)$$

where ϑ is the scattering angle, and φ is the azimuthal direction assigned to the plane of scattering. As the scattering particles can be assumed to be randomly oriented, the phase function depends only on the angle ϑ between the incident and the scattered light. In this case, (2.10) can be written in terms of $\mu = \cos \vartheta$ and becomes

$$\frac{1}{2} \int_{-1}^1 d\mu P_\mu(\mu) = 1. \quad (2.11)$$

Note that the phase function is proportional to the probability density per unit solid angle. Since $d\Omega = \sin \vartheta d\varphi d\vartheta$, the probability density $\Phi_\vartheta(\vartheta)$ for scattering at angle ϑ per unit scattering angle is given by

$$\Phi_\vartheta(\vartheta) d\vartheta = \frac{1}{2} P_\mu(\cos \vartheta) \sin \vartheta d\vartheta. \quad (2.12)$$

There are two different types of scattering that are relevant for radiative transport in the atmosphere and occur in different regimes of the size parameter $\alpha \equiv 2\pi R/\lambda$. *Rayleigh* Scattering occurs for $\alpha \ll 1$, whereas for *Mie* Scattering α is of order 1 or greater.

2.2.1 Rayleigh Scattering

Electromagnetic radiation incident on polarizable particles induces an oscillating dipole, which itself re-emits radiation. This effect is called Rayleigh Scattering and is confined to size regimes $\alpha \ll 1$, which applies for scattering of atmospheric radiation by molecules.

As known from classical electrodynamics, the power emitted by an oscillating dipole scales with ω^4 . Similarly, for wavelengths much shorter than the resonance wavelength an idealized particle's total cross section for Rayleigh

Scattering is proportional to λ^{-4} (Jackson, 1962, sec. 16.9). The higher scattering extinction of shorter wavelengths explains the blue color of the sky, and, likewise, the reddish color of direct sunlight when optical paths are long, particularly at sunrise and sunset. As Penndorf (1957) points out, however, the polarizability depends on the the number density and refractive index, hence also on wavelength, pressure and temperature. Therefore, the actual spectral dependence is somewhat different from the λ^{-4} -law. A higher order numerical approximation as suggested by Nicolet et al. (1982) is given by the formula

$$\sigma_R = \frac{4.0 \cdot 10^{-28}}{\lambda^{3.916+0.074 \cdot \lambda+0.005/\lambda}} [cm^2], \quad (2.13)$$

where the value of λ in μm must be used. Since the pressure and temperature effects on the scattering cross section are small, they were neglected in this study for the sake of computational simplicity.

The Rayleigh phase function depends on the orientation of the induced dipole with respect to the scattering plane. The orientation of the induced dipole gives rise to the polarization of the scattered light. As derived in the theory of an oscillating dipole, the angular distribution of the radiated power is proportional to $\sin^2 \vartheta_d$, where ϑ_d is the angle enclosed by the direction of the scattered light and the orientation of the dipole. If the induced dipole is oriented parallel to the scattering plane, the electrical vector of the emitted radiation is polarized perpendicular to the direction of propagation and parallel to the scattering plane. In this case, the scattering angle is given by $\vartheta = \vartheta_d + \pi/2$ and the phase function

$$P_{R,\parallel} \propto \sin^2 \vartheta_d = \cos^2 \vartheta_{sc} = \mu^2.$$

Radiation polarized perpendicular to the scattering plane can only be emitted by a dipole oriented perpendicular to this plane; in this case $\vartheta_d = \pi/2$ and the

phase function is constant:

$$P_{R,\perp} \propto \sin^2 \pi/2 = 1.$$

For unpolarized incident radiation the effective Rayleigh phase function is given by the normalized sum of the contributions of both polarizations:

$$P_R(\mu) = \frac{3}{4} (1 + \mu^2). \quad (2.14)$$

It is worth noting that, in the scope of classical Rayleigh theory, even for unpolarized incident radiation, Rayleigh scattered light with scattering angles of $\pi/2$ is completely polarized. In both forward and backward direction, by contrast, it is completely unpolarized.

The classical Rayleigh theory is derived considering a spherical, polarizable particle. Realistic molecules, such as N_2 and O_2 that constitute some 99 % of the dry earth atmosphere, are non-isotropic. As a consequence, the light scattered at an angle $\vartheta = \pi/2$ is not perfectly polarized. As described in Chandrasekhar (1950, sect. 18), for an analytical treatment of this effect, the anisotropy γ and the depolarization ϱ are introduced. The modified Rayleigh phase function is found to be

$$P_R(\mu) = \frac{3}{4(1+2\gamma)} (1 + 3\gamma + (1 - \gamma)\mu^2) \approx 0.7629 (1 + 0.932\mu^2) \quad (2.15)$$

where an effective anisotropy for air of $\gamma = 0.035$ (Penndorf, 1957) was used.

2.2.2 Mie Scattering

The interaction of radiation with particles of which the size can neither be considered much smaller nor much larger than the wavelength, the computation of the scattering cross section and and phase function is rather complicated.

Mie scattering is caused by interaction of radiation with a dielectric particle of size comparable to the wavelength and is therefore applicable to scattering by aerosols and clouds, whereas for very large particles, scattering can simply be considered using the laws of reflection geometrical optics. In the intermediate size regime interference effects are relevant and make a treatment in the scope of electromagnetic theory necessary.

Classical Mie Theory considers the most simple case of polarized light incident on a sphere, for which an analytical solution can be derived (e.g. Liou, 2002, ch. 5.2). This is accomplished by rewriting the Maxwell equations in spherical coordinates and performing a separation of variables. The incident and scattered electromagnetic field can then be expanded in a converging series over products in which the angular dependence is captured by spherical harmonics and the radial dependence by a Bessel function (Bohren and Huffmann, 1983, ch. 4). The far-field solution is described in terms of the two dimensionless complex scattering functions which have the symmetrical form

$$\begin{aligned} S_1(m, \alpha, \vartheta) &= \sum_{n=1}^{\infty} \frac{2n+1}{n(n+1)} [a_n \pi_n + b_n \tau_n] \\ S_2(m, \alpha, \vartheta) &= \sum_{n=1}^{\infty} \frac{2n+1}{n(n+1)} [b_n \pi_n + a_n \tau_n]. \end{aligned} \quad (2.16)$$

π_n, τ_n are functions of the scattering angle ϑ and can be written in terms of the associated Legendre Polynomials P_n^1 :

$$\begin{aligned} \pi_n(\cos \vartheta) &= \frac{1}{\sin \vartheta} P_n^1(\cos \vartheta) \\ \tau_n(\cos \vartheta) &= \frac{d}{d\vartheta} P_n^1(\cos \vartheta). \end{aligned} \quad (2.17)$$

The complex Mie coefficients a_n, b_n are functions of the size parameter α

and the refractive m only and given by

$$\begin{aligned} a_n &= \frac{\psi'_n(m\alpha)\psi_n(\alpha) - m\psi_n(m\alpha)\psi'_n(\alpha)}{\psi'_n(m\alpha)\zeta_n(\alpha) - m\psi_n(m\alpha)\zeta'_n(\alpha)} \\ b_n &= \frac{m\psi'_n(m\alpha)\psi_n(\alpha) - \psi_n(m\alpha)\psi'_n(\alpha)}{m\psi'_n(m\alpha)\zeta_n(\alpha) - \psi_n(m\alpha)\zeta'_n(\alpha)}, \end{aligned} \quad (2.18)$$

where ψ_n , ζ_n are the Riccati-Bessel functions and their derivatives (e.g. Abramowitz and Stegun, 1965, sec. 10.3), and $\alpha = 2\pi/\lambda$ is the size parameter. The formulation of the problem in terms of a complex electromagnetic field and the complex index of refraction m allows for a unified description of scattering and absorption.

The resulting scattering cross section is given by

$$\sigma_s = \frac{2\pi R^2}{\alpha^2} \sum_{n=1}^{\infty} (2n+1) (|a_n|^2 + |b_n|^2), \quad (2.19)$$

and similarly, the extinction cross section is given by

$$\sigma_e = \frac{2\pi R^2}{\alpha^2} \sum_{n=1}^{\infty} (2n+1) \operatorname{Re}(a_n + b_n). \quad (2.20)$$

Similar to Rayleigh scattering, Mie scattering also depends on the radiation's polarization relative to the scattering plane. The phase functions for radiation with the electrical vector polarized perpendicular and parallel are proportional to the square of the absolute value of the Mie scattering functions S_1 , S_2 , respectively:

$$\begin{aligned} P_{M,\perp}(\vartheta) &\propto \frac{1}{k^2} |S_1(\vartheta)|^2 \\ P_{M,\parallel}(\vartheta) &\propto \frac{1}{k^2} |S_2(\vartheta)|^2, \end{aligned} \quad (2.21)$$

where $k = 2\pi/\lambda$. This results in a normalized effective phase function for unpolarized incident light given by

$$P_M(\vartheta) = \frac{8\pi}{k^2 \sigma_s} (|S_1(\vartheta)|^2 + |S_2(\vartheta)|^2). \quad (2.22)$$

As opposed to Rayleigh scattering, a characteristic feature of Mie scattering is the strong forward peak, particularly for large particles. A number of numerical models exist to calculate scattering phase functions and cross sections. The rather complicated nature of the exact description, however, makes it desirable to parameterize the phase function in order to reduce the computational effort. The most common expression is given by the *Henyeey-Greenstein* phase function which is defined as

$$P_{HG}(\mu; g) = \frac{1 - g^2}{(1 + g^2 - 2g\mu)^{\frac{3}{2}}}, \quad (2.23)$$

where the *asymmetry parameter* g is the expectation value of μ :

$$g = \langle \mu \rangle = \frac{1}{2} \int_{-1}^1 \mu P(\mu) d\mu. \quad (2.24)$$

The Henyeey-Greenstein phase function is able to reproduce the forward peak of the actual Mie scattering reasonably well. However, in the backscattering direction, the Mie phase function exhibits a tendency to increase with scattering angle, a feature that is not captured by the Henyeey-Greenstein parameterization. Attempts have been made to account for this feature with a double Henyeey-Greenstein function of the form

$$P = b P_{HG}(\mu; g_1) + (1 - b) P_{HG}(\mu; g_2), \quad (2.25)$$

where g_1 is positive and accounts for the forward scattering, and g_2 is negative and accounts for the backscattering, and $0 \leq b \leq 1$.

The wavelength dependence of the Mie scattering coefficient is highly dependent on the particles' size. For size distributions typical of atmospheric aerosol, the scattering cross section has a strong overall tendency to decrease with wavelength at wavelengths larger than the particle size. For this regime,

a very commonly used and simple parameterization for the spectral variation of the Mie scattering optical depth is given by the Ångström power law (e.g. Satheesh et al., 1999):

$$\tau_M(\lambda) = \beta \lambda^{-\alpha}, \quad (2.26)$$

where α is the wavelength exponent, and β the turbidity parameter. Typical values for α are of the order of unity.

2.3 Absorption

Gaseous absorption occurs if a photon's energy is consumed by a molecule that makes a transition to a higher energy level. In addition to the electronic energy levels similar to those existing in atoms, molecules can have energy levels corresponding to different vibrational and rotational states. Electronic transitions are of the order of few eV, which corresponds to photon wavenumbers $\nu = \Delta E/hc$ of some 10^4 cm^{-1} . By contrast, the energy difference between neighboring vibrational states are typically 10^3 cm^{-1} , and rotational transitions are of the order of a mere 1 cm^{-1} . Since a change of the vibrational state induces a change of the molecule's moment of inertia, vibrational transitions are always coupled with rotational transitions. These can be observed as groups of lines in the near intermediate IR that are known as vibrational-rotational bands.

It is well known from quantum mechanics that radiative transitions can only occur if the corresponding dipole matrix element is non-zero. For symmetric, homonuclear molecules such as N_2 or O_2 , the dipole moment is zero for all electronic quantum states. Hence, there are no pure vibrational-rotational or rotational transitions for those molecules, and they are virtually inactive in the infrared region.

Asymmetric molecules such as H_2O and O_3 have dipole moments. They are radiatively active in the IR and have extensive absorption structures due to the variety of possible vibrational and rotational excitations.

The dipole moment of the ground state of the symmetrical polynuclear molecules CO_2 and CH_4 is zero. However, there are asymmetrical stretching and bending modes that result in an electric dipole moment, which gives rise to these molecules' vibrational-rotational spectra in the IR and their relevance as greenhouse gases.

For an isolated molecule, the natural linewidth is determined by the lifetime of the excited state, which is inversely proportional to the square of the transition matrix element. Real molecules have a finite temperature and are subject to collisions with other molecules, which results in broadening of the absorption lines. The emission frequency of a photon emitted by a molecule that is in motion with respect to the observer will be shifted due to the Doppler effect. The gas molecule velocity distribution is given by the Maxwell-Boltzmann distribution

$$p(v_x) = \sqrt{\frac{m}{2\pi kT}} e^{-\frac{mv_x^2}{2kT}}, \quad (2.27)$$

where k is Boltzmann's constant, T is the temperature, m is the molecule's weight, and v_x is the longitudinal velocity, i.e. the component parallel to the propagation of the photon. Since the Doppler shift is proportional to the longitudinal velocity

$$\delta\nu = \nu_0 \frac{v}{c} \quad \text{for } v \ll c, \quad (2.28)$$

the shape of the Doppler broadened line is a Gaussian and the line width is given by

$$\alpha_D = \nu_0 \sqrt{\frac{2kT}{mc^2}}. \quad (2.29)$$

The lifetime of an excited state is shortened in the presence of other molecules due to collisions. In addition, due to intermolecular forces during a collision, the energy levels are shifted. These effects on the molecular spectra are referred to as pressure broadening. The shape of a pressure broadened line is given by the Lorentz-profile, the Fourier-transform of an exponentially damped harmonic oscillation:

$$\Phi_L(\nu) = \frac{\gamma}{4\pi^2 \left[(\nu_0 - \nu)^2 + \left(\frac{\gamma}{4\pi}\right)^2 \right]}, \quad (2.30)$$

where γ is the damping parameter and ν_0 the frequency of the line center.

Pressure and temperature broadening give rise to the change of the molecular absorption cross sections over the vertical atmospheric profile and the transition from groups of individual absorption lines to continuously absorbing bands.

Apart from gaseous absorption, absorption can also occur in aerosol and cloud particles. A commonly used quantity to characterize the absorption by particles is the single scattering albedo ω_{aer} , which is given by the ratio of scattering cross section to the sum of scattering and absorption cross sections

$$\omega_{aer} = \frac{\sigma_s}{\sigma_s + \sigma_a}. \quad (2.31)$$

Typical values for ω at visible wavelength range from 0.2 to values of practically 1 for cloud droplets.

2.4 The Equation of Radiative Transfer

The quantities describing scattering and absorption introduced in the previous two sections enable us to formulate the equation of radiative transfer, which gives the spatial variation of the radiance field.

For a horizontally uniform atmosphere, the equation of radiative transfer is given by

$$\frac{1}{\mu} \frac{dI_\nu(\vartheta, \varphi, \tau)}{d\tau} = I_\nu(\vartheta, \varphi, \tau) - J_\nu(\vartheta, \varphi, \tau) \quad (2.32)$$

where the first term on the right hand side refers to the extinction according to Beer's law, whereas the second term J accounts for sources of radiation in the direction (ϑ, φ) . Possible source mechanisms are thermal radiation and scattering. Note that the negative sign in front of the source term arises due to the conventions that the optical depth decrease downward, and negative values of μ correspond to downwelling radiation. In the case of thermal emission, the source term is given by the Planck law (2.1).

Since the transfer of solar radiation is being studied, a scattering atmosphere without thermal emission is considered. The scattering source term can be calculated from the phase function:

$$J_{sc} = \frac{\omega_e}{4\pi} \int_{-1}^1 d\mu' \int_0^{2\pi} d\varphi' p(\vartheta', \varphi'; \vartheta, \varphi, \tau) I(\vartheta', \varphi', \tau). \quad (2.33)$$

The effective single scattering albedo ω_e must be defined to account for both molecular and aerosol absorption:

$$\omega_e = \frac{\tau_R + \tau_{aer} \omega_{aer}}{\tau_{aer} + \tau_{abs} + \tau_R}, \quad (2.34)$$

where τ_{aer} is the aerosol's extinction optical depth, and τ_{abs} is the optical depth of the molecular absorption. τ_R accounts for the Rayleigh scattering, which is conservative and therefore has a single scattering albedo of 1.

Given the scattering and absorption properties of the interior of the atmosphere, it is necessary to specify the boundary conditions before the equation of radiative transfer can be solved for the radiance field. At the top of the atmosphere, the downwelling radiation is simply given by the insolation. At the

lower boundary, by contrast, the upwelling radiance depends on the properties of the surface.

2.5 Radiation from the Ocean

For an ocean surface as a lower boundary, the upwelling radiation from the ocean can be described in terms of the following basic physical processes: Its major portion is due to specular reflection of downwelling direct sunlight at the wavy ocean surface. In addition, diffuse, previously scattered light incident on the ocean surface is reflected (“sky glint”). Sky glint can be described analogously to the reflection of direct sunlight. Dependent on parameters such as wavelength, salinity and content of dissolved particles, radiation transmitted into the ocean interior is partially scattered back and can also contribute significantly the observed atmospheric radiation (e.g. Walker, 1994).

2.5.1 Bidirectional Reflectance at the Ocean’s Surface

In a pioneering study, Cox and Munk (1954a) explored the radiative properties of the ocean’s surface from comparisons of aerial photographs with wind speed measurements at the surface. They derived an analytical model for the sea surface reflectance based on *Fresnel’s* equations and the distribution for the orientation of reflecting surface irregularities called facets. It was found that the distribution of wave slopes can be reasonably well approximated by a Gaussian function. For steady winds, the mean square slope in the along wind direction, σ_u^2 , is somewhat greater than the mean square slope in the cross wind direction, σ_c^2 . Lines of equal probability in the two-dimensional slope space therefore give

rise to an ellipsis. Cox and Munk's observations demonstrate nicely, that for small solar zenith angles, for which the Fresnel reflectance is almost constant over the sun glint domain, the reflection pattern is elliptical with the longer principal axis aligned with the wind. In the Gaussian approximation, the slope probability distribution is given by

$$p_s(z_x, z_y) = \frac{1}{2\pi\sigma_u\sigma_c} e^{-\frac{1}{2}\left(\frac{z_x^2}{\sigma_u^2} + \frac{z_y^2}{\sigma_c^2}\right)}, \quad (2.35)$$

where $z_x = \frac{\partial z}{\partial x}$, $z_y = \frac{\partial z}{\partial y}$ are slopes in x - and y -direction, respectively. Cox and Munk (1954a) obtained a linear parameterization for the mean square slopes in terms of the wind speed w (m/s):

$$\begin{aligned} \sigma_u^2 &= 0.003 + 0.00192 w \pm 0.004 \\ \sigma_c^2 &= 0.000 + 0.00316 w \pm 0.002. \end{aligned} \quad (2.36)$$

The Gaussian distribution (2.35) reproduces the data reasonably well. However, in order to account systematically for the small but significant deviations of the observed slope distribution from Gaussian, Cox and Munk (1954b) modified (2.35) by expanding the distribution in a Gram-Charlier series (see e.g. Khuri, 2003, for reference), where higher order corrections are imposed by multiplication of the two-dimensional Gaussian with a sum of products of Hermite-Polynomials in the variables $\xi = \frac{z_x}{\sigma_u}$ and $\eta = \frac{z_y}{\sigma_c}$:

$$p_{GC}(z_x, z_y) = \frac{1}{2\pi\sigma_u\sigma_c} e^{-\frac{1}{2}(\xi^2 + \eta^2)} \sum_{i,j=0}^{\infty} c_{ij} H_i(\xi) H_j(\eta). \quad (2.37)$$

The coefficients c_{ij} can be related to the central moments of the distribution (Khuri, 2003, sec. 10.9). The formulation with the parameters ξ , η has an expectation value of 0, and variance of unity. It can be shown that in this case

(Cox and Munk, 1954a)

$$\begin{aligned} c_{00} &= 1 \\ c_{01} &= c_{10} = c_{02} = c_{20} = 0 \end{aligned} \quad (2.38)$$

Additional simplification arises due to the symmetry in the cross wind direction, which implies that the terms involving polynomials with odd parity in η vanish. Hence the resulting distribution with corrections up to fourth order is given by (Cox and Munk, 1954a)

$$\begin{aligned} p(z_x, z_y) &= \frac{1}{2\pi\sigma_u\sigma_c} e^{-\frac{1}{2}(\xi^2+\eta^2)} \left[1 - \frac{1}{2}c_{12}(\eta^2-1)\xi - \frac{1}{6}c_{30}(\xi^3-3\xi) \right. \\ &+ \frac{1}{24}c_{40}(\xi^4-6\xi^2+3) + \frac{1}{4}c_{22}(\xi^2-1)(\eta^2-1) \\ &\left. + \frac{1}{24}c_{04}(\eta^4-6\eta^2+3) + \dots \right]. \end{aligned} \quad (2.39)$$

The numerical values for the coefficients c_{ij} were also determined as part of the Cox and Munk study:

$$\begin{aligned} c_{12} &= 0.01 - 0.0086 w \pm 0.03 \\ c_{30} &= 0.04 - 0.033 w \pm 0.12 \\ c_{04} &= 0.40 \pm 0.23 \\ c_{22} &= 0.12 \pm 0.06 \\ c_{40} &= 0.23 \pm 0.41. \end{aligned} \quad (2.40)$$

These values are relatively small and depend critically on the spatial uniformity of the wind field, accurate knowledge of the wind direction etc., which explains the low accuracy of the regressions.

For many applications in remote sensing, the wind direction is not specified, because the wind direction over the domain where the sun glint is observed is

not uniform, not known, or simply cannot be retrieved from the data. In the absence of information on wind direction, an isotropic slope distribution of the form

$$p_s(z_x, z_y) = \frac{1}{\pi\sigma^2} e^{-\frac{z_x^2+z_y^2}{\sigma^2}} \quad (2.41)$$

can be assumed (e.g. Takashima, 1985), where σ^2 is the mean square of the total slope:

$$\sigma^2 = \langle z_x^2 + z_y^2 \rangle = 0.003 + 0.00512 w \pm 0.004. \quad (2.42)$$

Since the eccentricity of the ellipses of equal slope probability, given by

$$e = \sqrt{1 - \frac{\sigma_c^2}{\sigma_u^2}}, \quad (2.43)$$

is of the order of 0.6, the deviation of (2.41) from (2.35) is not insignificant. The influence of the isotropy assumption on model results and applications is discussed in Section 6.2.3.

In order to determine the probability density of wave facets oriented such that a photon incident at angles (ϑ, φ) is reflected into direction (ϑ', φ') , the slopes z_x, z_y must be calculated from the photon geometry. Let

$$\begin{aligned} \vec{v} &= \begin{pmatrix} \cos \varphi \sin \vartheta \\ \sin \varphi \sin \vartheta \\ \cos \vartheta \end{pmatrix}, \\ \vec{v}' &= \begin{pmatrix} \cos \varphi' \sin \vartheta' \\ \sin \varphi' \sin \vartheta' \\ \cos \vartheta' \end{pmatrix} \end{aligned} \quad (2.44)$$

be the normalized vectors of incidence and reflection (see Figure 2.1). The reflection law implies that the wave facet must be oriented such, that its normal

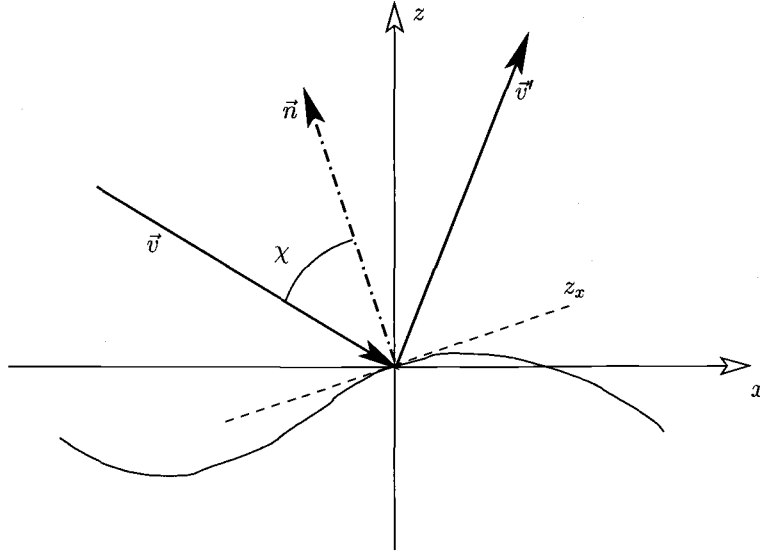


FIGURE 2.1: Geometry of the reflection at the ruffled ocean surface.

vector \vec{n} is collinear with the difference between \vec{v} , \vec{v}' :

$$\vec{n} \propto \vec{v}' - \vec{v} = \begin{pmatrix} \cos \varphi' \sin \vartheta' - \cos \varphi \sin \vartheta \\ \sin \varphi' \sin \vartheta' - \sin \varphi \sin \vartheta \\ \cos \vartheta' - \cos \vartheta \end{pmatrix}. \quad (2.45)$$

From geometrical considerations, the slopes of the surface is then simply given by the ratios of the components of \vec{n} as

$$\begin{aligned} z_x &= -\frac{n_x}{n_z} = \frac{\cos \varphi \sin \vartheta - \cos \varphi' \sin \vartheta'}{\cos \vartheta' - \cos \vartheta} \\ z_y &= -\frac{n_y}{n_z} = \frac{\sin \varphi \sin \vartheta - \sin \varphi' \sin \vartheta'}{\cos \vartheta' - \cos \vartheta}. \end{aligned} \quad (2.46)$$

The actual reflection probabilities for given reflection geometries must be calculated by also accounting first for the reflection coefficient of the sea surface and second for the size of the projected area normal to the incoming beam. Both

are functions of the angle χ_i between the incoming beam and the vector normal to the reflecting surface. Again, by applying the reflection law, χ_i is related to the scalar product between \vec{v} , \vec{v}' :

$$\cos(2\chi_i) = -\vec{v} \cdot \vec{v}' = -\cos \vartheta \cos \vartheta' - \sin \vartheta \sin \vartheta' \cos(\varphi - \varphi'). \quad (2.47)$$

The *Fresnel* reflection coefficient is derived using continuity conditions of the tangential and normal components of the electromagnetic field across the interface (e.g. Jackson, 1962, sect. 7.5). It is therefore dependent on the polarization of the incident beam. If the electric field vector is parallel to the plane of incidence, it is given by

$$\varrho_{\parallel}(\chi_i) = \frac{\tan^2(\chi_i - \chi_t)}{\tan^2(\chi_i + \chi_t)}, \quad (2.48)$$

where the transmission angle χ_t can be obtained from *Snell's* law

$$\sin \chi_i = m \sin \chi_t \quad (2.49)$$

and m is the ratio of indices of refraction across the interface. Similarly, for light polarized perpendicular to the plane of incidence

$$\varrho_{\perp}(\chi_i) = \frac{\sin^2(\chi_i - \chi_t)}{\sin^2(\chi_i + \chi_t)}. \quad (2.50)$$

Note that these relationships give rise to the very high degree of polarization observed in the reflected light. At the *Brewster* angle, given by

$$\chi_B = \arctan(m) \quad (2.51)$$

the reflection coefficient $\varrho_{\parallel}(\chi_B) = 0$. Light reflected at this angle is fully polarized. For water, the Brewster angle $\chi_B \approx 53^\circ$.

For natural, i.e. unpolarized, light the effective reflection coefficient $\varrho(\chi_i)$ is simply given by

$$\begin{aligned}\varrho(\chi_i) &= \frac{1}{2} (\varrho_{\perp} + \varrho_{\parallel}) \\ &= \frac{1}{2} \left(\frac{\sin^2(\chi_i - \chi_t)}{\sin^2(\chi_i + \chi_t)} + \frac{\tan^2(\chi_i - \chi_t)}{\tan^2(\chi_i + \chi_t)} \right).\end{aligned}\quad (2.52)$$

A derivation of the *Fresnel* reflectance from basic electrodynamic proportional to the cosine of the zenith angle of the reflected radiance.

Note that the index of refraction of saltwater is different from that of freshwater. This can be accounted for by introducing an additive correction term to the real part that scales approximately linearly with the salinity:

$$m_{sea} = m_w + \Delta \cdot \frac{s}{s_0}, \quad (2.53)$$

where s is the salinity, and the standard salinity is taken to be $s_0 = 34.3$ g/kg. The reported values for the correction Δ are about $7 \cdot 10^{-3}$ for the visible spectral range (Dorsey, 1940) and $6 \cdot 10^{-3}$ for the near IR (Friedmann, 1969). The salinity effect changes the the refractive index by a mere 0.5 %, however it yields a relative deviation of 3% in the Fresnel reflectance (2.52) for light incident at an angle of 45° or smaller and is therefore significant particularly for the sun glint radiances.

The number of photons incident on a tilted wave slope is proportional to the area normal to the incident beam. For a given surface area dA the area projected normal is given by $dA_{\perp} = \cos \chi_i dA$, where χ_i is the reflection angle. (2.39) must therefore be weighed with this factor of $\cos \chi_i$ and the Fresnel reflectance in order to yield the probability that an individual photon incident at (ϑ, φ) is reflected into (ϑ', φ')

$$P_{CM}(\vartheta, \varphi; \vartheta', \varphi') = \frac{\varrho \cos \chi_i}{C} p(z_x, z_y) \quad (2.54)$$

where the normalization constant C is defined by the condition

$$\int_0^{\frac{\pi}{2}} d\vartheta' \int_0^{2\pi} d\varphi' \sin \vartheta' P(\vartheta, \varphi; \vartheta', \varphi') = 1.$$

For geometries with sufficiently high elevation angles for the incident and reflected radiation, Cox-Munk theory performs very well. However, it is limited by the omission of effects due to the shadowing of wave facets by adjacent slopes as well as multiple reflections, which makes its predictions less reliable for low elevation angles. In this study, sun glint reflectance is only explored for nadir looking radiometers where these effects are indeed small.

Often, the properties of a non-isotropically reflecting surface are described by means of the *bidirectional reflectance distribution function (BRDF)* which relates the outgoing radiance to the incoming radiance. Whereas the reflectance (2.5) is defined for light incident from a discrete direction, the *BRDF* is defined analogously for diffuse incident radiation:

$$BRDF(\vartheta, \varphi; \vartheta', \varphi') := \frac{dI_{out}(\vartheta', \varphi'; \vartheta, \varphi)}{I_{in}(\vartheta, \varphi) \cos \vartheta d\omega}, \quad (2.55)$$

where $I_{out}(\vartheta', \varphi')$ is the reflected radiance, $I_{in}(\vartheta, \varphi)$ is the incident radiance, and $d\omega$ the differential solid angle of the incident light (Thomas and Stamnes, 1999, sec. 5.2.4). This definition takes into account that the incremental reflected upwelling radiance from a particular incident direction scales with the radiance from that direction and the differential incident solid angle. The number of photons from direction (ϑ, φ) incident on a reflecting surface area with normal in the z -direction is proportional to $I(\vartheta, \varphi) \cos \vartheta$. Similarly, per unit solid angle of the detector the observed reflecting surface area with normal in the z -direction is inversely proportional to the cosine of the zenith angle of the reflected radiance. Therefore, the ratios of incident and reflected radiance in (2.55) can be converted

into photon fluxes, N_{out} , N_{in} , by a multiplicative factor of $\frac{\cos \vartheta}{\cos \vartheta'}$:

$$\frac{dN_{out}}{N_{in}} = \frac{\cos \vartheta' dI_{out}}{\cos \vartheta I_{in}}. \quad (2.56)$$

The resulting *BRDF* derived from (2.54) is hence given by

$$BRDF(\vartheta, \varphi; \vartheta', \varphi') = \frac{P_{CM}(\vartheta, \varphi; \vartheta', \varphi')}{\cos \vartheta'} = \frac{\varrho \cos \chi_i}{C \cos \vartheta'} p(z_x, z_y). \quad (2.57)$$

2.5.2 Upwelling Radiation from the Ocean Interior

In addition to reflected light, photons transmitted into the ocean interior and scattered back into the atmosphere contribute to the observed radiance. Whereas Cox and Munk (1954a) found this effect to be negligible in the sun glint region, it can be comparable to the contribution from reflected diffuse sky light, i.e. sky glint, and therefore non-negligible away from the sun glint.

The oceanic radiative transfer is nicely described in Walker (1994, ch. 5). The results that are the most relevant for this study shall be briefly reviewed in this section. Similar to the atmosphere, radiative transfer in the ocean is controlled by conservative Rayleigh scattering and absorption by the water molecules, as well as Mie Scattering and absorption by dissolved particles, called hydrosols.

The Rayleigh scattering coefficient for water b_w , defined analogously to the extinction cross section (2.7), also follows an approximate λ^{-4} law:

$$b_w \approx b_w(\lambda_0) \left(\frac{\lambda_0}{\lambda} \right)^4. \quad (2.58)$$

For $\lambda_0 = 500$ nm, whereas $b_w(\lambda_0)$ equals 0.022 m^{-1} for freshwater, the value for saltwater, which was used for this study, is about 0.0029 m^{-1} . The water's absorption coefficient a_w varies enormously with wavelength. It reaches its

minimum of 0.145 at about 440 nm, however for 640 nm it is as large as 0.39 m^{-1} and exceeds 2 m^{-1} in the near IR. Since a_w is more than an order of magnitude larger than b_w for most of the spectrum, the subsurface reflectance of pure water becomes very small. For ocean water, however, the amount of light reflected back to the atmosphere can significantly increase in the presence of biogenic matter that act as scattering hydrosols. Most important is scattering and absorption of phytoplankton. Phytoplankton is photosynthetically active and its pigments have a strong absorption band in the blue (≈ 440 nm) and a somewhat weaker one in the red (≈ 675 nm). Other, typically somewhat less important hydrosols are detritus and dissolved organic matter (DOM). Their absorption coefficients decrease approximately exponentially with wavelength.

The scattering coefficient of the biogenic material can be approximated by a power law of the form

$$b_{bio}(\lambda) \approx b_w(\lambda_0) \left(\frac{\lambda_0}{\lambda} \right)^\beta. \quad (2.59)$$

Since the hydrosols are typically large in size, the exponent β is of order unity. The scattering phase function is strongly forward peaked, with an asymmetry parameter g_{bio} of typically 0.95.

For a given wavelength, the scattering coefficient can be empirically related to the water's chlorophyll content, again by using a power law. The resulting expression becomes

$$b_{bio}(\text{Chl}, \lambda) \approx 0.30 \text{ Chl}^{0.62} \left(\frac{550}{\lambda} \right), \quad (2.60)$$

where λ must be specified in nm, the chlorophyll concentration Chl in (mg/m^3), and the scattering coefficient is in m^{-1} .

As shown by a number of simulations based on explicit models of the radiative transfer in the ocean, for small solar zenith angles the upwelling radi-

ance from the ocean interior is almost constant with viewing geometry (e.g. Takashima, 1985; Walker, 1994, ch. 10). Its contribution to the reflectance can therefore be described as quasi-Lambertian.

For Lambertian surfaces the intensity of the reflected light is isotropic. The *BRDF* is hence constant, and it is equal to the albedo. In analogy to (2.57), the lambertian photon reflection probability distribution is given by

$$P_L(\vartheta, \varphi; \vartheta', \varphi') = \frac{\alpha}{\cos \vartheta'}, \quad (2.61)$$

where α is the Lambertian albedo. The full ocean system's reflection probability distribution is then given by the sum of specular reflection contribution P_{CM} and the quasi-Lambertian contribution P_L of the transmitted diffuse light.

CHAPTER 3

THE INDIAN OCEAN EXPERIMENT (INDOEX)

The Indian Ocean Experiment (INDOEX) was designed to study intensively the effects of aerosols on the earth radiation budget and climate, integrating field measurements with satellite observations and model studies. In the southern hemisphere, the tropical Indian Ocean is virtually free of any land masses from 40 °E to 100 °E and therefore largely dominated by pristine marine air. In the northern hemisphere, by contrast, the Indian Ocean adjoins the Asian continent at about 20 °N and is influenced by the presence of the Indian subcontinent. The atmosphere of the tropical northern Indian Ocean is heavily polluted with mostly anthropogenic aerosol from the continent. Due to the separation by the intertropical convergence zone (ITCZ), there is only little exchange between the air masses of the southern and northern hemisphere. Therefore, with other atmospheric parameters being very similar, there is a sharp contrast in aerosol loading across the ITCZ. Hence the tropical Indian Ocean offers a unique “natural laboratory” to study the radiative forcing due to aerosols and its effects on climate (Ramanathan et al., 1996).

During the two major field phases of INDOEX in February through March 1998 and January through March 1999, radiation data as well as measurements of aerosol and chemistry were taken from several aircraft, satellites and ground-based instruments. The goal of this thesis is to accurately model the radiance field observed by the Multichannel Cloud Radiometer (MCR), which was flown on the NCAR C-130 during the intensive field phase in 1999.

3.1 Aerosol Climate Interactions

Whereas the radiative forcing due to the change in abundance of atmospheric trace gases, such as CO₂, CH₄, N₂O, O₃ and halocarbons, is reasonably well understood, major uncertainty in the estimation of the anthropogenic radiative forcing arises due to the low-level of scientific understanding of the radiative forcing of aerosols.

Aerosols can affect climate in different ways. Following Ramanathan et al. (2001b), the major effects shall be referred to as direct effect, first and second indirect effect, and semi-direct effect. The direct effect describes the net forcing due to increased scattering and absorption of shortwave radiation (negative forcing at the surface) and absorption of outgoing longwave radiation (positive forcing). The net effect of the forcing depends critically on the optical properties of the aerosol, particularly its single scattering albedo. Black carbon aerosol, for instance, which has very high absorptivity, induces a positive forcing, whereas most other aerosols (e.g. sulphate, organic carbon) have a negative direct forcing (Haywood and Boucher, 2000).

The two indirect effects describe the influence of aerosols on clouds. Due to increased abundance of aerosols serving as cloud condensation nuclei more cloud droplets form, but the droplets are smaller. Assuming constant liquid water, these changes result in an overall increase of the cloud albedo and a negative forcing. This is referred to as the first indirect effect or Twomey effect (Twomey, 1977). In addition to the change in cloud albedo, the suppression of larger drops could result in a decrease of cloud precipitation, thus increasing cloud lifetime and liquid water content. This process is referred to as the second indirect effect which further increases the negative forcing.

It is important to note that the lifetime of aerosols is of the order of several days, much smaller than lifetimes of many years to decades for most of the greenhouse gases mentioned earlier. Because of the short lifetimes, the regional and seasonal patterns of the aerosol forcing are highly variable. Whereas the global mean aerosol forcing is estimated at a few W/m^2 , it can be much higher in regions with heavy air pollution, such as southeast Asia, where the surface forcing is found to be as high as $20 \text{ W}/\text{m}^2$ (Ramanathan et al., 2001b; Tahnk, 2001). Furthermore, whereas greenhouse gases such as CO_2 build up in the atmosphere, there is no such accumulation effect for aerosol, i.e. the aerosol forcing depends only on current emissions.

Aerosol pollution might also have an enormous impact on regional hydrological cycles. The drizzle suppression that gives rise to the second indirect effect is only one example of possible hydrological impacts. The reduction of sunlight at the surface decreases evaporation and hence the atmospheric water content available for precipitation (Ramanathan et al., 2001b). For absorbing aerosols, there is positive radiative forcing in the atmosphere, which in conjunction with the negative surface forcing could alter the stability of the atmosphere. The potential impacts on precipitation from deep convection remain largely unexplored.

The analysis of the data gathered by the aircraft-borne Multichannel Cloud Radiometer are of key interest for the understanding the relationship between aerosol and the properties of nearby clouds. Since the MCR has an ultra-high resolution of up to 30 m, small scale patterns in the clouds can be resolved, and the separation between cloudy sky and clear sky pixels is far superior to that achieved in the relatively coarse resolution of satellite radiometers (4 km). MCR observations could prove extremely valuable for addressing the problem

of possible cloud contamination in the pixels used to determine aerosol burden, as well as for the analysis of interactions between clouds and the aerosol in the nearby air.

3.2 Aerosol Sources

There is a wide variety of sources for atmospheric aerosol, both natural and anthropogenic. The atmospheric aerosol load is thought to have significantly increased due to anthropogenic activity. Besides primary aerosols, which are emitted directly from the source, there are also secondary aerosols which are formed from gaseous precursors through gas-to-particle conversion. The major aerosol species include sulfate aerosol, black carbon, organic carbon, mineral dust, nitrate aerosol, and sea salt aerosol.

Sulphate aerosols are mostly formed as secondary aerosols from SO_2 , which originates from anthropogenic pollution (e.g. combustion) or natural sources such as volcanic eruptions or wildfires. In addition, dimethyl sulfide (DMS), which is emitted from marine phytoplankton, is converted to sulphate aerosols by gas-to-particle conversion and contributes significantly to the aerosol budget over the ocean. Black Carbon (BC), also referred to as soot, is emitted as a primary aerosol from incomplete combustion processes. Even though naturally occurring biomass fires do occur, most of the BC stems from anthropogenic sources such as fossil fuels. Due to its particularly high absorptivity, BC abundance is particularly significant for the radiative properties of an aerosol layer. Organic carbon (OC) aerosol can be emitted directly as primary particles or from gaseous emissions as secondary particles. The major sources for OC are burning of fossil fuel and biomass, as well as oxidation of volatile organic com-

pounds (VOC). Additional natural sources include debris, pollen, spores, and algae (Houghton et al., 2001, sec. 5.2.2.).

Mineral dust is generated by wind erosion. Anthropogenic activity and land-use changes might significantly enhance its abundance. Sokolik and Toon (1996) estimate that between 20 and 50 % of the mineral dust aerosols are due to human activity. Mineral dust particles are coarse mode aerosol with typical radii larger than 1 μm . When at high altitudes, as in the case of windblown desert dust, they interact with IR radiation and induce a significant longwave forcing.

Sea salt aerosols are created mostly by bursting of air bubbles during white cap formation. Their rate of production is therefore very dependent on wind speed. Commonly, a distinction is made between the aerosols originating from the small film droplets and those originating from the few large jet drops in the center of the bubble. Due to their high hygroscopy, sea salt aerosol are particularly efficient as droplet condensation nuclei. However, jet drop aerosol and even film droplet aerosol are typically too large to survive at altitudes where cloud formation is relevant.

3.3 Aerosol Types for INDOEX

A comprehensive characterization of the atmospheric aerosol requires detailed information on size distribution, ratio of different aerosol components as well as internal chemical composition, and vertical profile. These parameters are highly variable and depend not only on the particle's sources and age but also on external factors such as the relative humidity of the ambient air. It is impossible to obtain all the properties of the atmospheric aerosol from remote sensing, since only a limited number of radiometric channels and hence only lim-

ited information is available for the retrieval. Therefore, *a priori* assumptions must be made to obtain a low order parameterization of the aerosol radiative properties. For this study, OPAC (Optical Properties of Aerosol and Clouds) standard aerosol models were used (Hess et al., 1998).

A very simple form of the aerosol size distribution is given by the *Junge Power Law* (e.g. Wallace and Hobbs, 1977)

$$\frac{dn(r)}{d \log r} = C r^{-\beta} \quad (3.1)$$

where n is the number of particles per unit volume, r is the particle radius and C is a normalization constant. For most aerosol types, the exponent $\beta \approx 3$ for the major part of the size spectrum, yielding a strongly decreasing aerosol number distribution with radius.

Apart from the above number distribution, it is worth considering the distribution of aerosol volume, which is expected to scale with $dV/d \log r \propto r^{3-\beta}$ according to Junge's law. Due to small fluctuations in the exponent β , rather than being approximately constant, the mass distribution reveals a multi-modal structure with two to three distinct maxima.

The smallest aerosol with radii below $0.02 \mu\text{m}$ are called *Aitken Particles*. They originate from gas to particle conversion and form the nucleation mode. The Aitken particles coagulate very efficiently to larger particles and hence their typical lifetime is only a few hours. Therefore the nucleation mode of the size distribution becomes less distinct and eventually disappears as the air mass moves away from the source.

Whereas small aerosols coagulate very efficiently and grow quickly in size, particle growth by coalescence with other particles is much slower in the intermediate size range. This gives rise to the accumulation mode. The accumulation

particles radii range from about $0.05 \mu\text{m}$ to to about $0.5 \mu\text{m}$. Apart from soot, organic species, and sulfates, that mostly originate from combustion processes, the small-sized sea salt aerosol that originate from film droplets belong to the accumulation mode.

The mode of the largest aerosols ranges from about $1 \mu\text{m}$ to $10 \mu\text{m}$. It is referred to as the coarse mode and represents mostly mechanically generated particles such mineral dust, and the large sea salt particles, generated from evaporated jet drops, in addition to fly ash.

For each of the different modes and components, the particle size distribution can be reasonably described by the log-normal distribution (e.g. Satheesh et al., 1999):

$$\frac{dn_i(r)}{dr} = \frac{n_i}{\sqrt{2\pi} r \ln(10) \log \sigma_i} e^{-\frac{1}{2} \left(\frac{\log r - \log r_i}{\log \sigma_i} \right)^2}, \quad (3.2)$$

where the free parameters are the mode's total particle number density n_i , the radius r_i , and the width of the distribution σ_i , which is dimensionless.

The different OPAC aerosol components and modes that were used for this study are listed in Table 3.1. The water soluble and insoluble components account for a variety of different species. The water insoluble component groups aerosol species with a certain amount of organic material, mostly originating from soil particles, vegetation and combustion. The water soluble component consists of various kinds of sulfates and nitrates. It also accounts for the aerosol from DMS produced over the ocean.

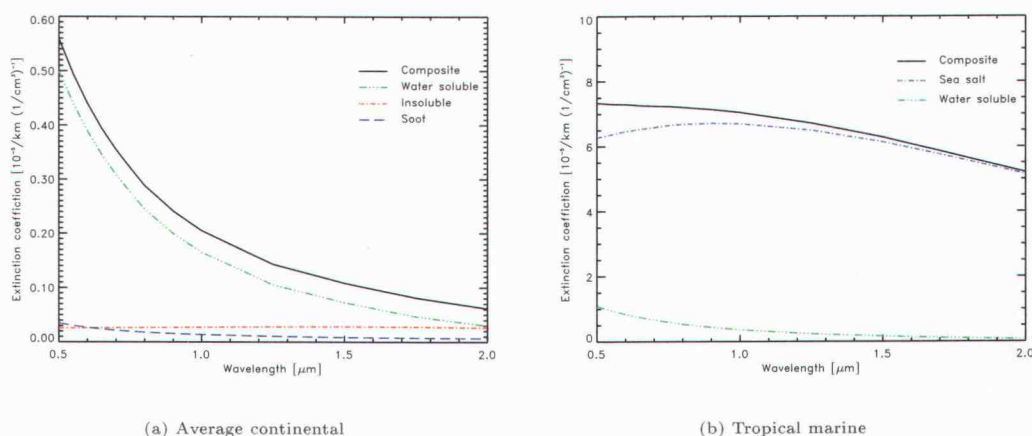
Note that for hygroscopic particles, such as the sea salt aerosol and the other water soluble species, the size distribution depends on the relative humidity. The equilibrium water vapor pressure over the haze droplet's surface is reduced by the solute effect due to the hygroscopic nucleus and increased by

TABLE 3.1: Microphysical parameters for the different aerosol components taken from Hess et al. (1998). The refractive index is given at a reference wavelength of $0.55 \mu\text{m}$.

Aerosol component	Mode radius r_i [μm]	Width σ_i	Refractive index		Aerosol mass [[$\mu\text{g m}^{-3}$]/(part. cm^{-3})]
			m_r	m_i	
Water insoluble	0.471	2.51	1.53	$- 8.0 \cdot 10^{-3}$	2.37
Water soluble					
<i>dry</i>	0.0212	2.24	1.53	$- 6.0 \cdot 10^{-3}$	$1.34 \cdot 10^{-3}$
<i>80% rel. hum.</i>	0.0306		1.40	$- 1.7 \cdot 10^{-3}$	
Sea salt (acc. mode)					
<i>dry</i>	0.209	2.03	1.50	$- 1 \cdot 10^{-8}$	$8.02 \cdot 10^{-1}$
<i>80% rel. hum.</i>	0.416		1.354	$- 2.9 \cdot 10^{-9}$	
Sea salt (coarse mode)					
<i>dry</i>	1.75	2.03	1.50	$- 1 \cdot 10^{-8}$	$2.24 \cdot 10^2$
<i>80% rel. hum.</i>	3.49		1.354	$- 2.9 \cdot 10^{-9}$	
Soot	0.0118	2.00	1.75	$- 0.45$	$5.99 \cdot 10^{-5}$

the curvature effect. Both effects depend on the droplet radius. For sufficiently small particles, according to the *Köhler* theory, the particle grows with increasing relative humidity (e.g. Pruppacher and Klett, 1978; Rogers and Yau, 1989). As the condensation nuclei become more and more diluted, this effect also alters the particle's index of refraction.

FIGURE 3.1: Spectral dependence of the extinction coefficient per unit aerosol number concentration for the average continental (a) and tropical marine (b) aerosol model. The contributions of the various components are plotted in color.



To describe the real atmosphere, it is necessary to account for mixtures of the different aerosol components. Depending on the geographical conditions, Hess et al. (1998) proposed different models that represent typical aerosol compositions. The aerosol models adapted for this study are *tropical marine* and *average continental*. For simulations of radiances in the pristine air of the southern hemisphere, the *tropical marine* aerosol model was used. The aerosol is

TABLE 3.2: Optical properties of the composite aerosol models (Hess et al., 1998; Coakley et al., 2002). The values are given for a reference wavelength of $0.65 \mu\text{m}$. The relative humidity was considered to be 80 % for the hygroscopic species. Ångström coefficients were calculated for the $0.64 \mu\text{m}$ to $1.64 \mu\text{m}$ range.

Aerosol component	Number fraction	Ext. Coeff. [[km^{-1}]/[part. cm^{-3}]]	Ångström coefficient	Single scattering albedo	Asymmetry parameter
Average continental					
Water insoluble	$2.61 \cdot 10^{-5}$	$8.62 \cdot 10^{-3}$	-0.081	0.750	0.811
Water soluble	0.458	$7.71 \cdot 10^{-6}$	1.93	0.977	0.675
Soot	0.542	$4.48 \cdot 10^{-7}$	1.23	0.173	0.302
<i>Composite</i>	<i>1.0</i>	<i>$4.00 \cdot 10^{-5}$</i>	<i>1.59</i>	<i>0.899</i>	<i>0.678</i>
Tropical marine					
Water soluble	0.983	$8.62 \cdot 10^{-6}$	1.93	0.977	0.675
Sea salt (acc. mode)	0.017	$3.83 \cdot 10^{-3}$	-0.11	1.00	0.781
Sea salt (coarse mode)	$2.17 \cdot 10^{-6}$	0.220	-0.054	1.00	0.848
<i>Composite</i>	<i>1.0</i>	<i>$7.32 \cdot 10^{-5}$</i>	<i>0.20</i>	<i>0.998</i>	<i>0.711</i>

supposed to be composed of water soluble and sea salt aerosols. For the polluted atmosphere of the northern hemisphere, the *average continental* aerosol, composed of water soluble and insoluble species as well as soot, was considered. Both in chemical composition and its optical properties, the average continental aerosol model is consistent with the findings of in-situ observations of polluted air during INDOEX.

Once the aerosol composition, size distribution, and the chemical properties of each component are established, the optical properties of the aerosol mixture can be obtained by performing Mie calculations for each component and integrating over the size range. The Mie calculations were performed using a numerical code based on Bohren and Huffmann (1983). The resulting optical parameters for the aerosol models used for the MOCARAT calculations are listed in 3.2. Because of the high soot content, the average continental aerosol has significant absorption, which leads to a single scattering albedo of 0.90 at $\lambda_{ref} = 0.65 \mu\text{m}$. Figure 3.1 shows the spectral dependence of the extinction of the aerosol models and its components. Even though its number fraction is only 1.7 %, the sea salt component contributes the most part of the extinction of the marine aerosol, particularly in the near IR. The large effective size of the sea salt aerosol also causes the total extinction of the marine aerosol to decrease much more slowly with increasing wavelength than the average continental. Whereas the ratio between the $1.64 \mu\text{m}$ and the $0.65 \mu\text{m}$ aerosol extinction is 0.82 for the tropical marine aerosol, the ratio is 0.23 for the tropical marine aerosol extinction at the same wavelengths.

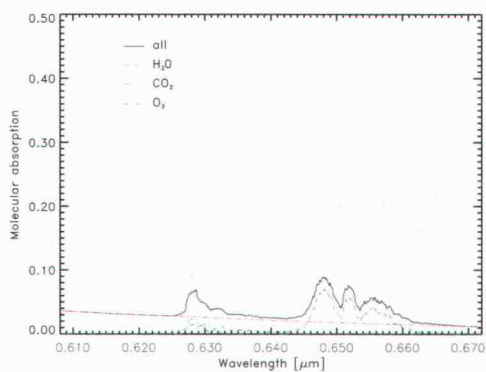
3.4 The Multichannel Cloud Radiometer (MCR)

The MCR is a 7-channel scanning radiometer that was designed for operation on aircraft. It was originally developed at the NASA Goddard Space Flight Center in the late 1970s and operated on several research flights. After having been taken out of service at NASA, it was transferred to the National Center of Atmospheric Research NCAR and employed on several field experiments on NCAR research aircraft. During INDOEX, the MCR was flown on the NCAR C-130 for ultra high resolution remote sensing of aerosol and clouds. Before the INDOEX campaign, it was totally redesigned and modified for improved performance and data sampling rate. In fact, the remodeling was finished just prior to INDOEX and the MCR arrived in the field with little prior testing. In order to increase sensitivity in some channels and avoid saturation in other channels, the instrument gains had to be adjusted during the first couple of INDOEX research flights. In addition, the instrument is sensitive to the conditions at flight altitude, making necessary the in-flight calibration for the MCR data collected during INDOEX.

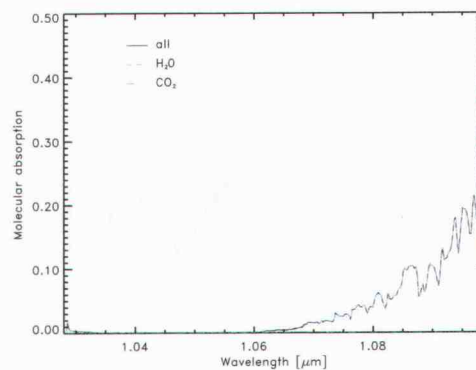
The MCR was designed for the observation of cloud and aerosol physical properties. It has six channels in the solar spectrum and one channel in the thermal infrared (Table 3.3). Channels 1, 4, 5 and 6 are chosen to be located in spectral window regions with low molecular absorption (Figure 3.2).

In channel 1 there is only weak water vapor and very little CO₂ absorption in addition to the flank of the ozone Chappius band. The shortwave part of channel 4 is virtually free of molecular absorption. In its longwave end, however, it runs into significant water vapor absorption. Channel 5 has very little absorption by CO₂ and water vapor. In the spectral domain of channel 6 there

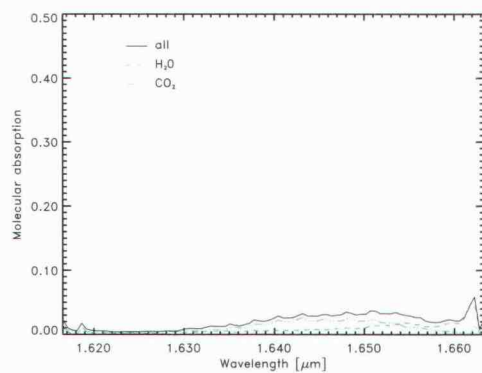
FIGURE 3.2: Atmospheric absorption for a vertical path in the wavelength ranges for MCR channels 1, 4, 5 and 6.



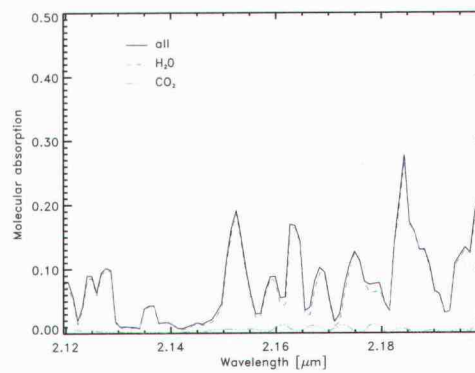
(a) Channel 1



(b) Channel 4



(c) Channel 5



(d) Channel 6

is moderate water vapor absorption and low absorption by CO₂. Due to the high transmission, these channels are well suited for the retrieval of aerosol and cloud parameters such as optical thickness, effective droplet radius, and column liquid water amount.

Channels 2 and 3 are very narrow at the wavelengths of the oxygen A-band. Due to the moderate absorption in these spectral bands, for cloudy sky conditions the photons do not penetrate very deep into the cloud interior and most of the upwelling photons are reflected at the cloud top. The observed reflectance is therefore very sensitive to cloud top altitude and can be used for its retrieval.

Channel 7 in the far IR can be used to retrieve cloud top temperature from Planck's law. Unfortunately, during the INDOEX campaign channel 7 rarely worked and when it did, the signal was degraded by large instrument noise probably induced by mechanical vibrations. For this thesis, the model developed focused on solar radiation and therefore channel 7 was not included in the analysis.

The MCR has a mirror that rotates at a rate of 3.47 rev/s and scans in the plane perpendicular to the direction of the aircraft's travel. It is oriented down looking with a scanning range that covers $\pm 45^\circ$ from nadir. During INDOEX, it was operated at typical altitudes of some 5000 to 6000 m. With the sampling rate of 360 pixels per active scan and a very narrow field of view of 0.007 radians, the spatial resolution in the nadir direction is 30 to 40 m.

From the scanning mirror, the light is reflected to a mirror telescope system in order to generate a parallel beam. The optical detection unit employs a series of dichroic filters to separate the beam for the various spectral regions. Dichroic filters are characterized by high reflectivity for sufficiently short wavelengths,

TABLE 3.3: The channel configuration of the MCR as operated during the INDOEX campaign

	Central wave- length [μm]	Bandwidth FWHM [μm]
Channel 1	0.640	0.063
Channel 2	0.761	0.001
Channel 3	0.763	0.001
Channel 4	1.06	0.07
Channel 5	1.64	0.05
Channel 6	2.16	0.08
Channel 7	10.9	0.9

whereas for longer wavelengths the transmissivity is high. The broad wavelength intervals defined by transmission through each of these dichroic filters are further constrained by transmission through narrow band interference filters before detection in photomultiplier units.

There is no transmitting window material that works for all the wavelength channels. Radiometers such as the MCR are therefore open and are fully exposed to the harsh environment at flight altitude during field experiments. The dichroic elements of the instrument as well as the band filters are sensitive to temperature. Despite temperature stabilization by heaters, the calibration at flight is likely to differ from the calibrations in the laboratory performed after the field campaign. Therefore it is necessary to check the in-flight performance of the instrument.

CHAPTER 4

MOCARAT: A MONTE CARLO RADIATIVE TRANSFER MODEL

The equation of radiative transfer in a scattering atmosphere (2.32) is an integro-differential equation and has no analytical solution. However, there are a variety of different approaches for numerical solutions.

The MONte CARlo RAdiative Transfer Model MOCARAT was developed in the scope of this thesis for the accurate modeling of the radiance field in a plane-parallel, i.e. horizontally uniform atmosphere over a reflecting ocean surface. In a more formal language, this translates to the task of solving the equation of radiative transfer for a non-isotropic boundary condition. The goal is to simulate the observed band radiances measured by multispectral imaging radiometers such as the MCR (see Section 3.4), the Moderate Resolution Imaging Spectrometer (MODIS) or the Advanced Very High Resolution Radiometer (AVHRR) and investigating the sun glint pattern. Additional complication arises due to the non-gray absorptivity over the bandwidths of the various channels.

Most commonly used radiative transfer models other than Monte Carlo take advantage of the linearity of the equation of radiative transfer and perform a separation of variables in the radiance field by decomposing its azimuthal dependence in a Fourier series. Each Fourier component is then considered at a discrete number of μ values (Thomas and Stamnes, 1999, ch. 8). Prominent examples are given by the discrete ordinate method and the adding-doubling

method.

Briefly, the discrete ordinate method explicitly solves the equation of radiative transfer by approximating the scattering source term as a discretized radiance field using a standard numerical quadrature rule. The whole problem can then be stated as a high order system of linear algebraic equations in the radiance components (Stamnes and Swanson, 1981; Stamnes and Dale, 1981). This method is implemented in the discrete ordinate radiative transfer model DISORT (Stamnes et al., 1988), which is a widely used tool for radiative transfer calculations.

For an optically thin layer, the reflection and transmission properties of each Fourier component can be readily approximated by single scattering. Once the optical properties of the sub-layers are determined, the adding-doubling method uses a standard formula, the doubling rule, to obtain the reflection and transmission of a homogeneous layer of finite thickness. The adding rule is used to combine homogeneous layers with distinctly different radiative properties. Repeated application of this method makes it possible to calculate the optical properties of an atmosphere of arbitrary vertical structure. A nice example of an implementation of the adding-doubling method is given by the POLRADTRAN model (Evans and Stephens, 1991).

Monte Carlo radiative transfer algorithms solve problems by describing a system in terms of elementary statistical processes and studying its behavior in the limit of a large number of samples. On the level of individual photons, radiative transfer is governed by statistical processes, such as the interaction with the atmosphere's molecules and aerosols, and can therefore be readily simulated using Monte Carlo techniques. The examples of Monte Carlo applications in atmospheric radiation are diverse in both their algorithmic approach, the given

boundary conditions and the the nature of the physical quantity to be obtained. Some codes obtain radiances by solving the equation of transfer in its integral form using a Monte Carlo Algorithm (Marchuk et al., 1980, ch. 3). Others stick closely with the actual physical processes by sampling the paths of individual photons. The straightforward implementation of the physics governing the radiative transfer is attractive because of its conceptual simplicity and flexibility. Non-gray absorption can be included at almost no additional computational cost. It is also feasible to simulate horizontally non-uniform atmospheres, e.g. in order to explore three dimensional cloud fields. Another very important reason for using the Monte Carlo technique for this study is that it facilitates the non-isotropic boundary condition imposed by the reflecting ocean surface.

4.1 Algorithmic Realization

In order to account for changes in atmospheric composition, pressure and temperature, the atmosphere is subdivided into a finite number of computational layers. Since the molecular absorption varies strongly with pressure and temperature, the atmosphere is discretized into 1 km layers for the transmission calculations. For clear sky conditions, it is sufficient to deal with as little as three scattering layers: a boundary layer that is well mixed and characterized by a high aerosol load, the upper troposphere, ranging from 1 to some 10 km, where both aerosol concentration and water vapor mixing ratio are decreased, and a top layer, reaching from the tropopause to the top of the atmosphere, where the humidity is very small and the aerosol concentration is assumed to be zero.

4.1.1 Sampling of Photon Paths

Individual photons are described by their altitude in units of optical depth, the optical thickness of the path traveled, and the direction of propagation. In a first step, the photon's path through the atmosphere is simulated by taking into account only scattering and reflection at the lower boundary, i.e. without consideration of absorption. In a second step, whenever the photon crosses the altitude of the observer, the transmissivity T_m of the particular path is determined as a function of the pathlength and the number of scatterings within each layer.

The reflectance, as defined by eq. (2.5), can be expressed in terms of the incident solar energy and the energy as measured at the observer level:

$$R(\vartheta, \varphi) = \frac{\pi}{\mu_0} \frac{dE_{obs}}{dA_{\perp} d\Omega dt} \cdot \left(\frac{dE_{inc}}{dA dt} \right)^{-1} \quad (4.1)$$

At a given bin ($\mu_i = \cos \vartheta_i, \varphi_j$), the results of the Monte Carlo simulation are evaluated by approximating the ratio of energies per unit time and area by

$$\frac{dE_{obs}}{dA_{\perp} dt} \cdot \left(\frac{dE_{inc}}{dA dt} \right)^{-1} \approx \frac{\sum_{m=1} T_m \mu_m}{\mu_0 N_{tot}} \quad (4.2)$$

where the sum is performed over all photons recorded at the solid angle bin (μ_i, φ_i), N_{tot} is the total number of photons used for the simulation, and μ_m is the cosine of the photon's zenith angle. The somewhat counterintuitive factor of $\mu_m = \cos \vartheta_m$ accounts for the fact that for the radiance, the differential area perpendicular to the beam must be evaluated, which is given by $dA_{\perp} = \cos \vartheta_m dA$, i.e. an observer looking along a slant path is covering more reflecting surface area per unit solid angle than one looking at nadir. Additionally replacing the differential $d\Omega$ by the bin size $\Delta\Omega_{i,j} = \Delta\mu_i \Delta\varphi_j$ gives the modeled radiance

$$R_{MC}(\mu_i, \varphi_j) = \frac{\pi}{\mu_0 N_{tot} \Delta\mu_i \Delta\varphi_j} \sum_{m=1} T_m \mu_m. \quad (4.3)$$

4.1.2 Generation of Random Variables

Commonly used random number algorithms typically generate random deviates with a uniform probability distribution in the 0 to 1 range. Photon free path lengths as well as scattering angles and the direction of light reflected at the lower boundary are random variables that are, in general, not uniformly distributed. In order to generate random variables x with an arbitrary, normalized distribution function $p_x(x)$ from a uniform deviate y a transformation function $x(y)$ is needed such that

$$p_x(x(y))dx = p_y(y)dy = dy \quad (4.4)$$

where $p_y(y) = 1$ for the uniform probability density function in the interval from 0 to 1. Integration of both sides yields

$$F_x(x(y)) \equiv \int_{x_0}^{x(y)} p_x(x') dx' = \int_{y_0=0}^y dy' = y. \quad (4.5)$$

where F_x is the cumulative distribution of the random variable x and the cumulative distribution of the random variable y is identity. Hence, the uniform deviate y can be transformed by means of the inverse of the cumulative distribution function:

$$x(y) = F_x^{-1}(y). \quad (4.6)$$

Typically 10^7 samples were used for the simulations conducted in this study, which requires approximately 10^8 random numbers. To ensure a sufficient number of independent and uncorrelated random numbers, the algorithm *RAN2* from the *Numerical Recipes* (Press et al., 1980, ch. 7.1.) was chosen.

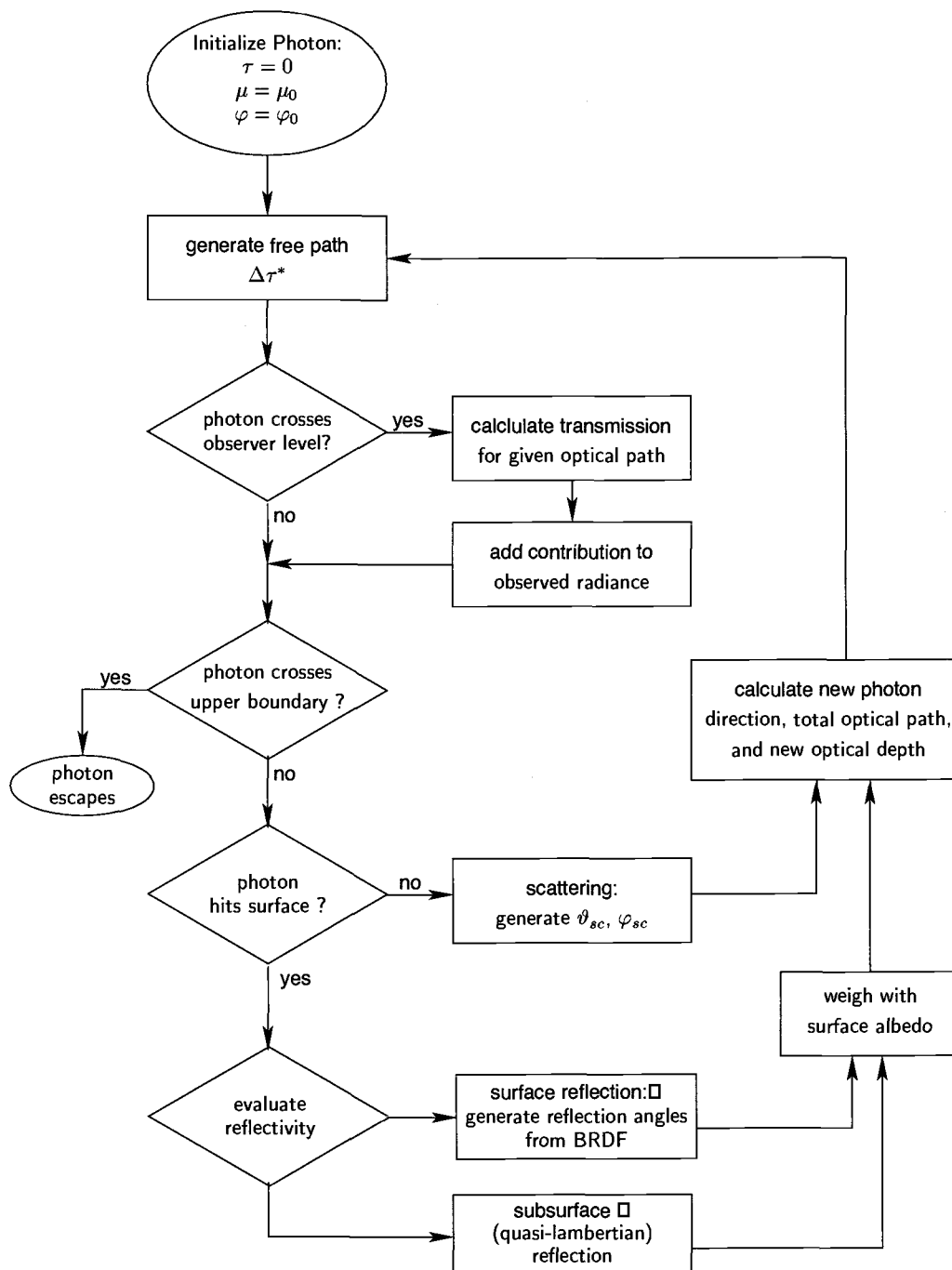


FIGURE 4.1: Simplified flowchart of a photon's random trial through the model atmosphere.

4.2 Simulation of Scattering

As visualized in Figure 4.1, forward tracing is performed by injecting photons incident at the top of the atmosphere in the direction of insolation and generating a trial of free path propagation and scattering.

The incremental optical pathlength $\Delta\tau^*$ is exponentially distributed:

$$p(\Delta\tau^*) = e^{-\Delta\tau^*} \quad (4.7)$$

By straight forward application of the transformation equation (4.6) we get $\Delta\tau^* = -\ln(1-y)$. As the uniform deviate y has the same probability distribution as $1-y$, random incremental optical pathlengths can be generated using the simplified form

$$\Delta\tau^* = -\ln y. \quad (4.8)$$

Given $\Delta\tau^*$, the new optical depth can be readily determined

$$\tau_{new} = \tau_{old} - \mu \Delta\tau^*, \quad (4.9)$$

where the negative sign arises due to the convention that downwelling photons are assigned a negative value for μ . Unless the photon escapes from the atmosphere ($\tau < 0$) or interacts with the surface ($\tau > \tau_{sfc}$), scattering occurs.

For each layer and wavelength channel, the Rayleigh scattering optical depth τ_R can be calculated from the layer's pressure thickness using the bulk formula (2.13) for the scattering cross section:

$$\tau_R = - \int_{z_1}^{z_2} n \sigma_R dz = \int_{p_1}^{p_2} \frac{\sigma_R}{M g} dp, \quad (4.10)$$

where M is the mean mass of the atmosphere's molecules.

Mie scattering cross sections are calculated for the different species considering typical size distributions using a generic Mie code. In order to obtain the layers' total scattering optical depth τ_l , the linearity of eq. (2.6) can be taken advantage of, which implies that the total optical depth is given by the sum of optical depths of the the individual species:

$$\tau_l = \tau_R + \sum_i \tau_i \quad (4.11)$$

where the index i denotes the various aerosol species. Likewise, the total single scattering albedo is given by the sum of single scattering albedo weighed by the optical depths. Noting that Rayleigh scattering is conservative, i.e. $\omega_R = 1$, the layer single scattering albedo is given by

$$\omega_l = \frac{1}{\tau_l} \left(\tau_R + \sum_i \tau_i \omega_i \right). \quad (4.12)$$

The scattering phase function is obtained as a linear combination of the phase functions weighed proportional to the scattering extinction:

$$P_l(\mu) = \frac{1}{\omega_l \tau_l} \left(\tau_R P_R(\mu) + \sum_i \omega_i \tau_i P_i(\mu) \right), \quad (4.13)$$

where the sum is performed over the different Mie scattering species. For the transformation of the computer generated uniform random variable y to the corresponding value for the scattering angle's cosine μ_{sc} , according to (4.6) it is necessary to evaluate the inverse of cumulative phase function:

$$\mu_{sc} = \omega_l \tau_l \left(\tau_R F_R + \sum_i \omega_i \tau_i F_i \right)^{-1} (y). \quad (4.14)$$

The normalized Rayleigh cumulative phase function corresponding to the modified phase function (2.15) is then given by

$$F_R(\mu) = \frac{1}{2} \int_{-1}^{\mu} P_R(\mu') d\mu' = \frac{1}{2} + \frac{3}{8}\mu + \frac{1}{8}\mu^3. \quad (4.15)$$

If the Henyey-Greenstein phase function is used to parametrize Mie scattering, the normalized cumulative phase function can be expressed as

$$F_{HG}(\mu) = \frac{1}{2} \int_{-1}^{\mu} P_{HG}(\mu') d\mu = \frac{1-g^2}{2g} \left(\frac{1}{\sqrt{1+g^2-2g\mu}} - \frac{1}{1+g} \right). \quad (4.16)$$

MOCARAT also allows for usage of exact numerical Mie data from a generic Mie code. For most of the simulations presented in this study, this option was used in order to obtain a more accurate representation of the scattering by aerosol. The Mie calculations were performed using the algorithm proposed by Bohren and Huffmann (1983, app. A).

Rather than evaluating (4.14) for each of the scattering events, it is computationally much more efficient to calculate a lookup table prior to the actual photon simulation runs; For a sufficiently large number of uniformly spaced values of the computer generated random variable y the corresponding value for the scattering angle's cosine $\mu_{sc}(y)$ is calculated by performing the inversion in (4.14) numerically. Whereas the phase function is given with typically 1800 values, the lookup table of the inverse distribution is calculated for 20000 values of the random deviate y in order to accurately capture the forward peak of the Mie scattering. For each scattering event, a scattering angle is quickly determined reading the μ_{sc} value from the location in the lookup array corresponding to a given random number y . The computational effort for the lookup table is small compared to the that of the photon sampling.

As the phase functions considered in this study do not depend on the azimuthal scattering angle, φ_{sc} is uniformly distributed and obtained by

$$\varphi_{sc} = 2\pi y. \quad (4.17)$$

Once the scattering angles $\vartheta_{sc}, \varphi_{sc}$ are generated, the new photon angles ϑ', φ' must be computed from the incident angles ϑ, φ .

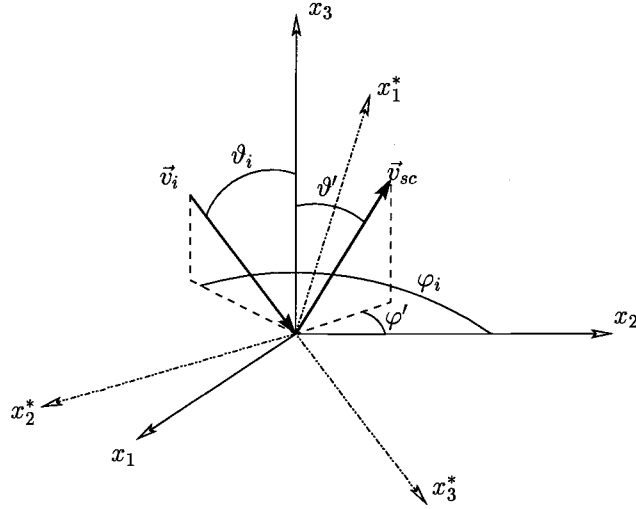


FIGURE 4.2: A new coordinate frame S^* aligned with the photon incident under \vec{v} with angles ϑ , φ is introduced in order to derive the new direction of propagation \vec{v}' with angles ϑ' , φ'

In order to derive the new scattering angles, consider the fixed coordinate system S with the x_1 - x_2 -plane parallel to the ground and the x_3 axis in the vertical, in which the direction of the incident photon is given by

$$\vec{v} = \begin{pmatrix} \cos \varphi \sin \vartheta \\ \sin \varphi \sin \vartheta \\ \cos \vartheta \end{pmatrix}. \quad (4.18)$$

In addition, we shall introduce a coordinate system S^* with the x_3^* -axis pointing in the direction of the incident photon and additionally constrained by the condition that the x_2^* be parallel to the ground. Its orthonormal unit vectors in

S are

$$\hat{e}_1^* = \begin{pmatrix} \cos \varphi \cos \vartheta \\ \sin \varphi \cos \vartheta \\ -\sin \vartheta \end{pmatrix}, \quad \hat{e}_2^* = \begin{pmatrix} -\sin \varphi \\ \cos \varphi \\ 0 \end{pmatrix}, \quad \hat{e}_3^* = \begin{pmatrix} \cos \varphi \sin \vartheta \\ \sin \varphi \cos \vartheta \\ \cos \vartheta \end{pmatrix}. \quad (4.19)$$

Hence, vectors are transformed from the system S to S* by means of the matrix

$$\mathbf{T} = \begin{pmatrix} \cos \varphi \cos \vartheta & -\sin \varphi & \cos \varphi \sin \vartheta \\ \sin \varphi \cos \vartheta & \cos \varphi & \sin \varphi \cos \vartheta \\ -\sin \vartheta & 0 & \cos \vartheta \end{pmatrix}. \quad (4.20)$$

The direction of the scattered photon in S* is given by

$$\vec{v}_{sc}^* = \begin{pmatrix} \cos \varphi_{sc} \sin \vartheta_{sc} \\ \sin \varphi_{sc} \sin \vartheta_{sc} \\ \cos \vartheta_{sc} \end{pmatrix}. \quad (4.21)$$

In order to obtain its value in S, we have to apply the transformation function

T:

$$\begin{aligned} \vec{v}_{sc} &\equiv \begin{pmatrix} \cos \varphi' \sin \vartheta' \\ \sin \varphi' \sin \vartheta' \\ \cos \vartheta' \end{pmatrix} = \mathbf{T} \vec{v}_{sc}^* \\ &= \begin{pmatrix} \cos \varphi \cos \vartheta \cos \varphi_{sc} \sin \vartheta_{sc} - \sin \varphi \sin \varphi_{sc} \sin \vartheta_{sc} + \cos \varphi \sin \vartheta \cos \vartheta_{sc} \\ \sin \varphi \cos \vartheta \cos \varphi_{sc} \sin \vartheta_{sc} + \cos \varphi \sin \varphi_{sc} \sin \vartheta_{sc} + \sin \varphi \sin \vartheta \cos \vartheta_{sc} \\ -\sin \varphi \cos \varphi \sin \vartheta_{sc} + \cos \vartheta \cos \vartheta_{sc} \end{pmatrix} \end{aligned} \quad (4.22)$$

The sought angles ϑ' , φ' can be obtained from the x_3 and the ratio of the x_2 and x_1 vector components, respectively:

$$\cos \vartheta' = \cos \vartheta \cos \vartheta_{sc} - \sin \varphi \cos \varphi \sin \vartheta_{sc} \quad (4.23)$$

$$\tan \varphi' = \frac{\sin \varphi \cos \vartheta \cos \varphi_{sc} \sin \vartheta_{sc} + \cos \varphi \sin \varphi_{sc} \sin \vartheta_{sc} + \sin \varphi \sin \vartheta \cos \vartheta_{sc}}{\cos \varphi \cos \vartheta \cos \varphi_{sc} \sin \vartheta_{sc} - \sin \varphi \sin \varphi_{sc} \sin \vartheta_{sc} + \cos \varphi \sin \vartheta \cos \vartheta_{sc}} \quad (4.24)$$

4.3 Simulation of Absorption

The MCR channels are sensitive to radiation in spectral intervals with width of as much as 1700 cm^{-1} . The spectral widths are large compared with absorption structures typically narrower than 1 cm^{-1} . The Rayleigh and aerosol scattering cross sections, in contrast, vary more smoothly with wavenumber. In order to model the band radiances, the absorption coefficients for each gaseous species cannot be assumed to be constant with wavenumber. Performing model runs for each of the spectral lines would result in a gigantic computational effort. There are two absorption schemes available in MOCARAT that are much more efficient than line by line calculations. The first scheme involves pre-calculation of a lookup table for photon transmission as a function of the scattering optical pathlength in each layer. This method saves CPU-time, however it is very memory expensive and therefore cannot be used with a large number of scattering layers. The second scheme is the correlated k -distribution method, which is based on approximating the wavelength dependence of the molecular absorption by a small number of representative absorption coefficients. The correlated k -method is inexpensive in terms of memory, saves considerable CPU time compared to line-by-line calculations, and is reasonably accurate.

4.3.1 The Lookup-Table Scheme

For a given atmospheric profile and composition, rather than performing computations of the band transmissivity for every sampled photon, it is much more efficient to pre-calculate the transmission for a number of different atmospheric paths and approximate the actual transmission by linear interpolation.

To do so, a distinction is made between arbitrary optical paths, characterized

by their scattering pathlengths τ^* , and the vertical scattering optical depths τ of atmospheric layers.

The effective transmission in a spectral band $\Delta\nu$ for a scattering optical pathlength τ^* is given by

$$T(\tau^*) = \frac{1}{\Delta\nu} \int_{\Delta\nu} T_\nu(\tau^*) d\nu, \quad (4.25)$$

where the T_ν is the monochromatic spectral transmission as a function of optical path. For a given composition, pressure and temperature profile, the transmission \hat{T}_i for vertical paths can be obtained at different wavenumbers ν_i from the *MODTRAN* database (Kneizys et al., 1996) with a resolution of 2 cm^{-1} .

\hat{T}_i can be readily converted into spectral absorption optical depth τ_i^a by applying

$$\tau_i^a = -\ln \hat{T}_i. \quad (4.26)$$

For monochromatic radiation, the absorption along an arbitrary scattering path in a homogenous atmosphere is augmented by the factor τ^*/τ . Similarly, since the spectral resolution of the *MODTRAN* data is sufficiently high, for each of the intervals and for an arbitrary scattering path of optical thickness τ^* with s scattering events in a layer of scattering optical thickness τ , the transmission can be approximated by

$$\hat{T}_i(\tau^*, s) = e^{\frac{\tau^*}{\tau} \ln \hat{T}_i} \omega^s, \quad (4.27)$$

where the factor ω^s accounts for absorption by the scattering particles. Discretization of the integral in eq. (4.25) yields for the broadband transmission

$$T(\tau^*, s) \approx \frac{1}{\Delta\nu} \sum_i e^{\frac{\tau^*}{\tau} \ln \hat{T}_i} \omega^s \delta\nu_i. \quad (4.28)$$

Generalization for the case of a model atmosphere discretized into N_l different layers gives the total transmission

$$T_{tot}(\tau_1^*, \dots, \tau_{N_l}^*; s_1, \dots, s_{N_l}) \approx \frac{1}{\Delta\nu} \sum_i \delta\nu_i \prod_l e^{\frac{\tau_l^*}{\tau} \ln \hat{T}_l \omega_l^{s_l}}, \quad (4.29)$$

where the index l refers to scattering optical path, scattering optical depth, vertical path transmissivity, number of scatterings and the single scattering albedo in the l th layer, respectively.

4.3.2 The Method of Correlated k -Distributions

A common scheme for accounting for non-gray absorption is the method of correlated k -distributions. It is used for both the computation of heating rates, e.g. in general circulation models (GCMs), and transmission calculations in the spectral ranges of imaging radiometers (Lacis and Oinas, 1991; Kratz, 1995).

For the sake of consistency with the literature, the transmission function T shall be formulated in terms of column absorber amounts $u = \int \rho(z) dz$ and the absorption coefficient per column absorber amount k , given in units of $(\text{g/cm}^2)^{-1}$. For a homogeneous path and a spectral interval $\Delta\nu$, T is given by

$$T_{\Delta\nu}(u) = \frac{1}{\Delta\nu} \int_{\Delta\nu} e^{-k(\nu)u} d\nu. \quad (4.30)$$

Consider the probability density distribution of the k -values in the spectral interval:

$$h(k) = \frac{1}{\Delta\nu} \frac{\delta\nu(k)}{dk}, \quad (4.31)$$

where $\delta\nu(k)$ is the combined length of the wavelength subintervals for which the absorption coefficient is in the interval between k and $k + dk$. It is possible to

reformulate the transmission (4.30) by substitution for $h(k)$:

$$T_{\Delta\nu}(u) = \int_0^{\infty} e^{-ku} h(k) dk \quad (4.32)$$

Given the probability density, the cumulative probability is obtained as

$$g(k) = \int_0^k h(k') dk'. \quad (4.33)$$

Let $k_g(g) = g^{-1}(k)$ be its inverse. The transmission function (4.32) can then be rewritten in the simplified form

$$T_{\Delta\nu}(u) = \int_0^1 e^{-k_g(g)u} dg. \quad (4.34)$$

In this form, the calculation can be greatly simplified by approximating the function k_g by a step function. This is accomplished by subdividing g -space into a small number of intervals $[g_i, g_{i+1})$ and assuming a constant absorption coefficient k_i in each interval, thus converting (4.34) into a sum over a small number of k -values k_i , each of which is assigned a weight $\Delta g_i = g_{i+1} - g_i$:

$$T_{\Delta\nu}(u) \approx \sum_i \Delta g_i e^{-k_i u}. \quad (4.35)$$

The realistic atmosphere is vertically inhomogeneous in pressure and temperature. Due to pressure and temperature broadening (Section 2.3), $k_i = k_i(T, p)$. It is empirically confirmed that, despite the pressure and temperature dependence, the location in g -space of the k -values corresponding to the same wavelength subintervals is highly correlated for different values of T, p (Lacis and Oinas, 1991). This means that the order of the k -values in each differential wavenumber bin ν remains approximately constant. The observed correlation is due to the line structure of the absorption spectrum: strong lines remain

stronger than the weaker lines even after broadening. For transmission calculations of inhomogeneous paths, the correlated k -distribution method takes advantage of this correlation. Since wavenumber subintervals $\delta\nu$ tend to remain in the same interval Δ_g independent of pressure and temperature, the transmission of an inhomogeneous path can be computed by keeping the Δg_i fixed while adjusting the k -values k_i to account for the change of atmospheric conditions:

$$\begin{aligned} T_{\Delta\nu}(u) &\approx \sum_i \Delta g_i \exp\left(-\int_0^u k_i(T, p) du'\right) \\ &\approx \sum_i \Delta g_i \exp\left(-\sum_j^N k_i(T_j, p_j) \Delta u_j\right) \end{aligned} \quad (4.36)$$

where the latter expression corresponds to an atmosphere discretized into N vertical layers with temperatures, pressures and slant column densities T_j , p_j and Δu_j .

The task of obtaining appropriate values of g_i , k_i is accomplished by fitting them to a transmission function from line-by-line calculations. However, since exponential sum fitting is a classical example of a numerically ill-conditioned problem, it is not trivial to obtain an optimal set of parameters g_i , k_i for a given range of absorber abundances. A well optimized routine was proposed by Wiscombe and Evans (1977) and implemented by Kratz (1995). Explicit k -calculations were not performed as part of this study, however for a variety of imaging radiometers such as AVHRR, MODIS, VIRS etc., k -values were obtained from Kratz (private communication). They are also available for download ¹.

¹ <http://asd-www.larc.nasa.gov/kratz>

4.4 Reflecting Ocean Surface

4.4.1 Quasi-Lambertian Subsurface Reflection

An explicit integration of the ocean interior into the radiative transfer model would greatly increase the computational effort. Since the upwelling radiation from the ocean accounts for only a small fraction of the atmospheric radiation, it is possible to greatly simplify the computations by accounting for it as a quasi-Lambertian contribution to the reflectance. The quasi-Lambertian albedo is obtained from the Eddington approximation.

The Eddington approximation is a simple yet accurate way of estimating flux transmissivity and reflectivity of a scattering and absorbing slab (e.g. Thomas and Stamnes, 1999). It relies on a low order representation of upwelling and downwelling radiance for the evaluation of the equation of radiative transfer in order to obtain the reflected and transmitted fluxes.

Due to its high absorption coefficient, the ocean can readily be considered as a semi-infinite layer. In this case, the Eddington reflectance is given by

$$R = \frac{\sqrt{1 - \omega g} - \sqrt{1 - \omega}}{\sqrt{1 - \omega g} + \sqrt{1 - \omega}}. \quad (4.37)$$

Since the asymmetry parameter for Rayleigh scattering is zero, the effective scattering asymmetry parameter g is calculated from the biogenic hydrosol's value as

$$g = \frac{b_{bio} g_{bio}}{b_w + b_{bio}}, \quad (4.38)$$

where b_w , b_{bio} are the scattering extinction coefficients for Rayleigh and Mie scattering. Similarly, the effective scattering albedo ω is given as the ratio between the conservative scattering and the extinction

$$\omega = \frac{b_w + b_{bio}}{a_w + a_{bio} + b_w + b_{bio}}, \quad (4.39)$$

where a_w , a_{bio} are the coefficient associated with molecular absorption, and the hydrosol absorption. A certain ratio of the upwelling photons are not transmitted across the ocean-atmosphere interface, which is accounted for by introducing a fudge factor f . The quasi-Lambertian Albedo α_L is given by

$$\alpha_L = fR = f \frac{\sqrt{1-\omega g} - \sqrt{1-\omega}}{\sqrt{1-\omega g} + \sqrt{1-\omega}} \quad (4.40)$$

Due to the small values for R , the contribution from multiple reflection at the interface is negligible. Hence, f can be approximated by integration of the Fresnel reflectance over the hemisphere and is found to be about 0.5 at 700 nm. The quasi-Lambertian albedo was calculated using typical values for the hydrosol listed in Table 4.1 (Walker, 1994).

Note that α_L depends critically on the biogenic scattering coefficient b_{bio} and asymmetry parameter g_{bio} . Their reported values from field experiments, however, vary significantly. The albedo values calculated for the visible wavelength suggest that the contribution of the subsurface radiation to the upwelling radiance at the surface can be significant, particularly away from the sun glint where the radiance field is rather dark. Due to the increase of water absorptance, subsurface reflectance becomes negligible in the near infrared.

4.4.2 Simulation of Photon Reflection from the Ocean

The bidirectional reflection function of the sea surface can be expressed as a function of the cosine of the incident beam's zenith angle, $\mu = \cos \vartheta$, that of the reflected beam, $\mu' = \cos \vartheta'$, and the relative azimuth angle, φ_{rel} :

$$P = P(\mu', \varphi_{rel}; \mu). \quad (4.41)$$

TABLE 4.1: Parameter values relevant for the calculation of the quasi-Lambertian subsurface albedo α_L for different wavelengths. Coefficients of scattering and absorption in the ocean by molecules and hydrosols as well as the hydrosol asymmetry parameter. Parameter values adapted from Walker (1994).

λ [μm]	b_w [m^{-1}]	b_{bio} [m^{-1}]	a_w [m^{-1}]	a_{bio} [m^{-1}]	g_{bio}	ω	α_L
0.50	$2.9 \cdot 10^{-3}$	0.14	0.026	0.10	0.96	0.53	$8.2 \cdot 10^{-3}$
0.64	$1.0 \cdot 10^{-3}$	0.10	0.329	0.02	0.96	0.22	$1.8 \cdot 10^{-3}$
0.76	$0.5 \cdot 10^{-3}$	0.08	2.55	0.01	0.96	0.030	$1.8 \cdot 10^{-4}$
>0.80	$< 0.4 \cdot 10^{-3}$	< 0.08	> 2.00	~ 0.001	> 0.94	< 0.039	$< 3.2 \cdot 10^{-4}$

Lookup tables are generated for a set of incident zenith angles. For clear sky conditions, most of the photons reach the sea surface without being scattered. Therefore, best performance is achieved if the lookup table for the direct beam incident at the solar zenith angle μ_0 is generated with higher resolution than the lookup tables computed for other incident zenith angles in order to account for reflection of diffuse light.

The probability that, for a given incident zenith angle μ_i the photon is reflected into the zenith angle bin $[\mu'_j; \mu'_j + \Delta\mu_j]$ can be approximated by discretizing using the bidirectional reflection function P :

$$\begin{aligned} p_\mu(\mu'_j + \frac{\Delta\mu_j}{2}) \Delta\mu_j &\approx \Delta\mu_j \int_{2\pi} P\left(\mu'_j + \frac{\Delta\mu_j}{2}, \varphi_{rel}; \mu\right) d\varphi_{rel} \\ &\approx \Delta\mu_j \sum_{i=0}^{N_\varphi-1} P\left(\mu, \mu'_j + \frac{\Delta\mu_j}{2}, \varphi_i + \frac{\Delta\varphi_i}{2}; \mu\right) \Delta\varphi_i \end{aligned} \quad (4.42)$$

where there are N_{phi} azimuthal bins $[\varphi_j; \varphi_j + \Delta\varphi_j]$. The cumulative probability $F_{\mu'_j}$ is then given by the sum over the probabilities for the bins with lower μ' :

$$F_{\mu'_j}(\mu') = \sum_{\mu'_k < \mu'_j} p_\mu(\mu'_k) \Delta\mu_k. \quad (4.43)$$

$F_\mu(1)$ is equal to the flux albedo R_μ for light incident at zenith angle μ . Whenever a photon hits the surface, its weight is multiplied by R_μ . In order to obtain the zenith angle of reflection, a uniform deviate y is generated. In analogy to the application of the transformation function in the case of the scattering angle, μ' is determined by interpolating between two adjacent values μ'_j that μ'_{j+1} that are chosen such that $F_\mu(\mu'_j)/R_\mu \leq y < F_\mu(\mu'_{j+1})/R_\mu$:

$$\mu' = \mu'_j + \frac{(yR_\mu - F_\mu(\mu'_j)) \Delta\mu_j}{F_\mu(\mu'_{j+1}) - F_\mu(\mu'_j)}. \quad (4.44)$$

Likewise, in order to obtain the variable φ_{rel} , the azimuthal cumulative proba-

bility distribution G_{μ, μ'_j} for given values μ, μ'_j is defined as

$$G_{\mu, \mu'_j}(\varphi_i) = \frac{1}{C_\varphi} \sum_{\varphi_k < \varphi_i} P\left(\mu, \mu'_j + \frac{\Delta\mu_j}{2}, \varphi_i + \frac{\Delta\varphi_i}{2}\right), \quad (4.45)$$

where the normalization constant C_φ is given by

$$C_\varphi = \sum_{i=0}^{N_\varphi-1} P\left(\mu, \mu'_j + \frac{\Delta\mu_j}{2}, \varphi_i + \frac{\Delta\varphi_i}{2}\right) \Delta\varphi_i. \quad (4.46)$$

φ_{rel} is obtained from a uniform deviate y by interpolating analogously to (4.44):

$$\varphi_{rel} = \varphi_i + \frac{\left(y - G_{\mu, \mu'_j}(\varphi_i)\right) \Delta\varphi_i}{G_{\mu, \mu'_j}(\varphi_{i+1}) - G_{\mu, \mu'_j}(\varphi_i)}, \quad (4.47)$$

where i is chosen such that

$$G_{\mu, \mu'_j}(\varphi_i) \leq y < G_{\mu, \mu'_j}(\varphi_{i+1}).$$

For the simulation runs presented in this study, the lookup tables for photons incident at a particular solar zenith angle were calculated at a discretization of 128 values for both zenith and azimuthal direction of reflection. For diffuse radiation, lookup tables for 48 uniformly spaced incident angles, and a 64×64 grid for reflected zenith and azimuth directions were computed. The proposed method requires enormous amounts of memory, however it significantly reduces computational time compared to repeated evaluation of the Cox-Munk reflection function for every sampled photon.

4.5 Wavelength Dependence

Whereas molecular absorption is characterized by high variability and sharp spikes, scattering, reflection and the solar spectrum also change, however more continuously, with wavelength. For radiometer channels that are sufficiently

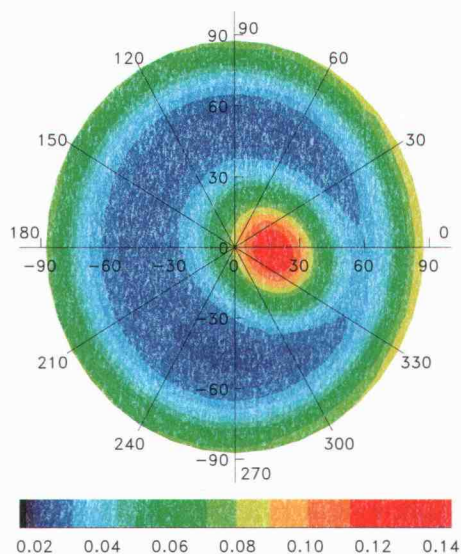
narrow, such as the channels 2 and 3 of the MCR ($\Delta\lambda=1$ nm), there is no need for corrections. By contrast, for wavelength bands such as the MCR's channel 1, the bandwidth of $0.064 \mu\text{m}$ is rather large compared to the central wavelength of $0.64 \mu\text{m}$. In this case, due to the approximate λ^{-4} dependence, the Rayleigh scattering cross section varies by some 40% across the spectral range. It is therefore useful to divide the band of such channels into a number of subchannels. Reflectance and Rayleigh scattering are then calculated for each subchannel and assumed constant across the subchannel. In order to calculate the radiance of the full channel, the subchannels are assigned a weight according to the filter response function and the associated incident insolation.

4.6 Results

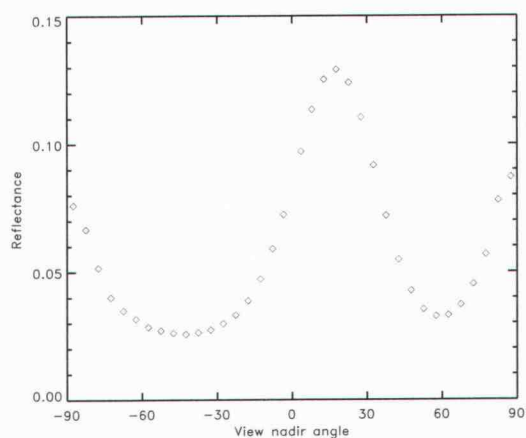
The result of a MOCARAT simulation run is visualized in Figure 4.3. In the polar plot, the reflectances are given as a function of the viewing geometry. The origin corresponds to nadir. The radial plotting direction corresponds to the view nadir angle. The azimuthal angle corresponds to the azimuthal view-solar angle, such that the solar radiation is incident from the positive x-direction. The vertical plane aligned along solar incidence is referred to as the principal plane. The simulated reflectances in the principal plane are plotted in Figure 4.3(b). The simulation was run for MCR's channel 1, assuming a solar zenith angle of 15° , tropical marine aerosol of optical depth 0.1 at the reference wavelength $\lambda_0 = 0.55 \mu\text{m}$ and a surface wind of 8 m/s blowing at an angle of 45° relative to the azimuthal angle of the incident sun.

Such small solar zenith angles are typical for the sun glint observed in the MCR data. Since the Fresnel reflectance is almost constant for small reflection

FIGURE 4.3: Example of results computed with MOCARAT. The radiance field is visualized as a polar plot (a). Principal plane reflectances are given in (b).



(a) Polar plot of reflectance



(b) Reflectances in the principal plane

angles, the sun glint is observed as an almost perfectly elliptical pattern, with the long principal axis aligned with the wind direction. Away from the sun glint, the reflectance increases with view nadir angle. This is typical for the radiance field above a surface with a low albedo, where the upwelling radiance mostly comes from atmospheric scattering. The higher the view zenith angle, the greater the optical path along which radiation is scattered into the viewing direction.

4.7 Error Estimation and Limitations of the Model

The uncertainties in the radiative transfer calculations performed with MOCARAT can be attributed to various limitations of the modeling approach.

The statistical character of the Monte Carlo method bears inherent uncertainty. It is well known from the Central Limit Theorem that the standard deviation of an estimate of a quantity Q inferred from an ensemble of N samples is inversely proportional to the square root of the number of samples. In the case of the given Monte Carlo sampling routine, this translates to the relative statistical error of the radiance simulated in a certain bin of solid angle error being approximately given by the inverse square root of photons recorded:

$$\frac{\Delta R_{MC}(\mu_i, \varphi_j)}{R_{MC}(\mu_i, \varphi_j)} \approx \frac{1}{\sqrt{N_{i,j}}}. \quad (4.48)$$

Since the photons sampled on their trial through the atmosphere are assigned different statistical weights according to the transmissivity of their path, this relation holds only approximately.

Furthermore, various discretization errors occur. Due to the finite size of the solid angle bins, the radiance field is not computed for discrete values but is only given as an average value for the respective bin. In order to reduce the computational costs, the scattering phase functions, the bidirectional reflection distribution function and the molecular transmission are pre-calculated and stored in lookup tables. This gives rise to additional discretization and interpolation errors. Theoretically, these numerical errors can be reduced to any value by simply improving the discretization grid or increasing the number of samples, however at the expense of increased CPU time or memory usage.

The simplified representation of the physical processes induces additional systematic errors. Most notably, MOCARAT neglects the effects of polariza-

tion on the observed radiances. An accurate representation of polarization is beyond the scope of this study and would also require polarized Mie calculations for realistic aerosol models. Since both scattering phase functions and ocean reflectance depend on polarization, for certain geometries the interaction of these polarization effects could significantly influence the radiances. For example, only one polarization component of diffuse light incident on the ocean surface at the Brewster angle is reflected. Fortunately, for either scattering process, light scattered into the forward direction is almost unpolarized. Scattered light that contributes to the radiances observed in the sun glint region can be mostly attributed to forward scattering, which is almost unpolarized. The sun glint radiances are thus relatively unaffected by polarization effects.

Depending on the design of their internal optics, many remote sensing instruments are somewhat sensitive to polarization, which makes it even more desirable to account for polarization in the models. For example, the MCR's sensitivity to light with the electric vector polarized parallel to the scanning plane is somewhat different from that for polarization perpendicular to the scanning plane. For the MCR, for example, the polarization sensitivity, defined as the ratio the difference between the signals for the different planes of polarization and the total signal, has been measured to be between 4% and 5% (Curran et al., 1981). For a degree of polarization of 0.5, which is typical of ocean sun glint at small solar zenith angles (Takashima, 1985), this translates to a bias between observations and model results of up to 2.5 %.

MOCARAT is also limited by the simplified representation of subsurface scattering processes. Since, for the wavelengths of interest in this study, the contribution of subsurface scattering to the observed radiances is relatively small, the impact of these limitations on the overall radiances is reasonably small.

Further simplifications include the neglect of multiple reflections by the wave facets, the earth's sphericity and the refraction of the beam. For solar zenith angles and view zenith angles much smaller than 90° , these omissions are well justified.

In summary, for the wavelength ranges, solar and viewing geometries considered in this thesis, MOCARAT is reasonably accurate. The uncertainty of the MOCARAT results attributed to inherent model limitations will not exceed the error introduced by the uncertainty of the input data, most notably the atmospheric water vapor and trace gas profile and the assumptions made for the aerosol parameters, rather than the error of the model calculations.

CHAPTER 5

VERIFICATION

MOCARAT was implemented from scratch and therefore needed testing and verification before it could be considered as a reliable tool for applications. The peculiar features of MOCARAT are the inclusion of an anisotropically reflecting surface and the non-grey molecular absorption. Its radiative transfer in the atmospheric interior and the reflection at the ocean surface will be checked separately using two different, well established radiative transfer codes.

As described in Chapter 4, there are a number of solving algorithms as well as actual model implementations designed for a variety of applications. RADK is based on DISORT and an implementation of the correlated k -distribution method (Section 4.3.2). Since it is able to calculate band radiances in a scattering and absorbing atmosphere, it can be readily used for verification of the atmospheric radiative transfer component of MOCARAT.

More recently, non-isotropic reflection was included in the discrete ordinate models libRadtran and SBDART. As they can readily perform monochromatic radiative transfer calculations over a reflecting Cox-Munk ocean surface, it was possible to use them for an independent verification of the ocean reflection implemented in MOCARAT.

A large number of verification runs were performed during the development of MOCARAT. In the scope of this thesis, only a small number of these are documented in order to demonstrate the typical performance of the model. The test cases presented here have all been performed using a grid of 18 uniformly

spaced zenith angle values and 36 azimuthal angle values. The total number of photons sampled per run by MOCARAT is $5 \cdot 10^7$, the average number of photons per solid angle sampling bin hence being about 70000.

In order to quantify the agreement of the MOCARAT results with those of the reference models, the relative deviation in each grid point (μ_i, φ_j) was evaluated:

$$\Delta_{rel}(\mu_i, \varphi_j) = \frac{2(R_{ref}(\mu_i, \varphi_j) - R_{MC}(\mu_i, \varphi_j))}{R_{ref}(\mu_i, \varphi_j) + R_{MC}(\mu_i, \varphi_j)}, \quad (5.1)$$

where, R_{ref} , R_{MC} are the reflectances of the reference model and MOCARAT, respectively. The relative standard deviation is then given by the discretized integral over the upwelling hemisphere of the form

$$\sigma \approx \frac{1}{2\pi} \sum_{i=1}^{N_\mu} \sum_{j=1}^{N_\varphi} \Delta_{rel}(\mu_i, \varphi_j) \delta\Omega_{ij} \quad (5.2)$$

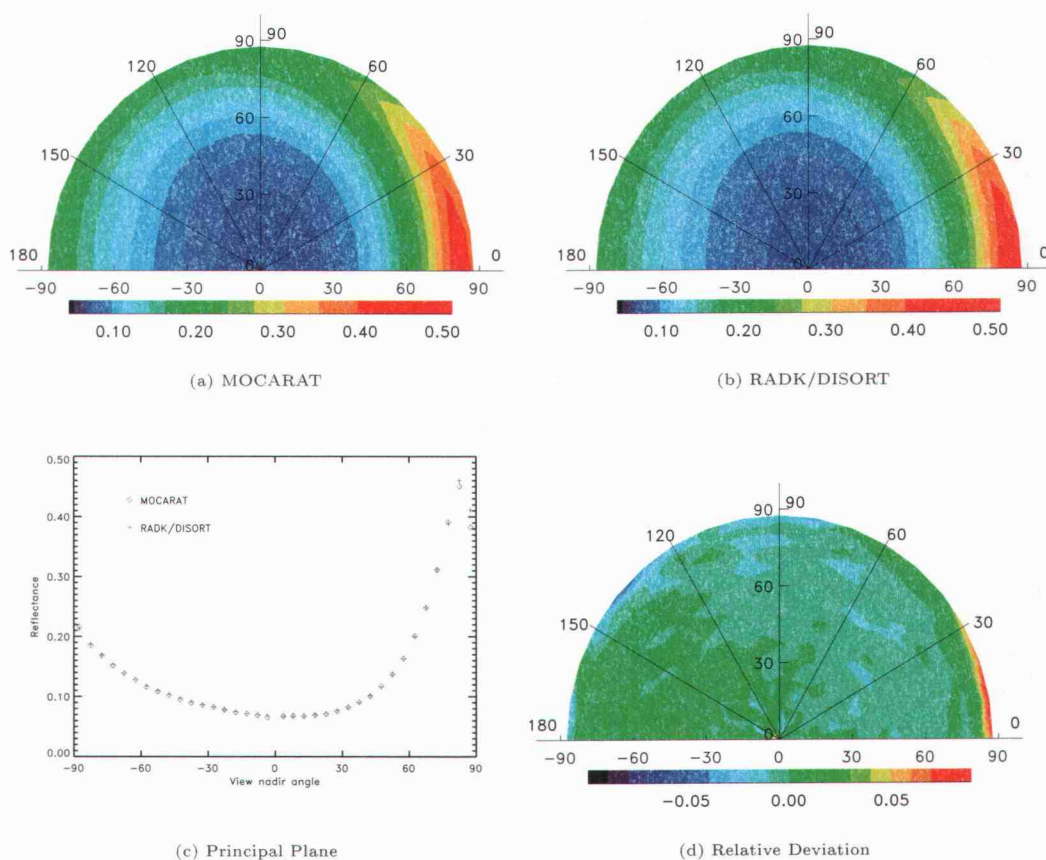
where $\delta\Omega_{ij}$ is the size of the solid angle bins.

5.1 Verification of Atmospheric Radiative Transfer: Comparison with RADK/DISORT

5.1.1 Test Case 1: MODIS Channel 1 Radiances, Low Surface Albedo

In the first test case, the radiance field in the spectral range of the MODIS channel 1 is considered. The atmospheric profiles of composition, pressure and temperature were adopted from the tropical standard model included in MODTRAN (Kneizys et al., 1996). A haze layer containing average continental aerosol of optical depth 0.6 at 550 nm is considered. Since RADK/DISORT cannot deal with anisotropic reflection, a Lambertian surface is assumed, and the albedo is set to 0.03.

FIGURE 5.1: Reflectances computed for test case 1. A polar plot of the results obtained by MOCARAT (a) and RADK/DISORT (b). Comparison of the principal plane reflectances computed by MOCARAT and RADK/DISORT (c). Polar plot of the relative deviation between the model results (d).



The results of both MOCARAT and RADK simulations are visualized as polar plots and given in Figures 5.1. Since the radiance field is symmetric with respect to the principal plane, it is sufficient to consider only azimuthal view solar angles in the range from 0° to 180° . The reflectances in the principal plane are given in Figure 5.1(c). Figure 5.1(d) shows the difference between the results of the two models. Away from the limb, the agreement is good with the deviation being well below 1%. At the limb, by contrast, the difference between the results is much larger. The difference can be mainly attributed to systematic differences in the modeling approaches. Whereas RADK/DISORT uses an analytical method to determine the radiances at *discrete* points, MOCARAT relies on a statistical technique to evaluate the *average* radiance in a solid angle bin. The deviation caused by this effect scales with the second derivative of the signal and is therefore strongest at the limb, where the variation in the radiance field is strongest. Furthermore, in the Monte Carlo model approach, at high view nadir angles, $\mu = \cos \vartheta$, fewer photons are sampled, but their statistical weight is proportional to $1/\mu$ and therefore very high. Hence, for the Monte Carlo results are less reliable at the limb, where $\mu \rightarrow 0$.

5.1.2 Test Case 2: Molecular Absorption and High Surface Albedo

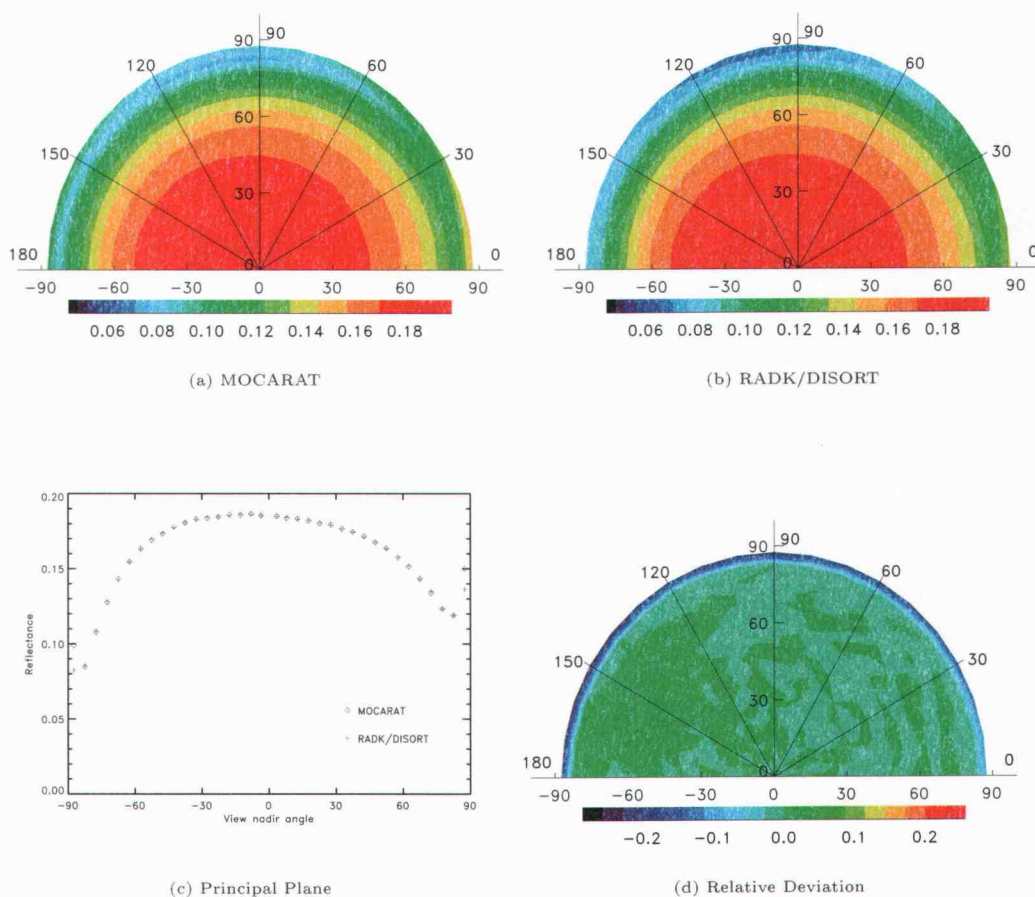
Although most radiometric channels used for the retrieval of aerosol properties are characterized by low molecular absorption, it is desirable to verify the model for a case of strong molecular absorption. For this purpose, the spectral wavelength band from $0.91 \mu\text{m}$ to $0.98 \mu\text{m}$ is considered. It contains the vibrational-rotational water vapor absorption band centered at $0.94 \mu\text{m}$ with a highly detailed structure and is therefore well suited for testing the molecular

absorption scheme of the model. A standard tropical atmosphere model was chosen. It is characterized by a large abundance of water vapor. The vertical water vapor column amount is 4.1 g/cm^2 .

Because this verification run focuses on molecular absorption, a thin layer of tropical marine aerosol of optical depth 0.1 at the reference wavelength $0.55 \mu\text{m}$ was considered. The lambertian surface albedo was set to a value of 0.5, which corresponds to, for example, a highly reflecting desert. The results for the top of atmosphere reflectances are presented in Figure 5.2.

Similar to test case 1, away from the limb the two models agree very well. As can be seen from the principal plane reflectances in Figure 5.2(c), the intensity decreases with increasing view nadir angle. The decrease is due to the higher absorption along a slant path of the light transmitted from the reflecting surface. At the limb, however, the reflectance increases again. The most likely reason for this effect is the vertical structure of the atmosphere. Whereas the mixing ratio of the strongly absorbing water vapor is highest in the lower atmosphere, the effective single scattering albedo in the upper atmosphere is much larger. At viewing angles close to 90° , the slant path through the upper atmosphere, along which photons can be scattered into the viewing direction without being subject to the high molecular absorption in the lower atmosphere, is very long. Hence the reflectance is high. This feature is captured more readily by MOCARAT, which averages over the solid angle bin, than by RADK/DISORT, which evaluates the reflectance only at a finite distance away from the limb. The limb values modeled by RADK/DISORT are therefore consistently smaller than those obtained with MOCARAT.

FIGURE 5.2: Reflectances computed for test case 2. A polar plot of the results obtained by MOCARAT (a) and RADK/DISORT (b). Comparison of the principal plane reflectances computed by MOCARAT and RADK/DISORT (c). Polar plot of the relative deviation between the model results (d).



5.2 Verification of Ocean Surface Reflection: Comparison with libRadtran and SBDART

More recently, DISORT-based radiative transfer models with non-isotropic surface reflection have become available. The incorporation of non-lambertian albedos is accomplished by expanding the bidirectional reflectance distribution function (*BRDF*) in spherical harmonics. Such implementations exist for both the radiative transfer software library libRadtran (Kylling and Mayer, 2002) and the Santa Barbara Discrete Ordinate Radiative Transfer model SBDART, which were used for this verification.

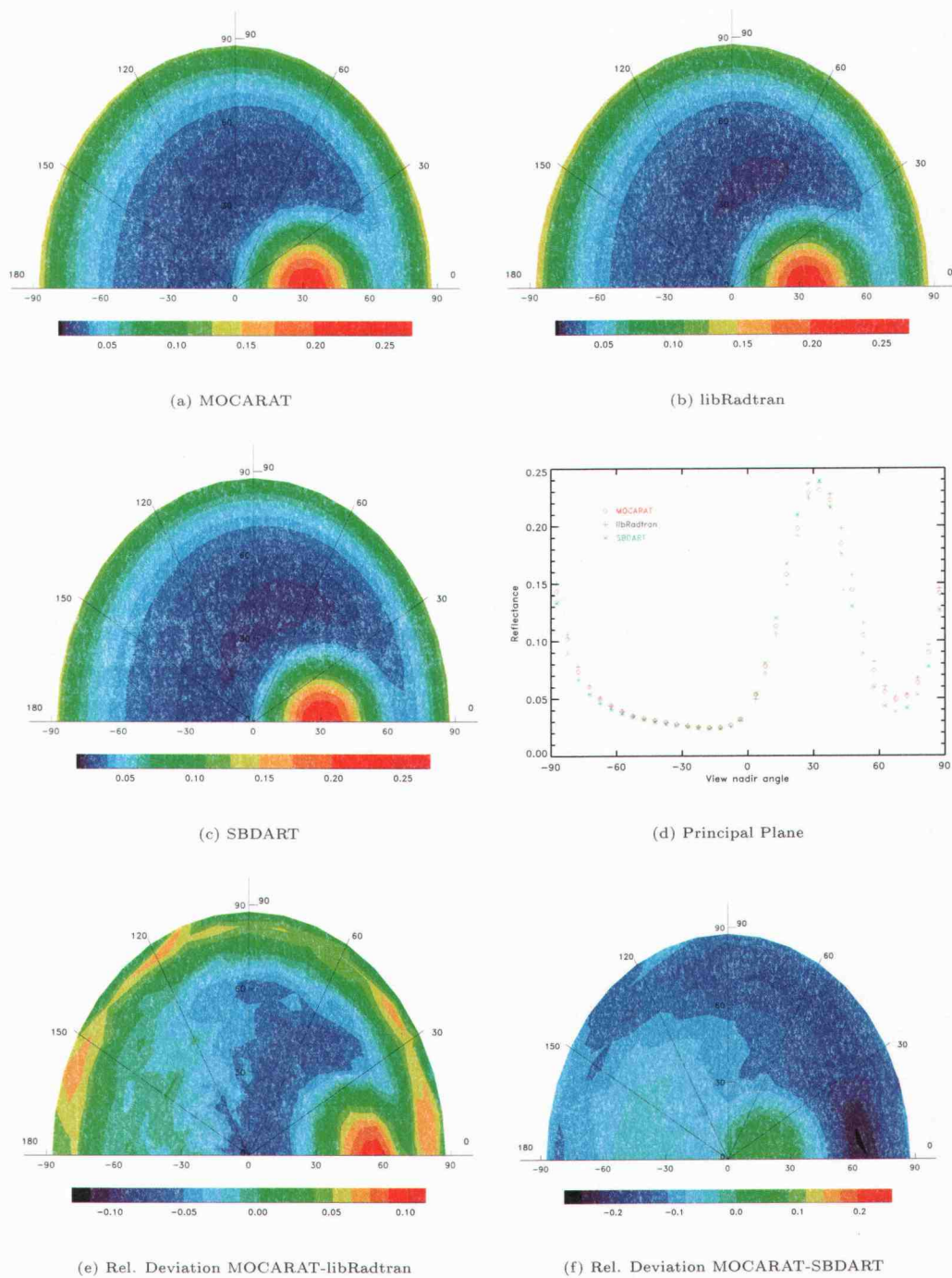
5.2.1 Test Case 3: Reflecting Ocean Surface with Isotropic Slope Distribution

The current version of SBDART only supports the simulation of an isotropic slope distribution of the form (2.41). In order to include SBDART in the model comparison, for this test run an isotropic slope distribution is also considered for MOCARAT and libRadtran. LibRadtran was originally only designed to account for an anisotropic slope distribution of the form (2.35) due to a wind field with a well defined direction. However, it was possible to modify the source code in order to implement an isotropic distribution.

For the sake of simplicity, monochromatic radiances at a wavelength of $0.64 \mu\text{m}$ were simulated. Again, the molecular profiles were taken from the standard tropical atmosphere. Rayleigh scattering was included, however no Mie extinction was considered. The wind speed was set to 5 m/s, and the solar zenith angle was 30° .

The output of the three models for this verification run are depicted in Fig-

FIGURE 5.3: Reflectances computed for test case 3. Polar plots of the results obtained by MOCARAT (a), libRadtran (b), and SBDART (c). Comparison of the principal plane reflectances (d). Polar plots of the relative deviation between the reference models and MOCARAT (e), (f). Note change in scale.



ure 5.3. Their results are consistent, however, the agreement is not as good as that obtained with RADK/DISORT for test cases 1 and 2. Nonetheless, taking into account that the models use different parameterizations for atmospheric Rayleigh scattering and molecular absorption, subsurface scattering, as well as conversion of the slope distribution into the BRDF, the agreement is reasonable. At the nadir side of the sun glint peak, the SBDART reflectances are greater than the MOCARAT results where those of libRadtran are smaller. On the limb side of the sun glint pattern, by contrast, the SBDART results are smaller and the libRadtran results are larger than the MOCARAT output. The discrepancies away from the sun glint and at the limb suggest that there is also a slight difference in the treatment of scattering and absorption.

Overall, MOCARAT's agreement with libRadtran is somewhat better than that with SBDART. Whereas the relative standard deviation between MOCARAT and libRadtran is some 3.1 %, the MOCARAT-SBDART standard deviation is as high as 4.5 %.

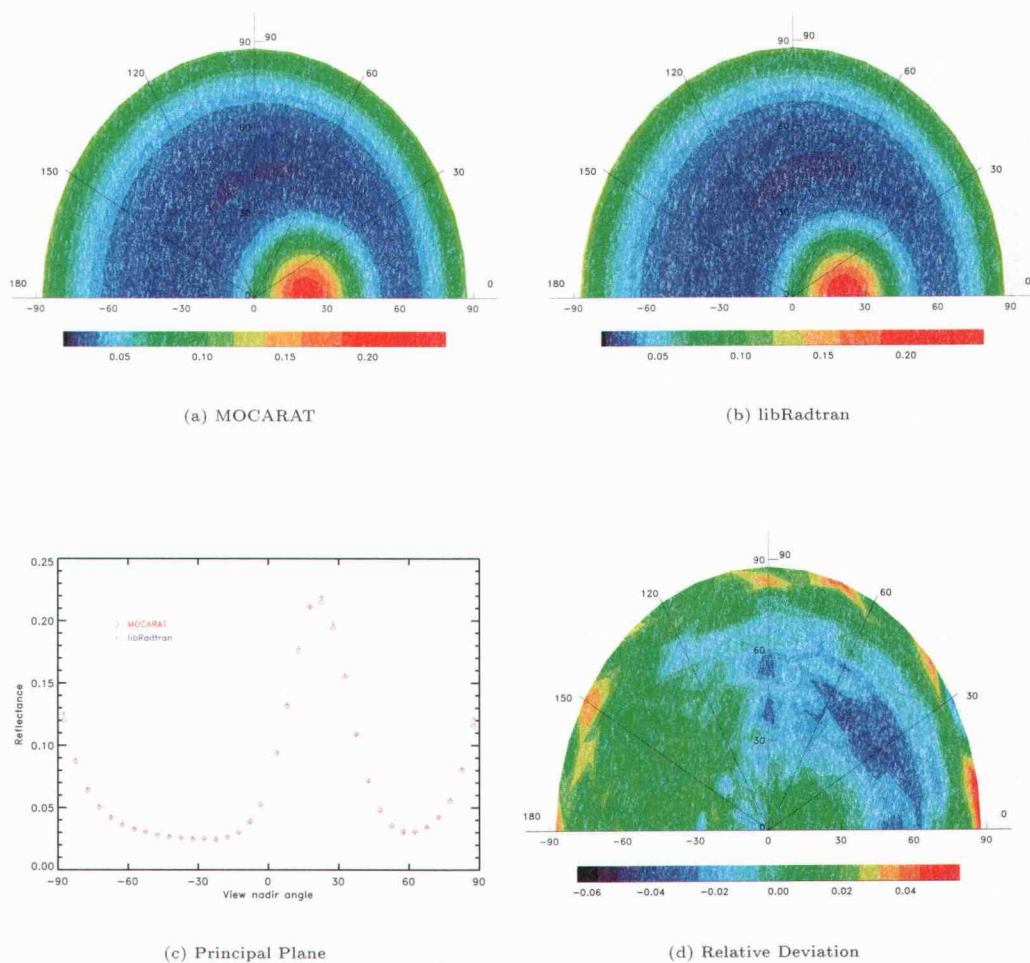
5.2.2 Test Case 4: Reflecting Ocean Surface with Anisotropic Slope Distribution

For the last test case presented in this thesis, a reflecting oceanic surface is considered where the wind direction is well defined. The slope distribution is then given from (2.39). It is anisotropic and symmetric with respect to the principle axis which is aligned with the wind direction.

Since SBDART cannot simulate the reflection from the anisotropic ocean surface, only MOCARAT and libRadtran were considered for this test case.

As in test case 3, a simplified atmosphere without aerosol scattering and

FIGURE 5.4: Reflectances computed for test case 4. Polar plots of the results computed by MOCARAT (a) and libRadtran (b). The principal plane reflectances are given in (c). (d) is a plot of the relative deviation between MOCARAT and libRadtran



absorption was considered. Only Rayleigh scattering and molecular absorption were taken into account. The radiance field was modeled with solar radiation incident at an angle of 20° .

For the ocean surface reflection, the surface wind speed was assumed to be 5 m/s and the wind direction was set to be aligned with the azimuthal direction of solar incidence.

The results of this verification run are shown in Figure 5.4. The two models agree very well, particularly in the sun glint region. Minor disagreements exist away from the sun glint and at the limb. Since fewer photons are sampled at the limb, the results of MOCARAT are less reliable. In addition, as described in Section 5.1, the bias due to the averaging over a solid angle bin in MOCARAT is strongest at the limb. The standard deviation between MOCARAT and libRadtran for test case 4 is 1.4%.

CHAPTER 6

REMOTE SENSING APPLICATIONS OF SUN GLINT

6.1 Method

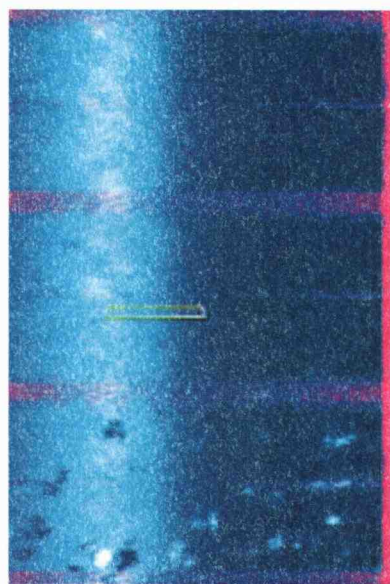
Modeling of sun glint radiances depends on the characterization of the sea surface roughness. The Cox-Munk theory is an adequate theoretical tool for relating the slope statistics to the surface wind field. Nevertheless, the Cox-Munk theory was developed almost 50 years ago. It is a purely empirical representation and its accuracy is not well documented. In any case, for most applications, independent information on surface wind speed and direction is unavailable.

In some cases, it is possible, to retrieve statistical parameters of the surface slope distribution from the observed radiance field. From the MCR data, for instance, the width of the sun glint pattern, which is related to the magnitude of the wind speed, is readily obtained. However, since a scanning instrument, such as the MCR, only records a one-dimensional cross section of the sun glint, there is no information about wind direction.

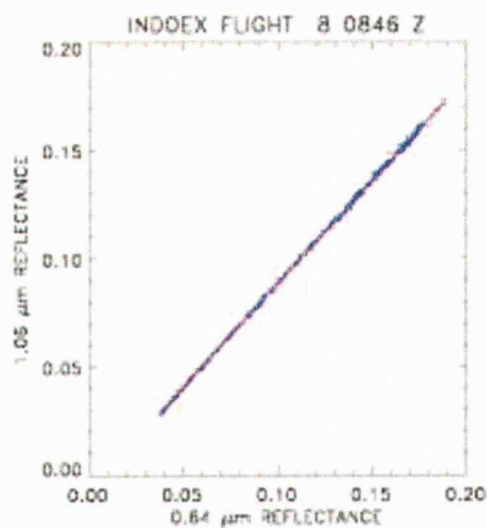
Additional complications arise for satellite borne radiometers. Due to the high flight altitude, the sun glint spreads over a region of several hundred kilometers at the ground. Consequently, the wind field cannot be considered constant over the entire region of sun glint.

For ideal observation conditions, i.e. small solar zenith angle, an appropriate azimuthal angle between the sun and the scanning direction, moderate wind speed and aerosol load, a very strong and distinct sun glint is observed.

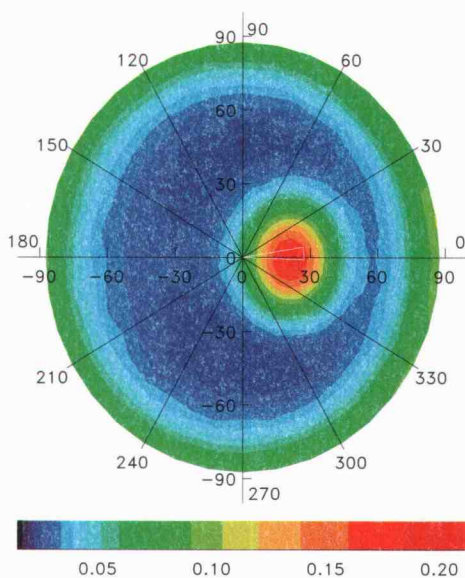
FIGURE 6.1: Analysis of the correlation of sun glint reflectances observed during INDOEX Flight 8 by the MCR. The highlighted box in (a) shows the pixels used for the analysis. The correlation diagram for channels 1 and 4 (b). Modeled reflectances (c) and correlation (d) of the grid points corresponding to the observational pixels used. Tropical marine aerosol was considered and results in (d) are given for reference optical depths of 0.05, 0.10, 0.20.



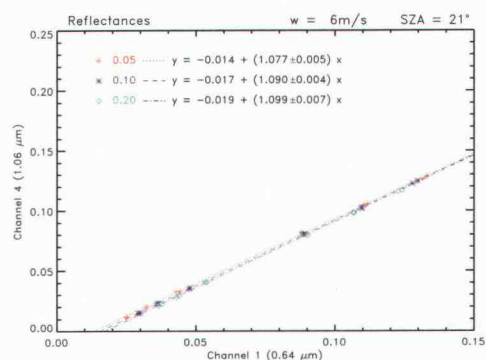
(a) MCR Scene



(b) Correlation of Observed Data



(c) Modeled Reflectance



(d) Modeled correlation

In such cases, radiances for different channels through the sun glint are found to be almost linearly related. Furthermore, the slopes of the relationships are much more robust with respect to the wind field than are the absolute values of the radiances. It is therefore proposed to use linear regressions of the sun glint reflectances to check the relative (channel-to-channel) calibration of imaging radiometers. As will be demonstrated in the following section, the linear coefficients turn out to be sensitive to aerosol extinction and absorption. This sensitivity suggests that the correlations can also be used for the retrieval of the spectral dependence of aerosol extinction and hence provide information on effective size.

For the analysis, a certain set of sun glint pixels of a perfectly cloud-free region is identified in the observed data. In a correlation diagram, the channel radiances are plotted for each pixel. Given the solar geometry, the radiance field is modeled using MOCARAT, thereby providing theoretical estimates for the channel correlations.

An example of the correlation and regression is given in Figure 6.1. The regressions were performed using a standard maximum likelihood estimators (e.g. Press et al., 1980, ch. 15). Comparison of the slope of the regression to the ratio of the Fresnel reflection gives information about the atmosphere. The attenuation of a beam incident at the top of the atmosphere and reflected at the ocean surface equals the product of the reflectance and the atmospheric extinction. Hence, using single scattering theory, the ratio of atmospheric path transmittance approximately equals the quotient of ratio of Fresnel reflection and the reflectance in the sun glint center.

Additionally, the linear regression is constrained by the reflectances at the edge of the sun glint. The offset of the linear regression can be interpreted

in terms of the difference in the atmospheric backscattering. Away from the sun glint, the upwelling radiation is mostly due to diffuse light scattered from the atmosphere and ocean. As can be seen from the results in Section 5.1, this diffuse contribution is almost constant away from the limb. Because of the decreasing Rayleigh, Mie and subsurface scattering, the diffuse radiation strongly decreases with wavelength. The offset for the correlation of the near IR channels with channel 1 is therefore always negative.

Once the absolute calibration of one radiometric channel is well established, the performance of all other channels might be calibrated with respect to it using the sun glint correlations. Thus, the sun glint radiances could be used for the relative calibrations of the channels.

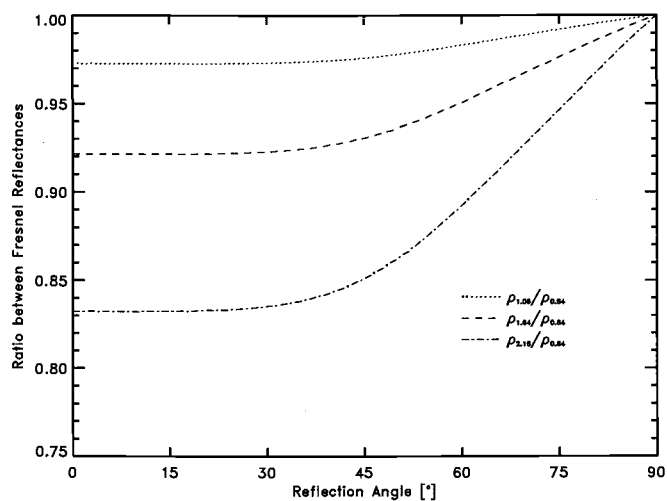
As will be demonstrated in the following section, because of uncertainties in the wind field, the predictions of the absolute radiances in the sun glint region are somewhat uncertain. The relationships among the reflectances, on the other hand, are relatively insensitive to the wind.

6.2 Sensitivity Studies

In order to assess the sensitivity of the of the correlation to atmospheric and observational parameters, channel radiances were modeled for different conditions. Simulations were performed for the MCR channels 1, 4, 5 and 6, which are the most relevant for aerosol research. For all sensitivity studies the reflectances were considered at an altitude of 6 km, which is typical for aircraft observations, and, aside from the profiles used in Section 6.2.5, the tropical standard atmosphere was used for the profiles of pressure, temperature, and chemical constituents.

As discussed in Section 3.3, the aerosols typical of continental air are distinctly different from those typical of tropical marine air and the differences lead to distinctly different optical properties. The effective radius of the continental aerosols is small, therefore the extinction decreases strongly with wavelength in the relevant spectrum. The aerosol contains soot, so that the single scattering albedo is of order 0.9. The tropical marine aerosol, by contrast, is composed of sea salt aerosol and other water soluble species and characterized by a rather large effective radius of about $1 \mu\text{m}$. Hence, the extinction is almost constant with wavelength with an Ångström coefficient close to 0. Because of these distinctly different properties, the sensitivity of the reflectance correlations to other parameters is quite different for the two aerosols.

FIGURE 6.2: Ratios of the Fresnel reflectances for MCR wavelength channels 1 ($0.64 \mu\text{m}$), 4 ($1.06 \mu\text{m}$), 5 ($1.64 \mu\text{m}$), and 6 ($2.16 \mu\text{m}$) as a function of reflection angle.



6.2.1 Average Continental Aerosol

The radiation field was simulated for a number of different solar geometries, aerosol optical depths and wind speeds. The sensitivity of the proposed correlation method is then assessed by comparing the slopes of the regression for different values of one of the parameters with all other parameters held fixed.

In order to determine the sensitivity to aerosol load, the radiances were modeled for different aerosol optical depth. Since the aerosol optical depth depends on wavelength, it is common to specify the aerosol abundance by the aerosol optical depth at the reference wavelength $0.55 \mu\text{m}$. Values of 0.10, 0.35 and 0.60 were chosen for τ_{ref} , where $\tau_{ref} = 0.10$ corresponds to clean air and the range of 0.35-0.60 is typical for the polluted air of the northern hemisphere close to the continents (Tahnk, 2001).

The correlation diagrams of channels 4, 5, and 6 with channel 1 are given in Figure 6.3 (a), (c), (e). The simulations were performed for a wind speed of 8 m/s and the solar zenith angle was set at 20° , a value typical of the sun glint scenes found in the INDOEX MCR data.

The correlations are nicely described by a linear regression. For all of the near IR channels the slopes strongly increase with increasing aerosol load. This increase can be interpreted in terms of the wavelength dependence of the aerosol extinction. For the continental aerosol, the aerosol extinction strongly decreases with increasing wavelength. Hence, an increase of the aerosol load affects the $0.64\text{-}\mu\text{m}$ channel much more than the the near IR channels, resulting in an increase of the correlation slope. As expected, in going from channel 4 to channel 6, the sensitivity to aerosol load is found to increase with increasing wavelength.

For comparison, Figure 6.2 shows the ratios of Fresnel reflectances for the

different wavelength channels as a function reflection angle. Note that, even for low aerosol loads, the slope exceeds the ratio of Fresnel reflectance. Atmospheric extinction, including both aerosol and molecular effects, in channel 1 is greater than that in the near IR channels. The difference is due to Rayleigh scattering, which decreases even more strongly with wavelength than the aerosol extinction.

6.2.2 Tropical Marine Aerosol

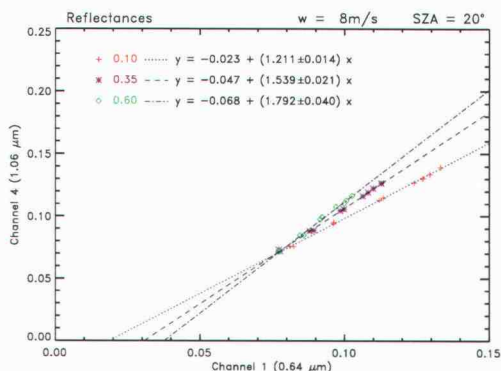
The sensitivity tests described above for the average continental aerosol were also performed for a tropical marine aerosol. The corresponding correlation diagrams are shown in 6.3 (b), (d), (f).

The resulting parameters for the regression of the correlation are somewhat less sensitive to aerosol load than those for the average continental aerosol. For the correlation of the 1.06 μm and the 0.64 μm channels, for example, the slope ranges from 1.11 for a tropical marine aerosol optical depth of 0.1 to 1.51 for an aerosol optical depth of 0.6. For comparison, this range is 1.21 to 2.10 for the same range of average continental aerosol burden.

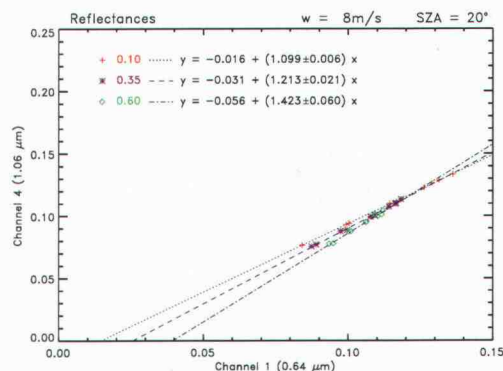
The weaker dependence on aerosol optical depth for the marine aerosol can be explained in terms of the weaker wavelength dependence of the aerosol extinction. An increase of aerosol optical depth in the visible corresponds to an increase of similar magnitude in the near IR. Furthermore, for the larger marine aerosol, the scattering is strongly peaked in the forward direction and therefore scattered photons may well end up in the sun glint region.

In order to demonstrate that the decreased aerosol sensitivity is an effect that must be attributed to size distribution rather than the differences in aerosol absorption that exist between the average continental and the tropical marine

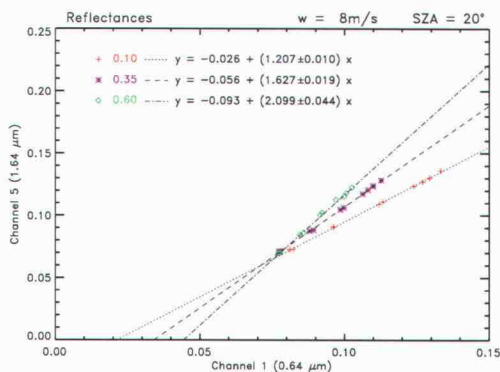
FIGURE 6.3: Correlation diagrams for the sun glint reflectances of the MCR's wavelength channels. Figures (a), (c), (e) show the sensitivity to average continental aerosol burden. Figures (b), (d), (f) show the sensitivity to tropical marine aerosol burden.



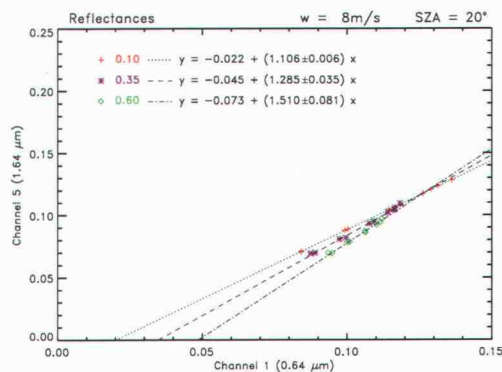
(a) Average Continental Aerosol



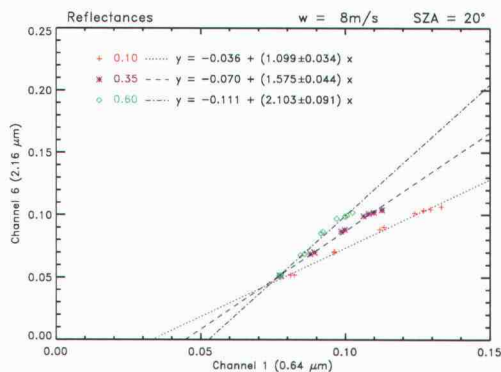
(b) Tropical Marine Aerosol



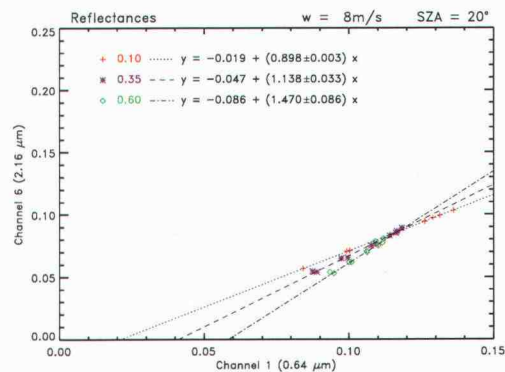
(c)



(d)

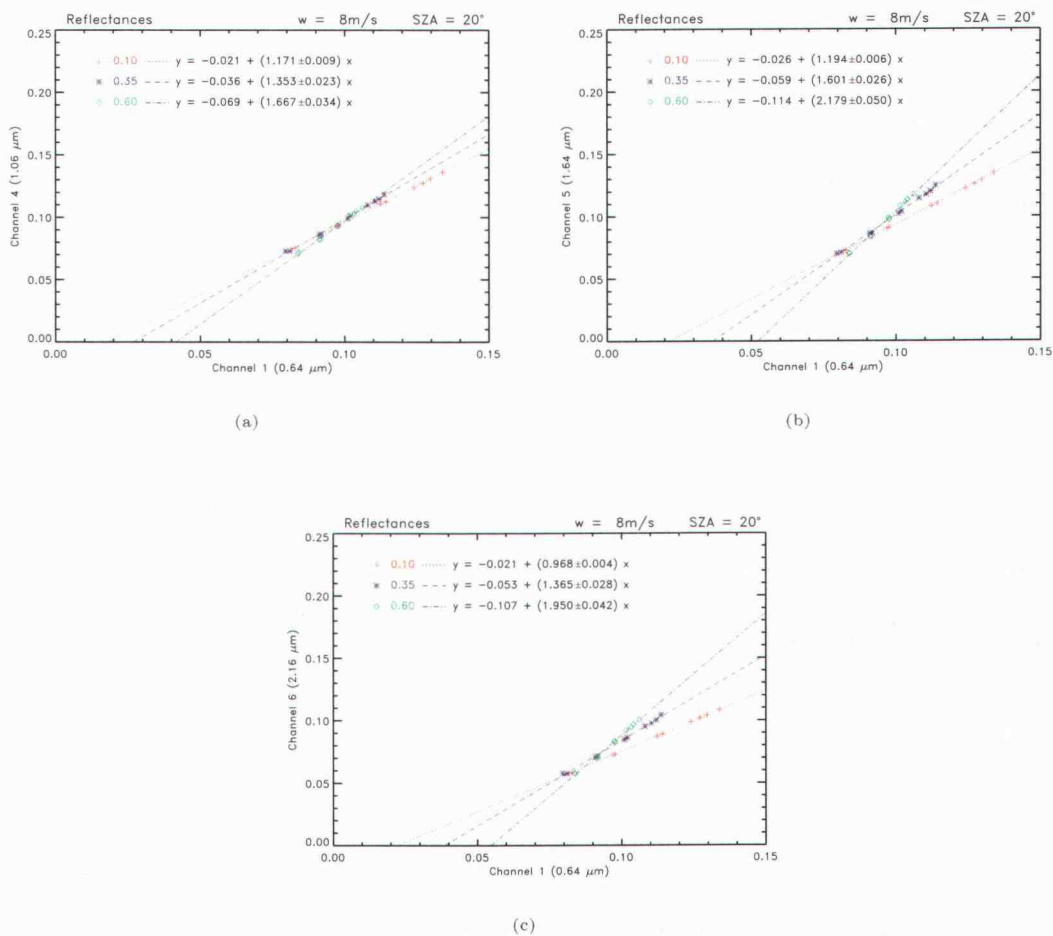


(e)



(f)

FIGURE 6.4: Sensitivity to aerosol burden for the NOAA Phase 2 aerosol model.



aerosol, it is worth considering the NOAA Phase 2 aerosol model. This aerosol model represents an aerosol with small non-absorbing particles. It is characterized by a very small effective radius of $0.1\ \mu\text{m}$ and a single scattering albedo of unity (Stowe et al., 1997). It turns out that the dependence of the slope on optical depth is similar or even exceeds that obtained for the average continental

aerosol. The sensitivity is particularly striking for channels 5 and 6 (Fig. 6.4).

The uncertainty in the slopes can be obtained from the regression. It is mostly due to departures of the actual correlation from the assumed linearity. The uncertainty is found to increase with aerosol burden. With increased aerosol abundance, the reflectance away from the sun glint increases whereas the reflectance in the center of the sun glint decreases. Higher aerosol loadings therefore result in a less distinct sun glint pattern and a smaller dynamic range for the correlations, which also makes the regression somewhat less constrained.

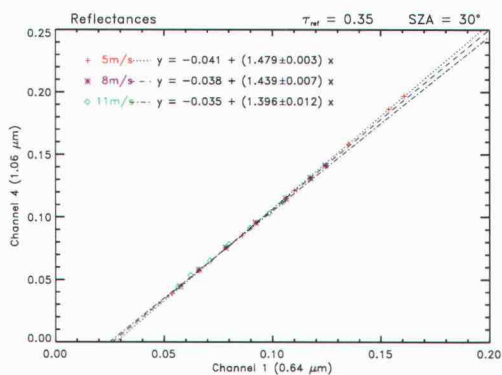
6.2.3 Wind Speed and Direction

For many remote sensing applications, there is only limited knowledge of the surface wind field. It is therefore particularly important to assess the dependence of the proposed correlation method on surface winds.

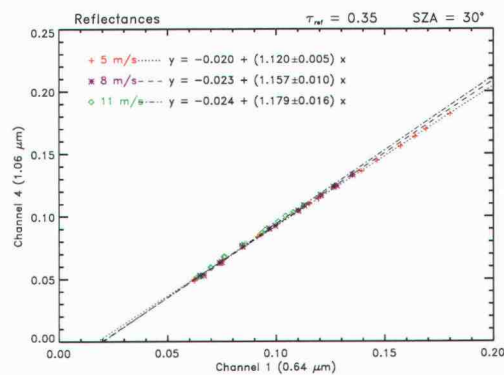
An increase in wind speed results in a wider distribution of wave slopes and a smoothed sun glint pattern. Again, this results in a reduced dynamical range of the reflectances and more uncertainty in the regressions. As shown in Figure 6.5, the correlations of the sun glint reflectances are only weakly sensitive to wind speed. The correlations presented here were obtained from simulations with a solar zenith angle of 30° and an aerosol load of $\tau_{ref} = 0.35$ for both average continental and tropical marine aerosol. The sensitivity turns out to depend on aerosol type. For average continental aerosol, the slope of the regression is found to decrease weakly, but consistently with wind speed. For tropical marine aerosol, by contrast, the slope tends to increase with wind speeds.

As discussed in Sections 2.5.1 and 4.4.2, the surface slope distribution also depends on wind direction. For scanning imagers such as the MCR, MODIS and

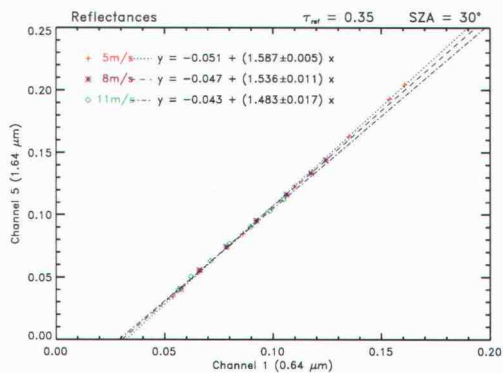
FIGURE 6.5: Sensitivity to wind speed. Figures (a), (c), (e) show the sensitivity for average continental aerosol. Figures (b), (d), (f) show the sensitivity for tropical marine aerosol.



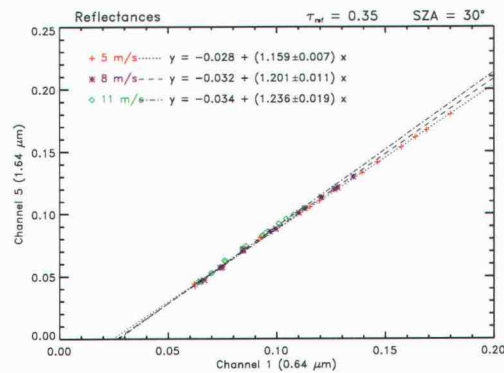
(a) Average Continental Aerosol



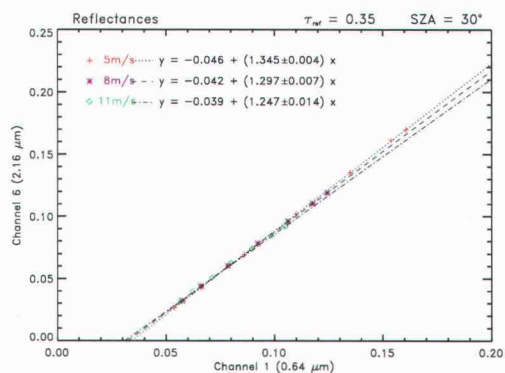
(b) Tropical Marine Aerosol



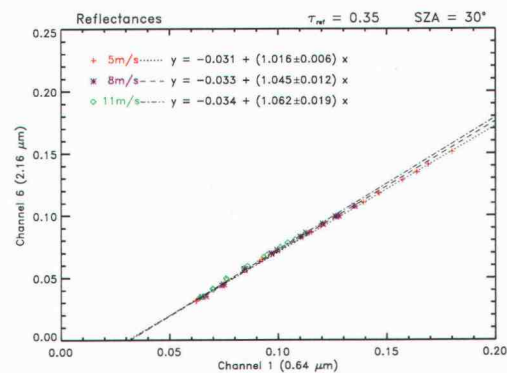
(c)



(d)



(e)



(f)

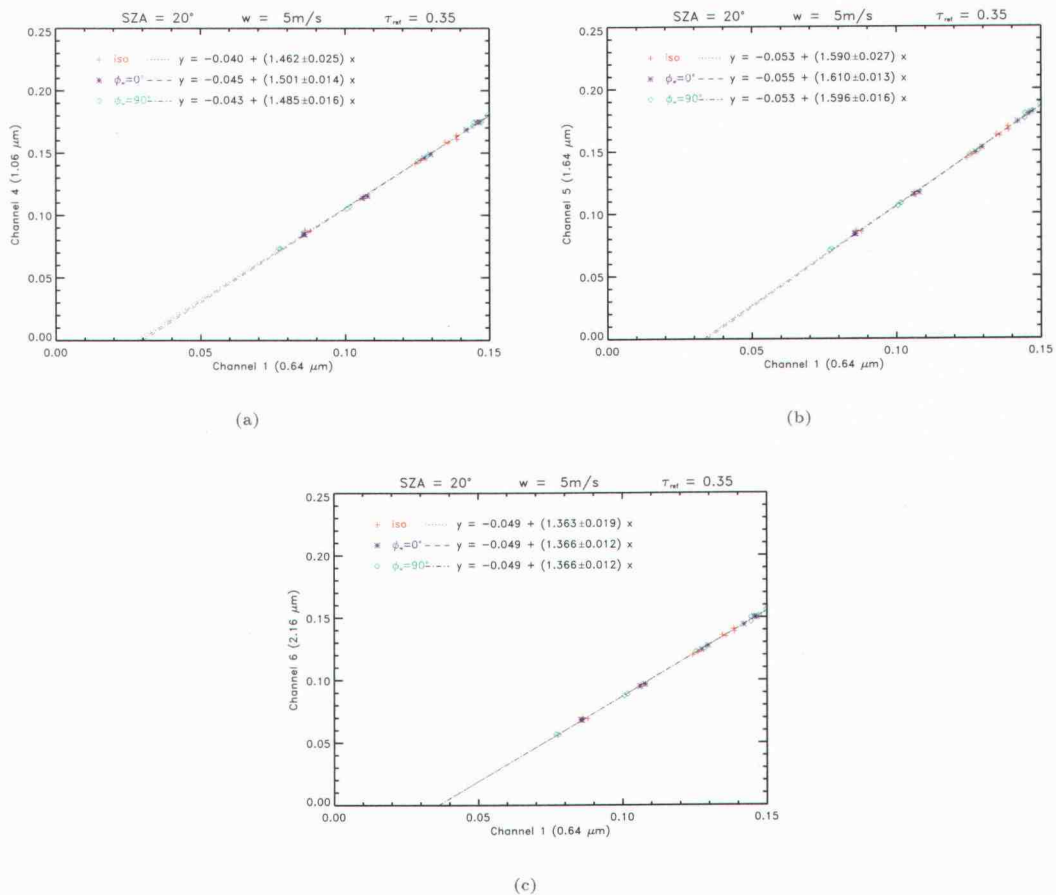
many other radiometers, only a one-dimensional cross section of the radiance field is obtained. Unlike two-dimensional imaging, such as the photographs considered by Cox and Munk (1954a), it is not possible to retrieve wind direction from a cross section obtained with a scanner. Wind direction certainly influences the absolute radiances, and it is necessary to assess its influence on the correlations. Therefore, comparisons were performed for three different slope distributions. First, the isotropic slope distribution (2.41) was considered. In addition, realistic slope distributions of the form (2.39) were considered for the two cases of the wind direction parallel to and perpendicular to the scanning direction. The results for the average continental aerosol at a reference aerosol optical depth of 0.35 and a solar zenith angle of 20° are presented in Figure 6.6. The deviations are found to be rather small and within the error of the regression.

6.2.4 Solar Geometry

An increase in solar zenith angle causes an increase of the optical pathlength for both aerosol and molecular extinction. For remote sensing applications, the solar zenith angle is readily available. For most aircraft borne observations, such as those performed with the MCR during INDOEX, the horizontal extent of the observed domain is on the order of 10 km, and the solar zenith angle can be assumed to be constant over the scene. For satellite observations, by contrast, the scenes extend over hundreds of kilometers, and the spatial variation of the solar zenith angle can become significant even for sub-domains of the sun glint.

It turns out that the sensitivity is very different for different atmospheric and observational parameters. In the visible, the Rayleigh and Mie extinctions are

FIGURE 6.6: Analysis of the sensitivity of the correlation method to wind direction. Calculations were performed for an isotropic distribution (iso), and anisotropic distributions with relative azimuth angles $\varphi_w = 0^\circ, 90^\circ$. An average continental aerosol was assumed.



greater than in the near IR. MCR's near IR channels, however, have stronger molecular absorption than the 0.64- μm channel. For higher solar zenith angle, the increased molecular absorption in channels 4, 5, 6 therefore tends to balance the increased aerosol and Rayleigh extinction in channel 1.

Four examples of sensitivity to solar zenith angle are given in Figure 6.7.

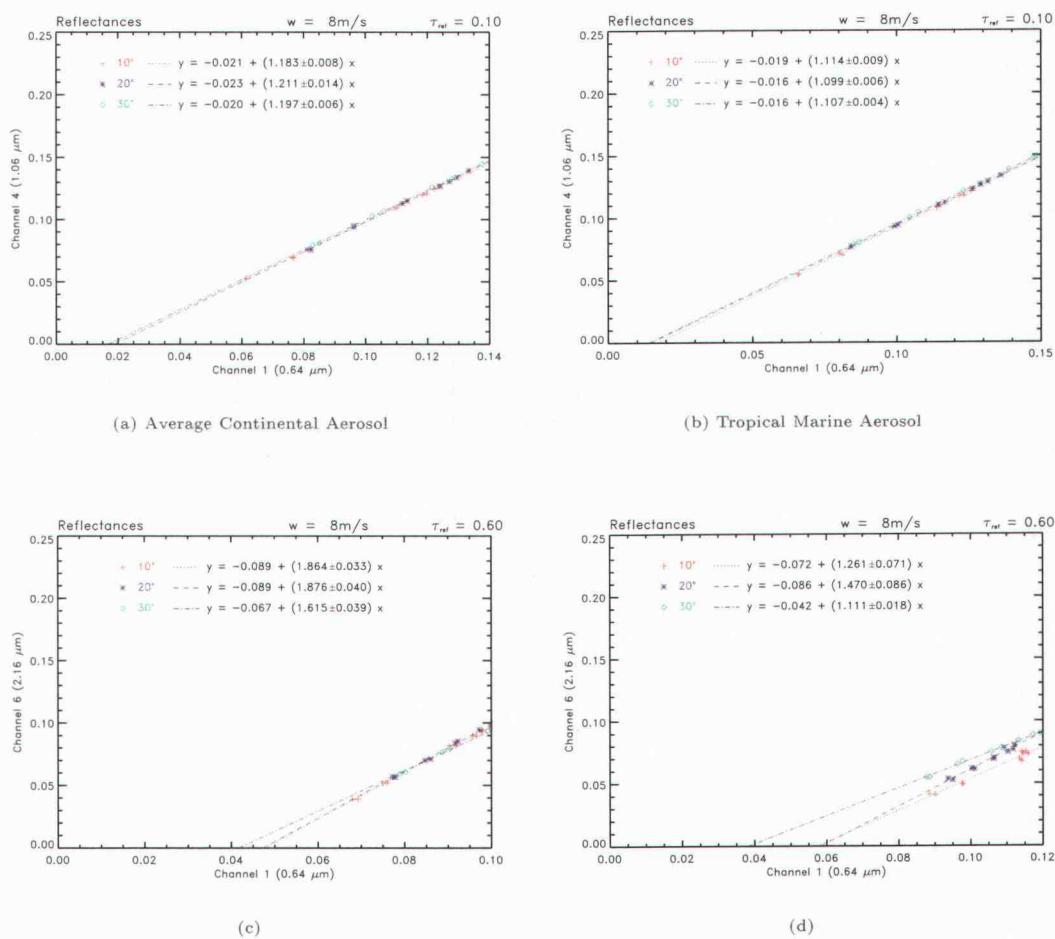
Correlation diagrams are presented for both tropical marine and average continental aerosol. The optical depths are $\tau_{ref} = 0.10$ for channel 4 and $\tau_{ref} = 0.60$ for channel 6. For an aerosol burden of $\tau_{ref} = 0.10$, the slope of the channel 1 vs. channel 4 correlation is almost constant for different solar zenith angles (Figure 6.7a-b). For other configurations, the correlations depend considerably on solar zenith angle. This is the case in channel 6 for the larger aerosol abundances (Figure 6.7c-d). Interestingly, the slopes for solar zenith angles 10° and 30° turn out to be smaller than that for 20° . The slope being non-monotonic in the extinction path length might be due to the non-gray molecular absorption, that is rather significant in channel 6. Clearly, the sensitivity is greater as aerosol burden increases.

For many remote sensing applications, the relative azimuthal angle between solar incidence and the viewing direction, which in the case of the MCR is given by the scanning line, must be considered. The relative azimuth angle is readily available from the flight data, so it is possible to include it in the analysis.

When the scanning line is in the principal plane, the observed reflectance cross section contains the center of the sun glint and the dynamic range is strongest. By contrast, in the case of off-axis scanning away from the principle plane, for sufficiently large relative azimuth angle and depending on wind speed and direction, the scanning instrument might only transect the edge of the sun glint pattern where the maximum observed reflectance would be considerably smaller than in the principal plane case.

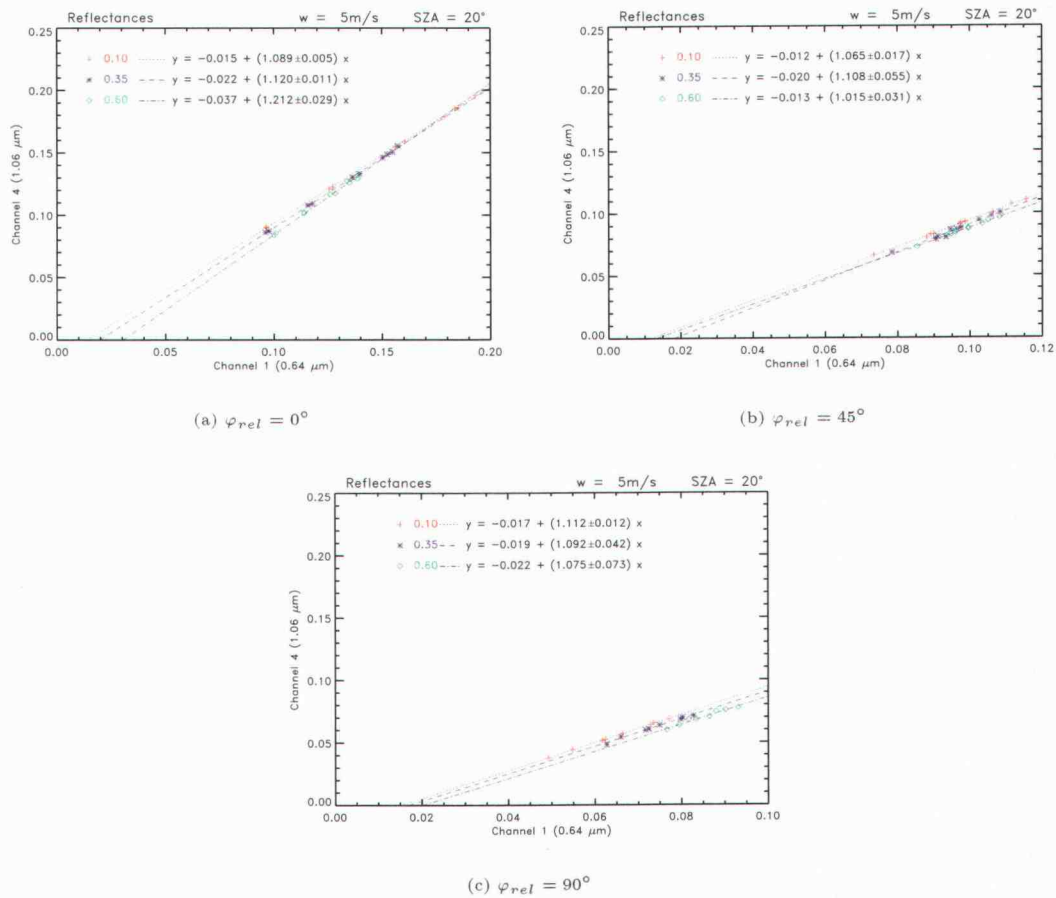
The modeled correlations are sensitive to relative azimuth angle. In Figure 6.8 the channel 4 versus channel 1 correlations are presented for relative azimuth angles of 0° , 45° , and 90° are presented. Tropical marine aerosol and a solar zenith angle of 20° is considered. Particularly for large aerosol loads,

FIGURE 6.7: Correlation diagrams for the sun glint reflectances of the MCR's wavelength channels. Figures (a), (c) show the sensitivity to solar zenith angle for average continental aerosol. Figures (b), (d) show the sensitivity to solar zenith angle for tropical marine aerosol.



the correlations are less constrained and the uncertainty in the regression increases. Further model calculations were performed and it was found that in the case of off-axis scanning the sensitivity to the surface wind field is somewhat

FIGURE 6.8: Modeled correlation between channel 1 and channel 4 radiances for different relative azimuth angles φ_{rel} between scanning line and solar incidence.



enhanced.

6.2.5 Water Vapor Abundance

For tropical conditions in particular, water vapor is the most important absorber in the MCR channels. The spatial and temporal variability of its abundance is also very large. Since water vapor differs in the different channels, it is necessary to assess the dependence of the correlation method on water vapor burden. All the sensitivity studies presented above were performed assuming a water vapor profile from the tropical standard atmosphere. In this section, the results for the tropical profile shall be compared with two other profiles with significantly lower integrated water vapor amounts.

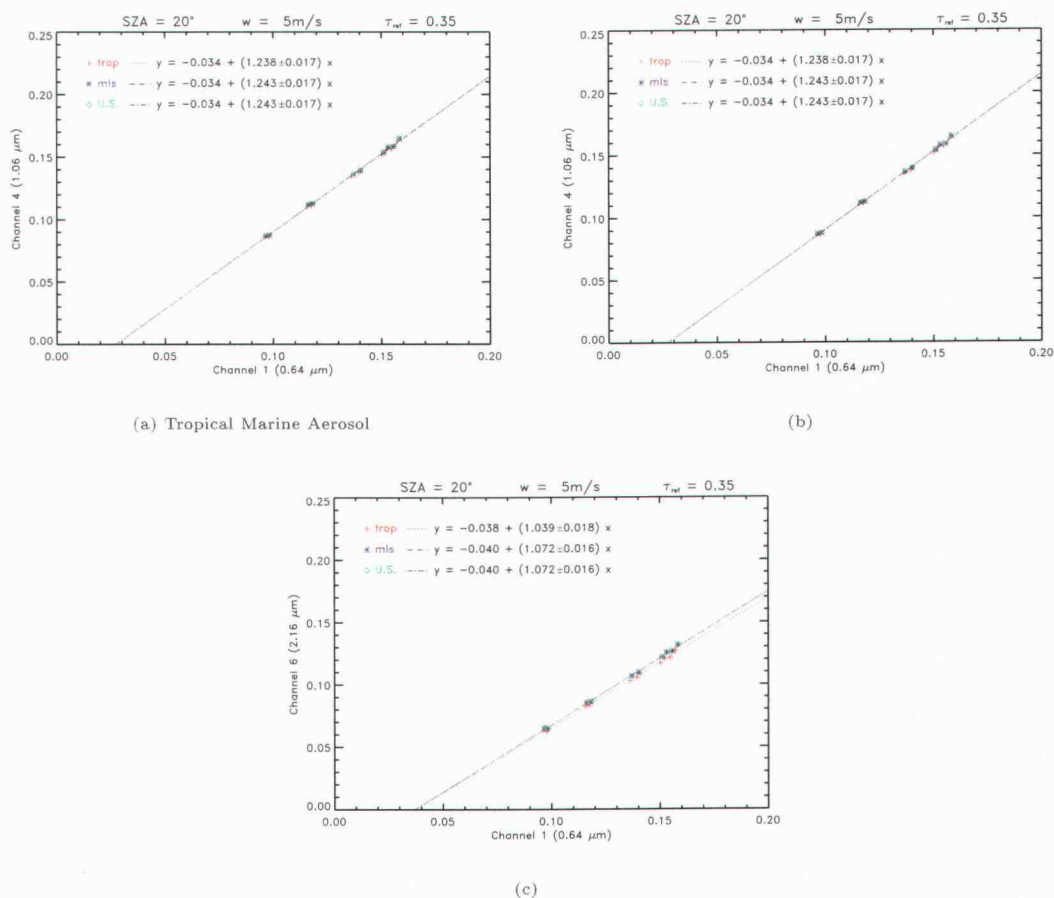
In addition to the tropical profile, a standard mid-latitude summer model and the U.S. Standard Atmosphere have been considered. Their cumulative H₂O amounts are 1.4 g/cm² and 2.9 g/cm², which compares to 4.1 g/cm² for the tropical model. For all other atmospheric constituents, the profiles from the tropical model were used.

The results are given in Figure 6.9 for a solar zenith angle of 20° and tropical marine aerosol at an optical depth of 0.35. Due to the small molecular absorption, it is found that the sensitivity to H₂O abundance is rather insignificant for channels 1, 4 and 5. For channel 6, by contrast, the effect of water vapor abundance is noticeable. The slope of the reflectance correlations is found to increase by about 3% for the U.S. standard atmosphere compared with the tropical water vapor model.

6.3 Consistency of calibration of the MCR

The results of the sensitivity studies presented in the previous sections suggest that it is possible to obtain relative calibrations for the in-flight performance

FIGURE 6.9: Sensitivity to water vapor abundance. Simulations were performed for H₂O profiles from a tropical (trop), and a mid-latitude summer (mls) model, as well as the U.S. 1976 Standard Atmosphere (U.S.).



of imaging radiometers from sun glint. For the MCR, the gains of various channels were adjusted several times during the INDOEX campaign. Even though the gain changes were recorded and accounted for in the data processing, it is necessary to check the consistency of the calibration used for the data processing.

The geographic region where INDOEX was conducted is characterized by

its low latitude where the sun is high during the day. Therefore sun glint was encountered frequently by the nadir looking MCR. Clearly the ocean of the southern hemisphere is best suited for the calibration. Due to the absence of anthropogenic and continental aerosol sources, the typical aerosol load is rather small and ranges from 0.05 to 0.20, which compares to values of 0.5 and larger encountered in the northern hemisphere. As pointed out by Tahnk (2001) and Coakley et al. (2002), the aerosol abundance in the Indian Ocean south of the ITCZ can be well described by a tropical marine aerosol model composed of sea salt aerosol and sulphate aerosol with a large effective radius and a single scattering albedo close to unity. Because of the large size, the aerosol extinction is only weakly dependant on wavelength. As demonstrated in Section 6.3, the channel reflectance correlation is therefore less sensitive to aerosol burden. The variability of the correlation for the range of aerosol optical depth of 0.05 to 0.20 is reasonably small. Furthermore, for an aerosol load this low the dynamic range of the channel reflectances is increased and the sensitivity of the correlation to the other atmospheric parameters such as wind speed and direction as well as solar geometry is decreased.

The correlation method was used to check the consistency of the preliminary calibration performed by NCAR based on the laboratory calibration of the MCR instrument after the INDOEX campaign. The preliminary calibrations try to account for the gain changes made during INDOEX. For this purpose, MCR scenes of flights in the southern hemisphere were evaluated. Out of the 18 research flights conducted by the NCAR C-130 during INDOEX, Flights 4, 8, 11 and 17 collected data in the southern hemisphere. Unfortunately, for many of the flights one or more of the channels failed. Among the southern hemisphere flights analyzed, all of the window channels, 1, 4, 5 and 6, functioned properly

TABLE 6.1: Comparison of observed and modeled channel correlations. The model results are given for $\tau_{ref} = 0.10$.

Flight No. and time	SZA	Lat.	Linear correlation with ch. 1			
			ch. 4	ch. 5	ch. 6	
RF08 08:52	21°	7.3 S	<i>obs.</i>	0.96 x - 0.007	1.46 x - 0.010	n/a
			<i>mod.</i>	1.09 x - 0.017	1.07 x - 0.020	n/a
RF11 08:47	22°	6.7 S	<i>obs.</i>	1.04 x - 0.011	1.86 x - 0.013	1.11 x - 0.018
			<i>mod.</i>	1.06 x - 0.012	1.04 x - 0.019	0.85 x - 0.013
RF17 06:49	11°	7.9 S	<i>obs.</i>	0.74 x - 0.006	2.11 x - 0.005	n/a
			<i>mod.</i>	1.07 x - 0.014	1.05 x - 0.017	n/a

only on Flight 11.

For the available flight data, the observational results were compared with the model values. The model calculations were performed considering the appropriate solar geometry, observational parameters such as flight altitude and relative azimuth angle to solar incidence, as well as the wind speed estimated from the observations. Tropical marine aerosol was considered at optical depths of 0.05, 0.10, and 0.20. This range is typical for the pristine air of the tropical Indian Ocean in the southern hemisphere and the variability of the slopes in this range of aerosol burden is only a few percent.

The results for $\tau_{ref} = 0.10$ are compiled in Table 6.1. For all three flights considered, there are large discrepancies that exhibit the need for recalibration of the MCR-channels. Not only do modeled and observed slopes lack agreement, the discrepancies are different between different flights. Whereas during Flight 11 the correction of the calibration for channel 4 would be only a few percent, the appropriate correction for Flight 17 is on the order of 30 %. Even between Flight 8 and 11, between which no gain adjustments were made, the calibration is inconsistent. For Flight 8, the slope for the correlation of the observed reflectances is significantly smaller than that obtained for Flight 11.

6.4 Consistency Tests for MODIS

In order to validate the methodology of the calibration check performed for the MCR, it is instructive to perform similar tests for the well calibrated and reliable satellite borne MODIS instrument. MODIS has 19 channels in the solar spectrum, out of which three correspond to the window channels with the low absorption of the MCR: Channel 1 is centered at $0.645 \mu\text{m}$ and corresponds to

the MCR channel 1, MODIS channel 6 is centered at $1.64 \mu\text{m}$ and corresponds to channel 5 of the MCR, and channel 7 of MODIS is centered at $2.13 \mu\text{m}$ and mostly overlaps with the MCR's channel 6 (King et al., 2003).

TABLE 6.2: Observed channel correlations for MODIS.

Scene (Year-Day-Time)	SZA	Lat.	Linear correlation with ch. 1	
			ch. 6	ch. 7
03-073-07:32	25°	10 S	1.119 x - 0.022	0.864 x - 0.017
03-071-06:03	23°	4 S	1.120 x - 0.022	0.885 x - 0.018
03-071-04:25	24°	6 S	1.115 x - 0.023	0.872 x - 0.019
03-067-06:26	24°	2 N	1.123 x - 0.023	0.918 x - 0.021
03-020-03:58	25°	21 S	1.097 x - 0.022	0.872 x - 0.016
01-081-06:13	23°	6 S	1.185 x - 0.025	0.925 x - 0.021
01-079-06:22	21°	8 N	1.328 x - 0.036	1.074 x - 0.031
01-067-05:57	24°	10 N	1.662 x - 0.061	1.356 x - 0.052

A set of MODIS sun glint scenes in the tropical Indian Ocean, where the aerosol characteristics are well studied, was analyzed. It included 5 scenes from the southern hemisphere, one equatorial scene at longitude 63°, more than 1500 km away from any continent, as well as two scenes from the Arabian sea in rather close proximity to the Asian continent. The results of the regressions of the correlations are given in Table 6.2. MODIS is mounted on the Aqua satellite which observes the earth on a polar-orbiting sun-synchronous track. This means that the equator is always passed at the same local time, and the viewing geometry is therefore very similar for the scenes considered. For reference optical depths of 0.05, 0.10 and 0.20 of tropical marine aerosol the modeled correlations for the 0.64 μm and the 1.64 μm channels are given in

FIGURE 6.10: Modeled correlations of $0.64 \mu\text{m}$ reflectance with $1.64 \mu\text{m}$ reflectance (a) and $2.13 \mu\text{m}$ reflectance (b) for MODIS. Calculations for $\tau_{ref} = 0.05, 0.10, 0.20$ are presented.

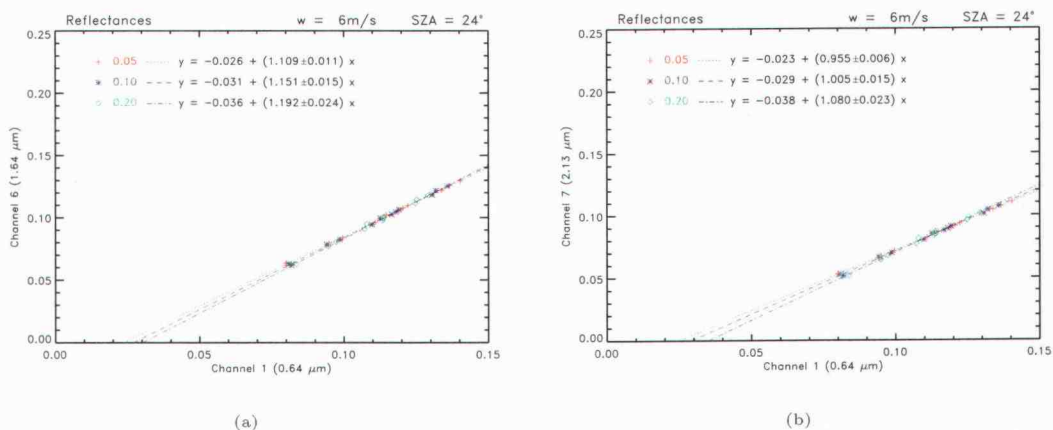


Figure 6.10.

The $0.64\mu\text{m}$ - $1.64\mu\text{m}$ correlations are very similar for the southern hemisphere and the equatorial scene. Apart from scene 01-081-06:13, the correlation slopes are within 2 % of 1.11. For scene 01-081-06:13, the slope is somewhat larger, possibly due to cloud contamination or a stronger aerosol contamination. The agreement between modeled and observed correlation is remarkably good. The observed correlation matches the modeled correlation for an aerosol optical depth of 0.10.

For the scenes from the Arabian sea, where the air is expected to be polluted with continental aerosol, the observed correlations are much more variable and have a much larger slope than those for the southern hemisphere. These findings are consistent with the modeled correlations and sensitivities for average

continental aerosol (Section 6.2.1).

The correlations of the 0.64- μm and the 2.16 μm channels show somewhat less agreement between observations and model results. The observed correlations are slightly more variable than those obtained for the 1.64- μm channel. For the cases of pristine marine air the slopes range from 0.864 to 0.925 and are consistently smaller than those obtained from the model. For the trace gas profiles adapted from the standard tropical atmosphere and aerosol optical depths ranging from 0.05 to 0.20, the modeled slopes range from 0.95 to 1.08.

Possible reasons for the discrepancy between model and observations include underestimation of water vapor abundance, inaccuracy of the aerosol model used, and polarization effects. As discussed in Section 6.2.5, the reflectances and correlations involving the 2.1 to 2.2 μm band are sensitive to water vapor abundance. It turns out that for a water vapor abundance twice that of the standard tropical atmosphere model, the modeled slopes range from 0.93 to 1.06 for the same range of aerosol burdens. This suggests that the uncertainty in atmospheric water vapor content could at least partly account for the discrepancy. Unfortunately, there is no information available on the polarization sensitivity of the MODIS device. As discussed in Section 4.7, the polarization sensitivity could easily account for biases in the observations of few percent. Since the polarization sensitivity could have different signs for different channels, this bias could significantly affect the correlations of the measured reflectances.

CHAPTER 7

CONCLUSIONS

In this thesis the Monte Carlo Radiative Transfer model (MOCARAT) was introduced. MOCARAT was implemented for accurate simulation of the reflectance field observed by imaging radiometers over the ocean. It is capable of modeling the radiance and reflectance field in a plane-parallel atmosphere with molecular (Rayleigh) scattering, scattering and absorption by aerosols, and non-grey molecular absorption. A key feature of MOCARAT is the implementation of the bidirectional reflectance distribution function of the air-ocean interface derived from the wave facet slope distribution introduced by Cox and Munk (1954b).

In order to assess the performance of MOCARAT, comparisons with other radiative transfer models were performed. The reference models are based on the discrete ordinate method for explicit solution of the equation of radiative transfer, and their results can therefore be considered independent from those obtained by MOCARAT. Separate runs were conducted for the verification of the atmospheric band radiative transfer and that of the oceanic reflection. For the test of the atmospheric radiative transfer, the RADK/DISORT model was utilized as a reference model. The agreement between MOCARAT and RADK/DISORT was found to be very good. The small departures between the two models at the limb can be attributed to the different algorithmic approaches and are well understood. The verification of the bidirectional reflection at the ocean surface was accomplished by comparison with the libRadtran and SB-

DART models. Test runs were performed both for isotropic slope distributions and slope distributions aligned with the wind field (MOCARAT and libRadtran only). The agreement between the three models is reasonably good, however, due to the somewhat different parameterizations used for the simulation of slope distribution and water-leaving radiance, minor deviations exist.

Since the modeling of absolute radiances in the sun glint depends critically on accurate knowledge of the surface wind field, a method was proposed to use correlations of the reflectances for different channels across the sun glint as a robust signal for remote sensing applications. The results of the sensitivity studies show that the correlations are rather insensitive to surface wind conditions and observational geometry. The sensitivity to aerosol burden was found to be rather large for small aerosol particles such as those typical of polluted continental air. For large aerosol particles such as those typically encountered in tropical marine air, the sensitivity to aerosol burden was found to be significantly smaller.

The correlation method was used to check the consistency of the current calibrations of the MCR instrument. The correlations of the observed radiances differed from those obtained from the model and exhibited large variability from flight to flight even in the pristine atmosphere of the southern hemisphere, where they were expected to be stable. The lack of agreement between the model and observations suggests that gain changes during the flights were not properly considered during the data processing. A careful recalibration of the data is necessary before it can be used for the proposed studies of aerosol-cloud interactions.

The correlation method was also tested by applying it to MODIS. The observed correlations from the southern hemisphere Indian Ocean were found to be stable for scenes on different days. Very good agreement was found between

the model and the observations for the correlation of the 1.64 μm and 0.64 μm reflectance correlations. By contrast, the model systematically overestimated the slopes of the 2.13 μm versus 0.64 μm correlations. It is necessary to investigate whether the discrepancy is due to measurement errors or systematic shortcomings in the modeling approach, such as the use of inaccurate aerosol and atmospheric trace gas models.

BIBLIOGRAPHY

- Abramowitz, M., and I.A. Stegun (eds.), 1965: *Handbook of Mathematical Functions*. Dover Publikations, New York.
- Anderson, T.L., R.J. Charlson, S.E. Schwartz, R. Knutti, O. Boucher, H. Rodhe, and J. Heintzenberg, 2003: Climate Forcing by Aerosols - a Hazy Picture. *Science*, **300**, 1103-1104.
- Bohren, C.F, and D.R. Huffmann, 1983: *Absorption and Scattering of Light by Small Particles*. John Wiley & Sons, New York.
- Cahalen, R.F, and R. Davies (eds.), 2000: *Intercomparison of Three-dimensional Radiation Codes(I3RC)*. abstracts of the First and Second International Workshops in Tucson, Arozona.
- Chandrasekhar, S., 1950: *Radiative Transfer*. Oxford University Press, London, UK.
- Coakley, J.A., W.R. Tahnk, A. Jayaraman, P.K. Quinn, C. Devaux, and D. Tanré, 2002: Aerosol optical depths and direct radiative frocing derived from AVHRR: Theory. *J. Geophys. Res.*, **107**.INX2, **8**, 1-18.
- Cox, C., and W. Munk, 1954a: Measurement of the Roughness of the Sea Surface from Photographs of the Sun's Glitter. *J. Opt. Soc. Am.*, **44**, 838-850.
- Cox, C., and W. Munk, 1954b: Statistics of the Sea Surface Derived from Sun Glitter. *J. Mar. Res.*, **13.2**, 198-227.

- Curran, R.J., H.L. Kyle, L.R. Blaine, J. Smith, and T.D. Clem, 1981: Multi-channel scanning radiometer for remote sensing cloud physical parameters. *Rev. Sci. Instrum.*, **52.10**, 1546-1555.
- Dorsey, N.E., 1940: *Properties of Ordinary Water-Substance*. Reinhold Pub. Co., New York.
- Evans, K.F., and Stephens, G.L., 1991: A New Polarized Atmospheric Radiative Transfer Model. *J. Quant. Spectrosc. Radiat. Transfer*, **46.5**, 413-423.
- Friedmann, D., 1969: Infrared Characteristics of Ocean Water(1.5-15 μ). *Appl. Opt.*, **8.10**, 2073-2078.
- Haywood, J., and Boucher, O., 2000: Estimates of the Direct and Indirect Radiative Forcing due to Tropospheric Aerosol: A Review. *Rev. Geophys.*, **38.4**, 513-543.
- Hess, M., P. Koepke, and I. Schult, 1998: Optical Properties and Clouds: The Software Package OPAC. *Bull. Am. Met. Soc.*, **79.5**, 831-844.
- Houghton, J.T., Y. Ding, D.J. Griggs, M. Noguer, P.J. van der Linden, X. Dai, K. Maskell, C.A. Johnson (eds.), 2001: *Climate Change 2001. The Scientific Basis*, Cambridge University Press, Cambridge, UK.
- Hulst, H.C. van de, 1957: *Light scattering by small particles*. John Wiley & Sons, New York.
- Jackson, J.D., 1962: *Classical Electrodynamics*. John Wiley & Sons, New York.
- Kaufmann, Y.J., J.V. Martins, L.A. Remer, M.R. Schoeberl, and M.A. Yamasoe, 2002: Satellite Retrieval of Aerosol Absorption over the Oceans Using Sun glint. *Geophys. Res. Lett.*, **41**, 442-458.

- Khuri, A.I., 2003: *Advanced Calculus with Applications in Statistics, 2nd Ed.* John Wiley & Sons, New York.
- Kleidman, R.G., Y.J. Kaufman, B.-C. Gao, L.A. Remer, V.G. Brackett, R.A. Ferrare, E.V. Browell, and S. Ismail, 2000: Remote Sensing of Total Precipitable Water Vapor in the Near-IR over Ocean Glint. *Geophys. Res. Lett.*, **27.17**, 2657-2660.
- Kneizys, F.X., D.C. Robertson, L.W. Abreu, P. Acharya, G.P. Anderson, L.S. Rothman, J.H. Chetwynd, J.E.A. Selby, E.P. Shettle, W.O. Gallery, A. Berk, S.A. Cough, 1996: *The MODTRAN 2/3 Report and Lowtran 7 Model*. Phillips Laboratory, Geophysics Directorate, Hanscom AFB, MA 01731-3010.
- King, M.D., Y.J. Kaufman, W.P. Menzel, and D. Tanré, 1992: Remote Sensing of Cloud, Aerosol, and Water Vapor Properties from the Moderate Resolution Imaging Spectrometer (MODIS). *IEEE Trans. Geosci. Remote Sens.*, **30**, 2-27.
- King, M.D., W.P. Menzel, Y.J. Kaufman, D. Tanré, B.-C. Gao, S. Platnick, S.A. Ackermann, L.A. Remer, R. Pincus, and P.A. Hubanks, 2003: Cloud and Aerosol Properties, Precipitable Water, and Profiles of Temperature and Water Vapor from MODIS. *IEEE Trans. Geosci. Remote Sens.*, **41**, 442-458.
- Kratz, D.P., 1995: The Correlated k -Distribution Technique as Applied to the AVHRR Channels. *J. Quant. Spectrosc. Radiat. Transfer*, **53.5**, 501-517.
- Kylling, A., and B. Mayer (2002): *libRadtran 1.0-beta - library for radiative transfer calculations*. www.libradtran.org.
- Lacis, A.A., and V. Oinas, 1991: A Description of the Correlated k Distribution Method for Modeling Nongray Gaseous Absorption, Thermal Emission, and

- Multiple Scattering in Inhomogeneous Atmospheres. *J. Geophys. Res.*, **38.4**, 513-543.
- Liou, K.N., 2002: *An Introduction to Atmospheric Radiation, 2nd Ed.* Academic Press, San Diego.
- Marchuk, G.I., G.A. Mikhailov, M.A. Nazaraiev, R.A. Darbinjan, B.A. Kargin, and B.S. Elepov, 1980: *The Monte Carlo Methods in Atmospheric Optics.* Springer: Berlin, Heidelberg, New York.
- Nicolet, M., R.R. Meier, D.E. Anderson, Jr., 1982: Radiation Field in the Tropopause and Stratosphere - II. Numerical Analysis. *Planet. Space Sci.*, **30.9**, 935-983.
- O'Brien, D.M. and R.M. Mitchell, 1988: Retrieval of Surface Wind Speed and Aerosol Optical Depth over the Oceans from AVHRR Images of Sun Glint. *J. Appl. Met.*, **27**, 1395-1403.
- Penndorf, R., 1957: Tables of the Refractive Index for Standard Air and the Rayleigh Scattering Coefficient for the Spectral Region between 0.2 and 20.0 μ and Their Application to Atmospheric Optics. *J. Opt. Soc. Am.*, **47**, 176-182.
- Press, W. H., S.A. Teukolsky, W.T. Vetterling, and B.P. Flannery, 1995: *Numerical Recipes in Fortran; The Art of Scientific Computing, 2nd Ed.* Cambridge University Press.
- Pruppacher, H.R., and J.D. Klett, 1978: *Microphysics of Clouds and Precipitation.* D. Reidel, Dordrecht, Boston, London.

- Ramanathan, V., P.J. Crutzen, J.A. Coakley, Jr., A. Clarke, W.D. Collins, R. Dickerson, D. Fahey, B. Gandrud, A.J. Haymsfield, J.T. Kiehl, J. Kuettner, T.N. Krishnamurti, D. Lubin, H. Maring, J.A. Ogren, J. Prospero, P. Rasch, D. Savoie, G.E. Shaw, A. Tuck, F.P.J. Valero, E.L. Woodbridge, and G. Zhang, 1996: Indian Ocean Experiment(INDOEX): A multi-agency proposal for a field experiment in the Indian Ocean. *C4 Publ.* **162**, Scripps Institution of Oceanography, Univ. of Calif. San Diego, La Jolla.
- Ramanathan, V., P.J. Crutzen, J.T. Kiehl, D. Rosenfeld, 2001: Aerosols, Climate, and the Hydrological Cycle. *Science*, **294**, 219-224.
- Ramanathan, V., P.J. Crutzen, J. Lelieveld, A.P. Mitra, D. Althausen, J. Anderson, M.O. Andreae, W. Cantrell, G.R. Cass, C.E. Chung, A.D. Clarke, J.A. Coakley, A.J. Haymsfield, W.D. Collins, W.C. Conant, F. Dulac, J. Heintzenberg, A.J. Haymsfield, T.N. Krishnamurti, R. Dickerson, D. Fahey, B. Gandrud, A. Haymsfield, J.T. Kiehl, J. Kuettner, T. Krishnamurti, D. Lubin, G. McFarquhar, T. Novakov, J.A. Ogren, I.A. Podgorny, K. Prather, K. Priestley, J.M. Prospero, P.K. Quinn, K. Rajeev, P. Rasch, S. Rupert, R. Sadourny, S.K. Satheesh, G.E. Shaw, P. Sheridan, and F.P.J. Valero, 2001: Indian Ocean Experiment: An integrated analysis of the climate forcing and effects of the great Indo-Asian haze. *J. Geophys. Res.*, **106.D22**, 28,371-28,398.
- Rogers, R.R., and M.K. Yau, 1989: *A Short Course in Cloud Physics, 3rd Ed.*. Butterworth-Heinemann, Woburn, MA.
- Satheesh, S.K., V. Ramanathan, X. Li-Jones, J.M. Lobert, I.A. Podgorny, J.M. Prospero, B.N. Holben, and N.G. Loeb, 1999: A Model for the Natural and

- Anthropogenic Aerosols over the Tropical Indian Ocean Derived from the Indian Ocean Experiment Data. *J. Geophys. Res.*, **104.D22**, 27,421-27,440.
- Sokolik, I.N., and O.B. Toon, 1996: Direct radiative forcing by anthropogenic airborne mineral aerosols. *Nature*, **381**, 681-683.
- Stamnes, K., and H. Dale, 1981: A New Look at the Discrete Ordinate Method for Radiative Transfer Calculations in Anisotropically Scattering Atmospheres. II: Intensity Computations. *J. Atmos. Sci.*, **38**, 2696-2706.
- Stamnes, K., and R.A. Swanson, 1981: A New Look at Discrete Ordinate Radiative Transfer Calculations in Anisotropically Scattering Atmospheres. *J. Atmos. Sci.*, **38**, 387-399.
- Stamnes, K., S-C. Tsay, W. Wiscombe, and K. Jayaweera, 1988: Numerically stable algorithm for discrete-ordinate-method radiative transfer in multiple scattering and emitting layered media. *Appl. Opt.*, **27**, 2502-2509.
- Stowe, L.L., A.M. Ignatov, and R.R. Singh, 1997: Development, Validation, and Potential enhancements to the second-generation operational aerosol product at the National Environmental Satellite, Data, and Information Service of National Oceanic and Atmospheric Administration. *J. Geophys. Res.*, **102.D14**, 16923-16934.
- Tahnk, W.R., 2001: INDOEX Aerosol Optical Depth and Radiative Forcing Derived from AVHRR. PhD Dissertation, Oregon State University.
- Takashima, T., 1985: Polarization Effect on Radiative Transfer in Planetary Composite Atmospheres with Interacting Interface. *Earth, Moon, and Planets*, **33**, 59-97.

- Thomas, G.E., and K. Stamnes, 2002: *Radiative Transfer in Atmosphere and Ocean*. Cambridge University Press.
- Twomey, S.A., 1977: The influence of pollution on the shortwave albedo of clouds. *J. Atmos. Sci.*, **34**, 1149-1152.
- Walker, R.E., 1994: *Marine Light Field Statistics*. John Wiley & Sons, New York.
- Wallace, J.M., and Hobbs, P.V., 1977: *Atmospheric Science: An Introductory Survey*. Academic Press, San Diego.
- Wisombe, W, and J. Evans, Exponential-sum fitting of radiative transmission functions. *J. Comput. Phys.*, **38.4**, 513-543.